CRYSTALLOGRAPHIC ANALYSIS OF THE REGULATORY DOMAIN OF HUMAN CARDIAC TROPONIN C

by

Yueh Alison Li
B. Sc., University of British Columbia, 2005

THESIS SUBMITTED IN PARTIAL FULFILLMENT OF
THE REQUIREMENTS FOR THE DEGREE OF

MASTER OF SCIENCE

In the
Department of Molecular Biology and Biochemistry

SIMON FRASER UNIVERSITY

Summer 2009

APPROVAL

Name: **Yueh Alison Li**

Degree: **Master of Science**

Title of Thesis: **Crystallographic Analysis of the Regulatory Domain of Human Cardiac Troponin C**

Examining Committee:

Chair: **Dr. Frederic Pio**, Assistant Professor, Department of Molecular Biology and Biochemistry

_____

Dr. Mark Paetzel
Senior Supervisor
Associate Professor, Department of Molecular Biology and Biochemistry

_____

Dr. Glen Tibbits
Supervisor
Professor, Department of Biomedical Physiology and Kinesiology

_____

Dr. Jack Chen
Supervisor
Associate Professor, Department of Molecular Biology and Biochemistry

_____

Dr. Edgar C. Young
Internal Examiner
Assistant Professor, Department of Molecular Biology and Biochemistry

Date Defended/Approved: July 22, 2009

Declaration of Partial Copyright Licence

ABSTRACT

The N-terminal regulatory domain of cardiac troponin C (N-cTnC) is an essential Ca^{2+} sensor to trigger muscle contraction. Using X-ray crystallography, the first crystal structure of wild type human N-cTnC was solved to 2.2 Å resolution. It revealed two novel features about this protein. First, each EF-hand binding loop coordinates two cadmium ions, even though one of the loops is normally inactive. One Cd^{2+} ion occupies the canonical ion binding site, whereas the other Cd^{2+} ion binds adjacent to it. Thus, N-cTnC is forced to adopt a very unusual conformation. Second, an additive, deoxycholic acid (DXC), was observed bound to the central hydrophobic cavity and between helix N and helix A. DXC has a similar chemical structure to Ca^{2+}-sensitizing drugs that are used for treating troponin-related cardiovascular diseases. These new insights provide valuable information for the use of N-cTnC as a potential target for rational drug design.

Keywords: troponin C, X-ray crystallography, EF-hand binding loop, cadmium ion coordination, deoxycholic acid, protein structure

ACKNOWLEDGEMENTS

First of all, I would like to thank my senior supervisor, Dr. Mark Paetzel, for giving me the opportunity to carry out this interesting project that really opened my eyes to the beauty and the challenges of X-ray protein crystallography. I would like to thank my committee member and collaborator, Dr. Glen Tibbits, for providing the cell constructs and giving suggestions and guidance for my project. I would also like to thank my other committee member, Dr. Jack Chen, for his encouragement and support throughout my studies.

I would like to express my sincere thanks to our lab manager, Deidre de John-Wong, for making the Paetzel lab a neat and organized workplace, and for her continuous support and invaluable assistance during the most difficult times of my studies. I would like to thank Dr. Jaeyong Lee, for being such a wonderful and patient mentor, who taught me everything from the simplest protein purification techniques to the most difficult data processing, and helped me understand the theory and the background of crystallography. I cannot thank enough to Dr. Borek Dominika and Dr. Zbyszek Otwinowski from the UT Southwestern Medical Center, for their unquestionable generous help on solving these very difficult datasets and providing useful suggestions for my protein structure. I would also like to thank the past and the present members of the Paetzel lab, the former post-Doc Dr. David Oliver, and graduate students, Yun, Yuliya, Apollos, Ivy, Kelly, Charlie, Sung, and Daniel, for their encouragement

and friendship that made this lab a fun and enjoyable environment. I especially would like to thank Charlie for trouble shooting all the computer problems that I encountered and patiently answering all my questions regarding any computer issues. I am also truly grateful for Dr. Jaeyong Lee and Charlie for taking their time to proofread my entire thesis. I would also like to thank Edward from Dr. Agnes lab for analyzing my protein samples by mass spectrometry.

Finally, I would like to my parents, Jimmy and Penny, my brother, Jeff, and my better half Johnny Lee, for their unwavering support and for always believing in me. They have always been the most important support I have and I could not have done this project without their encouragement and love. Thank you.

TABLE OF CONTENTS

Approval ..... **ii**

Abstract ..... **iii**

Acknowledgements ..... **iv**

Table of Contents ..... **vi**

List of Figures ..... **ix**

List of Tables ..... **xiv**

Glossary ..... **xv**

1: Introduction **1**

1.1 Discovery of troponin 1
1.2 Cardiac muscle regulation by the troponin complex 2
1.3 General background of TnC 5
1.4 Ca^{2+} binding to EF hand and HMJ model 8
1.5 Mutation in troponin C and its relation to familial hypertrophic cardiomyopathy 20
1.6 Three dimensional structure of cardiac TnC 25
1.6.1 TnC in complex with TnI and binding drug 27
1.6.2 Bepridil 28
1.6.3 Trifluoperazine (TFP) 33
1.6.4 Levosimendan 34
1.6.5 EMD 57033 36
1.6.6 Anapoe 39
1.6.7 Troponin complex 41
1.7 Overview of Objectives 47

2: crystallization of the amino-terminal domain of cardiac troponin C in the trigonal/hexagonal system – dealing with twinned crystals **50**

2.1 Introduction 50
2.2 Materials and Methods 56
2.2.1 Mutagenesis of full-length troponin constructs 56
2.2.2 Overexpression of the native N-cTnC protein 57
2.2.3 Native N-cTnC purification by column chromatography 57
2.2.4 Crystallization of native N-cTnC protein 59
2.2.5 Data collection for WT N-cTnC 59
2.2.6 Data collection for L29Q N-cTnC 59
2.2.7 Data collection for NIQD N-cTnC 60
2.2.8 Data processing 60

2.3 Results and Discussion 61
2.3.1 Mutagenesis of full-length troponin constructs 61
2.3.2 Over-expression and purification of native N-TnC proteins 62
2.3.3 Crystallization of native troponin C 65
2.3.4 Data processing on the trigonal/hexagonal crystal 67
2.3.5 Twinning analysis 69
2.4 Conclusion 74

3: CRYSTALLIZATION of the N-terminal domain of cardiac troponin C in the orthorhombic system – dealing with radiation damage 75

3.1 Introduction 75
3.2 Materials and methods 78
3.2.1 Crystallization of the native orthorhombic crystal of WT N-cTnC 78
3.2.2 Data collection for the native orthorhombic WT N-cTnC crystal 80
3.2.3 Data processing for the native orthorhombic WT N-cTnC crystal 81
3.2.4 Over-expression of Se-Met-incorporated N-cTnC proteins and purification 81
3.2.5 Confirmation of Se-Met incorporation by Matrix-assisted laser desorption/ionisation-time of flight mass spectrometry (MALDI-TOF MS) 82
3.2.6 Crystallization of Se-Met-incorporated WT N-cTnC 83
3.2.7 Data collection for Se-Met-incorporated WT N-cTnC 83
3.2.8 Phasing, structure determination, and refinement 84
3.3 Results and discussion 85
3.3.1 Crystallization of the native orthorhombic crystal of WT N-cTnC 85
3.3.2 Data processing for the native orthorhombic crystal of WT N-cTnC 86
3.3.2 Purification and crystallization of Se-Met-incorporated WT N-cTnC 87
3.3.3 Confirmation of Se-Met incorporation 90
3.3.4 Data analysis for Se-Met-incorporated WT N-cTnC 92
3.3.5 Phasing 94
3.3.6 Structure determination and refinement 96

4: STRUCTURAL analysis of human N-ctnc 99

4.1 Protein fold of N-cTnC 99
4.2 The dimerization interface 104
4.3 The cadmium binding sites 109
4.4 The deoxycholic acid binding pocket on N-cTnC 126
4.5 Comparison with other N-cTnC Structures 138
4.6 Conclusion 154

Appendices 156
5: BIBLIOGRAPHY 163

LIST OF FIGURES

Figure 1-1: The schematic of (a) thin and thick filament and (b) how troponin complex regulates muscle contraction. 4

Figure 1-2: Sequence alignment of full-length human cTnC (161 residues) with full-length human sTnC (160 residues). 6

Figure 1-3: Full-length NMR structure of (a) sTnC and (b) cTnC. 7

Figure 1-4: (a) A schematic representation of the primary and secondary structure of human cTnC with Ca^{2+} binding in each functional binding site and (b) the alignment of the four EF-hand binding motif. 11

Figure 1-5: The four EF-hand Ca^{2+} binding site in full-length human cTnC (PDB: 1J1D). 12

Figure 1-6: The superposition of chicken skeletal N-domain of TnC from residue 1-90 (black) and C-domain from residue 91-161 (white) (PDB: 1YTZ). 14

Figure 1-7: A Cα-trace of sTnC that shows the difference between Ca^{2+}-free and Ca^{2+}-bound structure of sTnC. 16

Figure 1-8: Superposition of the NMR structure of Ca^{2+}-free human N-cTnC (orange, PDB: 1SPY) with the NMR structure of Ca^{2+}-bound human N-cTnC (green, PDB: 1AP4). 17

Figure 1-9: Cartoon representations of skeletal and cardiac TnC in Ca^{2+}-free and Ca^{2+}-bound form. 20

Figure 1-10: The cartoon representation of N-cTnC with (a) L29 highlighted and with (b) D2, V28, L29, and G30 highlighted (PDB: 1J1D). 25

Figure 1-11: The chemical structures of Ca^{2+} sensitizing drugs and their binding site on TnC. 28

Figure 1-12: The structure of full-length chicken cTnC complex with three bepridil molecules. 30

Figure 1-13: (a) cartoon representation of the NMR structure of the ternary complex of N-cTnC·Ca^{2+}·$cTnI_{147-163}$ ·bepridil (PDB: 1LXF) and (b) the electrostatic representation of the same model. 31

Figure 1-14: A stepwise mechanism of the effects of Ca^{2+}, bepridil, and the $cTnI_{147-163}$ peptide on the conformation of N-cTnC. 33

Figure 1-15: (a) The crystal structure of N-cTnC-Ca^{2+} bound with 2 TFP molecules. (PDB: 1WRK; Takeda *et. al.* 2003) and (b) the electrostatic representation of 1WRK with 2TFP molecules bound. 34

Figure 1-16: Levosimendan and analogs. Figures were generated using GChemPaint (Brefort 2001) and adapted from Li, 2008, Bicohm. Biophys. Res. Commun. (Li 2008) 36

Figure 1-17: (a) The cartoon representation of the NMR strucutre of $2Ca^{2+}$·C-cTnC·EMD57033. (PDB: 1HIO) (b) the surface representation and..... 39

Figure 1-18: Crystal structure of the sTnC complex with Anapoe. (PDB: 1YTZ) 41

Figure 1-19: Crystal structure of the 52kDa domain of human cardiac troponin in the Ca^{2+} saturated form. 43

Figure 1-20: Structure comparison of the two molecules in the asymmetric unit of Tn46K (Tn46KA, green; Tn46KB blue) and the two molecules in the asymmetric unit of Tn52K (Tn52KA, red; Tn52KB, orange). 45

Figure 1-21: A schematic representation of the conformation of cardiac troponin in relation to thin filament in the absence and presence of Ca^{2+}. 47

Figure 2-1: They hypothetical models of (a) epitaxial twinning and (b) merohedral twinning. Figure is adpated from Yeats, 1999 (Yeates 1999). 52

Figure 2-2: The H twinning test carried out by DETWIN. 54

Figure 2-3: The example of Britton plot for (a) untwinned data and (b) twinned data. 55

Figure 2-4:Sequence alignment between N-TnC and full length WT bovine TnC (Swiss-Prot accession number P63315) to confirm the site-directed mutagenesis. 62

Figure 2-5: A small scale protein expression for N-TnC/pET21/BL21(DE3). 63

Figure 2-6: Purification of WT N-cTnC proteins by hydrophobic interaction chromatography..... 64

Figure 2-7: Gel filtration chromatogram of WT N-cTnC. 65

Figure 2-8: The trigonal/hexagonal crystal of (a) WT N-TnC; crystal dimension is approximately of 0.20 mm × 0.15 mm × 0.02 mm. (b) The trigonal/hexagonal crystal of L29Q N-cTnC; crystal dimension is approximately of 0.11 mm × 0.11 mm × 0.02 mm.

(c) The trigonal/hexagonal crystal of NIQD N-cTnC; crystal dimension is approximately 0.10 mm × 0.10 mm × 0.02 mm. 66

Figure 2-9: The H-test for twinning performed by DETWIN for (a) WT N-cTnC, (b) L29Q N-cTnC, and (c) NIQD N-cTnC. 72

Figure 2-10: The Britton plot obtained from DETWIN shows the twinning fraction of (a) WT N-cTnC, (b) L29Q N-cTnC, and (c) NIQD N-cTnC. 73

Figure 3-1: Statistics from scaling the individual images with the average of the data. 77

Figure 3-2: The orthorhombic crystal of native WT N-cTnC. The crystal dimension is approximately 0.30 mm × 0.25 mm × 0.05 mm. 86

Figure 3-3: Purification of Se-Met-incorporated WT N-cTnC by phenyl-sepharose hydrophobic interaction chromatography. 88

Figure 3-4: Chromatogram obtained from gel-filtration for Se-Met-incorporated WT N-cTnC. 89

Figure 3-5: The light scattering analysis of WT N-cTnC. 90

Figure 3-6: The orthorhombic crystal of Se-Met-incorporated WT N-cTnC. The dimension of the crystal is approximately 0.25 mm × 0.20 mm × 0.05 mm. 90

Figure 3-7: The mass spectra of the Se-Met-incorporated sample (top) and the native sample of the WT N-cTnC protein (bottom). 92

Figure 3-8: The statistical output of scaling suggests the presence of radiation damage based on the plots of (a) *B*-factor versus image number and (b) the X^2 and R-factor versus frame number. 93

Figure 3-9: Ramachandran plot of the crystallographic model of WT human N-cTnC. 98

Figure 4-1: The overall conformation of the four proteins chains in the asymmetric unit. 100

Figure 4-2: The orientation of the four protein molecules (chains) in the asymmetric unit. 101

Figure 4-3: The protein fold of human N-cTnC. 103

Figure 4-4: The superposition of the four chains coloured spectrally by B-factor, in which red denotes the most disordered regions and the most ordered regions are coloured blue. 104

Figure 4-5: The electrostatic surface properties of the AB dimer 106

Figure 4-6: The hydrogen bonding interactions at the interface formed between chain B and chain C. 108

Figure 4-7: The electron density of Cd^{2+} and Ca^{2+} on a (2Fo-Fc) map at (a) σ4.0 and (b) σ5.0. 111

Figure 4-8: Sequence alignment of our N-cTnC structure with other N-TnC homologous structure. 113
Figure 4-9: Cd^{2+} coordination in (a) EFI of chain A, (b-i) EFI of chain B, (b-ii) EFI of chain C, and (c) EFII of chain A. 119
Figure 4-10: The ion coordination of (a) Cd_{17} and (b) Cd_{18} outside the EF-hand binding loop. 125
Figure 4-11: The chemical structure of deoxycholic acid. 127
Figure 4-12: The DXC binding in the Phe-rich environment of N-cTnC protein chain. 128
Figure 4-13: The binding site of deoxycholic acid (DXC) in four N-cTnC protein chains from (a) the top view and (b) the side view. 130
Figure 4-14: The DXC binding site on the surface of (a) (b) AB dimer and (c) (d) CD dimer. 131
Figure 4-15: The binding location of (a) DXC_{A2} and DXC_{B2}, and (b) DXC_{C2} and DXC_{D2}. 134
Figure 4-16: The surface representation of dimer AB (white) and symmetry-related dimer CD (red). 136
Figure 4-17: Structural comparison of DXC to other Ca2+-sensitizer drugs: levosimendan, TFP, and EMD57033. 138
Figure 4-18: The superimposition of our crystal structure of human N-cTnC on the NMR structures of (a) Ca^{2+} free N-cTnC (PDB: 1SPY) and (b) Ca^{2+}-bound N-cTnC (PDB: 1AP4). 141
Figure 4-19: The chemical structure of TFP. 142
Figure 4-20: Comparison of the (a) crystal structure of 1WRK monomer (light cyan) and our human N-cTnC structure (blue) and (b) their superimposed structure. 145
Figure 4-21: The vacuum electrostatic representation of the binding pocket for (a) 1WRK and (b) our N-cTnC structure. 145
Figure 4-22: Comparison between (a) 1WRL (yellow) and our human N-cTnC structure (blue) and (b) their superimposed structure. 147
Figure 4-23: Comparison between (a) our human N-cTnC (blue) and homolog N-cTnC (cyan) with TnI peptide (orange) from full troponin complex model (1J1D). (b) Their superimposed structure. 149
Figure 4-24: Comparison between (a) the NMR structure of N-cTnC (white) in complexed with TnI peptide (orange) and bepridil (blue) (PDB: 1LXF) and our human N-cTnC structure (blue). (b) Their superimposed structure. 151

Figure 4-25: The superposition of the six homologous structures used for comparison, with (a) terminal helix N and helix A superimposed and (b) helix C superimposed. 152

Figure 4-26: Superposition of our human N-cTnC structure (blue) with the other N-cTnC structures. 154

LIST OF TABLES

Table 1-1: The previously-solved cTnC related structures. If Ca^{2+} is included in the final structure, then an X is marked in the "Ca^{2+}-BOUND" category; if Ca^{2+} is not included in the final structure, the an X is marked in the "Ca^{2+}-FREE" category. 26

Table 2-1: The possible merohedral twin operators for tetragonal, trigonal, hexagonal, and cubic space group system (Chandra 1999). 55

Table 2-2: Data collection statistics for hexagonal WT N-cTnC, L29Q N-cTnC, and NIQD N-cTnC. 67

Table 3-1: List of additives screened during crystallization experiments. 79

Table 3-2: Data collection statistics for native orthorhombic WT N-cTnC. 86

Table 3-3: The data collection statistics for AL281_C4a peak data and ALI_A peak data. 95

Table 3-4: Refinement statistics for Se-Met-incorporated orthorhombic WT N-cTnC 97

Table 4-1: The inter-chain hydrogen bonds between the two dimers of N-cTnC. 107

Table 4-2: Comparison between calcium and cadmium. 109

Table 4-3: Cadmium-ligand distance in the binding loop of N-cTnC. 120

Table 4-4: Additional Cd^{2+}-coordination with side chains not involved in the binding loop. 125

Table 4-5: Comparison of our human N-cTnC to 1WRK and 1WRL. 142

Table 4-6: Comparison of the phi-psi angle of residue 28-34 of chain A to that of 1WRK. 154

GLOSSARY

Å	Angstroms, a unit of measurement. 1Å = 10^{-10} meters
ADP	Adenosine diphosphate
Asymmetric unit	The largest assembly of molecules that has no symmetry in itself, but can be superimposed on other identical elements in the unit cell by symmetry operations
ATP	Adenosine triphosphate
B-factor	Also called a temperature factor. It is affected by atomic thermal motion and disorder of an atom. In the scaling process, it is a continuous function of accumulated X-ray dose absorbed by the protein sample, thus it can be used as an indicator for detecting radiation damage. In the refinement process, it points out the errors built in model and is determined by local crystal packing. It is related to the atomic displacement u by the equation: $B = 8\pi^2 \langle u^2 \rangle$. High B-factors indicate a high degree of disorder and a low degree of confidence about that particular part of the model.
Ca^{2+}	Calcium ion
Cd^{2+}	Cadmium ion
Chi square (χ^2)	A parameter used to indicate the quality of data collection. It is the squared ratio of differences between equivalent measurements divided by expected errors $(I_{hkl} - \langle I_{hkl} \rangle)^2/(\sigma^2_{I\ hkl} + \sigma^2_{\langle I\ hkl \rangle}$. Expected value is around 1 for reasonable model of error.
Completeness	The number of crystallographic reflections measured in a data set, expressed as a percentage of the total number of reflections present at the specified resolution.
Contractility	The ability of a cardiac muscle fibre to contract when its

	thick and thin filaments slide past each other.
Crystal	An array of atoms, molecules, or ions, which are packed in a regularly ordered, repeating pattern extending in all three spatial dimensions.
Crystal lattice	The regular spacing (defined by lengths and angles) grid of molecules from the origins of the individual unit cells).
Crystallographic Refinement	A cyclic process of improving agreement between the molecular model and the crystallographic data. In each cycle, a computing program coverts small optimizing shifts such as the adjustment of the atomic position, conformation of regions, and atom oscillations or vibrations around the atomic position, in order to obtain highly precise structural model that matches the data.
Da	Dalton, a unit used to express molecular masses. 1 Da ≈ 1 gram per mole
Crystallographic Data	The positions and intensities of reflections from a single crystal in the diffraction pattern produced by incident X-rays.
DXC	Deoxycholic acid
EFI	EF-hand binding loop I
EFII	EF-hand binding loop II
Electron Density Map	The map of electron clouds surrounding the molecule.
Hanging drop vapour diffusion	A common method of protein crystallization, in which small volumes of precipitant and protein are mixed together and the drop is equilibrated against a larger reservoir of solution containing precipitant or another dehydrating agent. Drops are placed on a coverslip that seals the reservoir, such that they hang over the reservoir solution. Both the sample and reagent increase in concentration as water leaves the drop for the reservoir until equilibration concentration is reached. This process may produce

	favourable conditions for crystallization.
HEPES	4-(2-hydroxyethyl)-1-piperazineethanesulfonic acid
IPTG	Isopropyl-β-D-thiogalactopyranoside
Matthews Coefficient	Specifies the specific volume (Vm) of the crystal and is calculated as Vm = V/(n ×m) where Vm is the volume of the unit cell, n is the number of asymmetric units, and M is the molecular weight of contents of the asymmetric unit. It has a unit of $Å^3$/Da. The average is 2.4 $Å^3$/Da , in a range of 1.9-4.2 $Å^3$/Da.
Mother liquor	The part of a solution that is left over after the crystals are removed.
Mosaicity	is the width of mis-orientation angles of all unit cells in a crystal, which is caused by the imperfect order of a crystal. This number has units of degrees. Lower mosaicity indicates better-ordered crystals and hence better diffraction.
Myocyte	The type of cell found in muscles. It contains myofibrils that are composed of long chains of sarcomere, which are the contractile units of the cell.
N-cTnC	N-terminal regulatory domain of troponin C (residue 1-89)
NMR	Nuclear magnetic resonance. A technique used to solve the molecular structure by measuring the absorption of electromagnetic energy of the nuclei of atoms when placed in a strong magnetic field.
Occupancy	A measure of the fraction of molecules in the crystal in which a particular atom actually occupies the position specified in the model. If all molecules in the crystal are precisely identical, then occupancies for all atoms are 1.00.
PDB	Protein Data Bank, http://www.rcsb.org
Ramachandran plot	A plot showing the main-chain conformational angles in a polypeptide. The conformational angles plotted are phi, the

torsional angle of the N-CA bond; and psi, the torsional angle of the CA-C bond. Due to steric repulsion, only certain conformational angles are allowed. The plot is used as a tool to assess the validity of the model.

Redundancy The data sets contain several independent measurements of each reflection due to symmetry in the crystal. Redundancy gives the average number of independent measurements of each reflection in a crystallographic data set and is calculated as the number of measured reflections divided by the number of unique reflections.

Refinement The process of improving the agreement between the molecular model and the crystallographic data by adjustment of positions, occupancies, and B-factors of atoms in the model. Progress in refinement is signified by decreasing R values, disappearance of residues from the unfavourable region of the Ramachandran plot, and improving chemical plausibility of the structure (e.g. bond lengths and angles).

R_{factor} A measure of agreement between the crystallographic model and the original X-ray diffraction data, calculated as $R = \sum \| F_{obs} | - | F_{calc} \| / \sum | F_{obs} |$, where F_{obs} and F_{calc} are structure factors observed from the measured data or calculated from the model, respectively.

R_{free} Calculated using the same equation as the R-factor, except only for a small subset (5-10%) of randomly chosen intensities, which are set aside at the beginning and not used in refinement. R_{free} measures how well the current model predicts a subset of the measured reflection intensities that were not included in the refinement. R_{free} is higher than the R_{factor} at the beginning of refinement, but in the final stages, the two values should become more similar.

R_{merge} A measure of the quality of the diffraction data. R_{merge} is calculated as follows: $R_{merge} = \sum | I - \langle I \rangle | / \sum \langle I \rangle$ (I is the individual measurement of each reflection, and <I> is the average intensity from multiple observations).

r.m.s.d. Root mean square deviation

SDS-PAGE	Sodium dodecyl sulfate polyacrylamide gel electrophoresis
Sitting drop vapour diffusion	Same principles as described for hanging drop vapour diffusion, except drops are placed on a pedestal above the reservoir solution
Space group	Designation of the symmetry of the unit cell of a crystal.
N-sTnC	N-terminal regulatory domain of skeletal troponin C
TFP	Trifluoperazine. An antipsychotic drug of the phenothiazine group that increases the Ca^{2+} affinity of TnC
TRIS	2-amino-2-hydroxymethyl-1,3-propanediol, a common biology buffer
TnC	Troponin C; the Ca^{2+} binding subunit of the troponin complex that acts as a Ca^{2+} sensor to initiate the cascade event of muscle contraction.
TnI	Troponin I; the inhibitory subunit of the troponin complex that switches its binding between TnC and actin monomers during muscle contraction and relaxation
TnT	Troponin T; the tropomyosin binding subunit of the troponin complex that anchors the troponin complex on tropomyosin
Unit cell	The simplest repeating unit in the crystal that is representative of the entire crystal

.

1: INTRODUCTION

1.1 Discovery of troponin

Since the early 1950's, the study of Ca^{2+}-dependent muscle contraction and relaxation has been an active research area for many biochemists and biophysicists. One of the many muscle researchers intrigued by this unknown mechanism, Dr. Ebashi Setsuro made a major breakthrough in understanding muscle contraction and relaxation in 1962. He discovered that the Ca^{2+}-dependent muscle contraction and relaxation was only observed when tropomyosin and an unknown protein factor were present. This unknown protein, which had the ability to confer the Ca^{2+} sensitivity to the purified myosin-actin system, was first named as "native tropomyosin" and eventually became known as "troponin" (Ebashi 1966). Ebashi's discovery of troponin was a significant step forward in muscle research and eventually led to more remarkable findings about this protein. For example, Otsuki *et. al*. demonstrated that the regular distribution of troponin molecules on each thin filament has an interval distance of 400 Å, by using fluorescent antibodies against troponin in an immune-electron microscopic study (Otsuki 1967). The periodic occurrence distance of troponin on actin filaments was supported by the binding stoichiometry of actin, tropomyosin, and troponin, which is 7:1:1, respectively (Ebashi 1969). Although troponin was originally thought to be a single protein, it was later found that three components were involved in forming the troponin complex. In 1972, during the Cold Spring

Harbor Symposium, “The Mechanism of Muscle Contraction”, the nomenclature and the identification of the three components of troponin were finalized as troponin C, troponin I, and troponin T (Watson 1972) . Since then, a more coherent mechanism of muscle contraction and relaxation and its Ca^{2+}-dependent regulation by troponin were accepted, and together they have served as an important foundation for muscle research in the past fifty years.

1.2 Cardiac muscle regulation by the troponin complex

Cardiac muscle contraction and relaxation is caused by the interaction of thick and thin filament in a Ca^{2+}-dependent manner. The thick filament consists of a polymer of motor protein myosin, and the thin filament consists of three main components: tropomyosin (Tm), actin, and troponin (Tn) (figure 1-1).

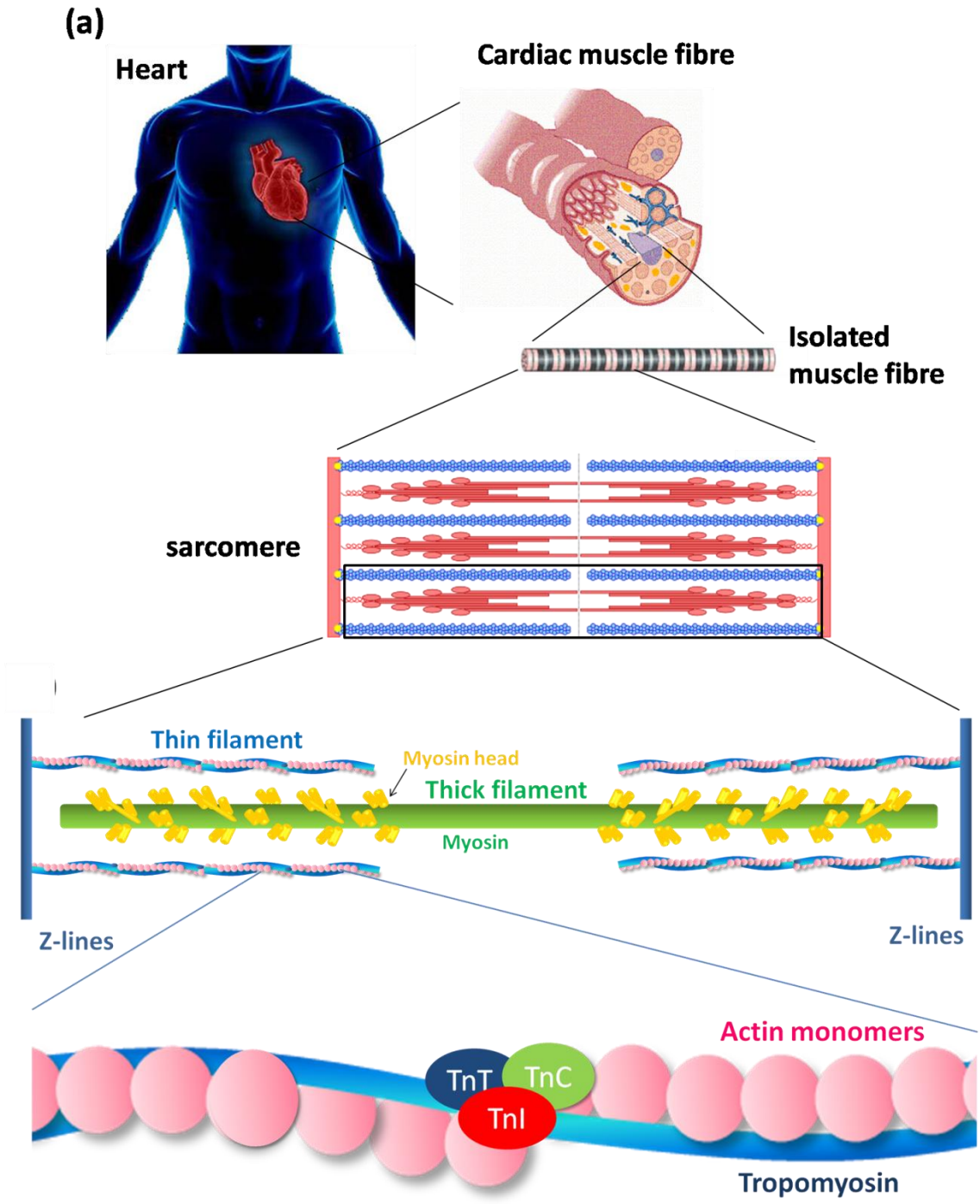
(a)
Heart
Cardiac muscle fibre
Isolated muscle fibre
sarcomere
Thin filament
Myosin head
Thick filament
Myosin
Z-lines
Z-lines
Actin monomers
TnT
TnC
TnI
Tropomyosin

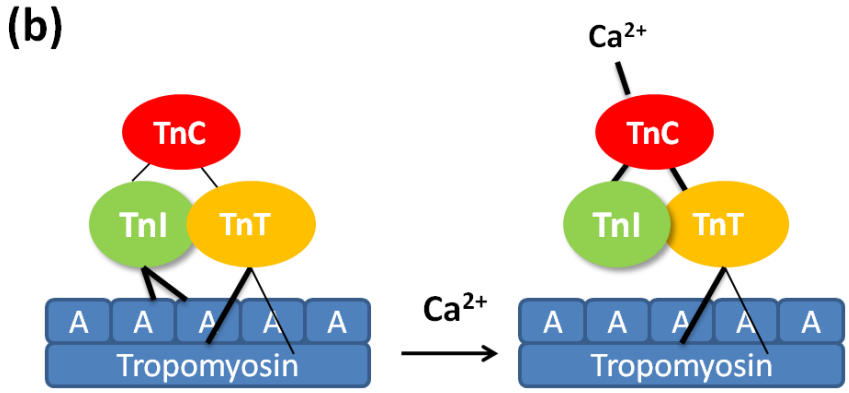

Figure 1-1: The schematic of (a) the location of troponin complex b) how troponin complex regulates muscle contraction.

(a) The thick filament is composed of myosin (green) with the head groups of myosin (yellow) attached to it. The thin filament is composed of tropomyosin (blue) and actin monomers (pink). An enlarged section of the thin filament is shown. The troponin complex is composed of TnT (blue, Swiss-Prot accession number: 45379), TnI (red) (Swiss-Prot accession number: P19429), and TnC (green) (Swiss-Prot accession number: 63316). The troponin complex is located on every seventh actin monomer throughout the thin filament. (b) How troponin complex regulates muscle contraction. In absence of Ca^{2+} binding to TnC, TnI has its inhibitory subunit remain bound on the actin monomers. In presence of Ca^{2+} binding to the regulatory domain of TnC, the conformation of TnC is changed from a closed state to a more open state, allowing TnI to switch its binding from actin monomers to TnC. This exposes the actin monomers that are previously bound by TnI, allowing the myosin head from the thick filament to bind. As the myosin head binds to one actin monomer after another, the thin filament slides past through the thick filament, hence the muscle contacts. (b) is adapted from Gordon *et. al.* (Gordon 2001).

The tropomyosin molecules form an elongated coiled-coil structure that intertwines with the double helix of actin monomers. Cardiac troponin, located on every seventh actin monomer throughout the thin filament, is an essential three-subunit complex that plays a key role in muscle regulation. The three subunits include: 1) Ca^{2+} binding subunit troponin C (TnC) that acts as a Ca^{2+} sensor, 2)

the inhibitory subunit troponin I (TnI) that inhibits the ATPase activity of actomyosin, and 3) the tropomyosin-binding subunit (TnT) that anchors troponin to tropomyosin. Together, the thin filaments interact with the thick filaments to allow a power stroke to occur, which is required for muscle contraction (Gordon 2000).

During systole, the spontaneously depolarizing cells of the sinoatrial node are activated by depolarization of their membranes. When this occurs, the voltage-gated Ca^{2+} channels on the cell membrane open and allow Ca^{2+} ions to move into the sarcoplasm of the muscle cells. Ca^{2+} ions then bind to its receptors on the sarcoplasmic reticulum and cause an influx of Ca^{2+} into the sarcoplasm. This process may increase the cystolic Ca^{2+} concentration from the nanomolar to the micromolar amount. These free cystolic Ca^{2+} ions then bind to the regulatory domain of TnC and causes TnC to undergo a conformational change that exposes its hydrophobic binding site for TnI. In the following event, TnI releases its inhibitory binding to actin-tropomyosin complex, and switches its binding to the regulatory domain of TnC. This results in an overall conformational change of troponin and tropomyosin binds to a different actin monomer, exposing the actin that was previously bound to the tropomyosin. This newly exposed actin is now available for the myosin head to bind. As the myosin head binds to one actin monomer after another, it causes the thick and think filaments to slide past each other so that the muscle contracts ((Farah 1995; Gordon 2000).

1.3 **General background of TnC**

Troponin C (TnC) is a highly conserved protein found in all striated muscle among vertebrate species. There are two isoforms of TnC: the fast skeletal TnC (sTnC) and the cardiac/slow skeletal TnC (cTnC). Skeletal TnC has 162 amino acid residues while cTnC has 161, and the sequence identity between them is 65% (figure 1-2).

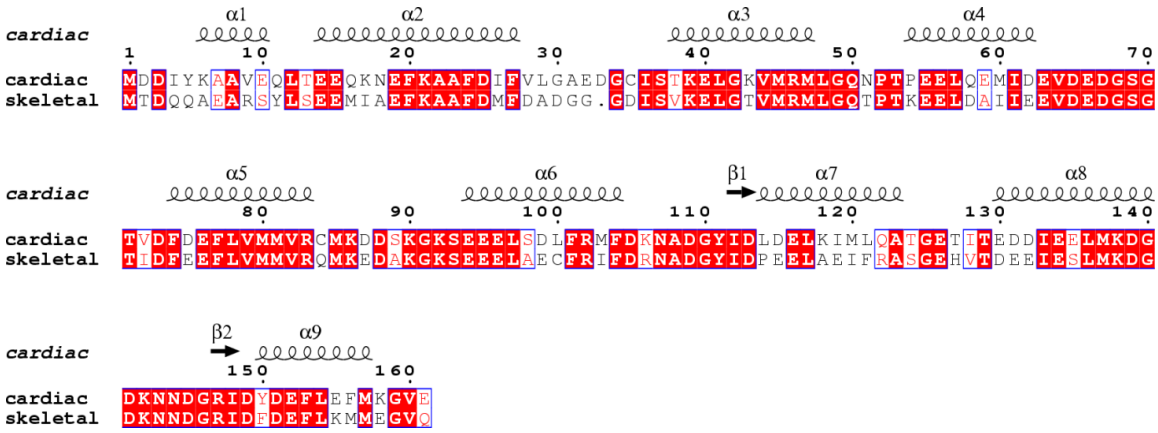

Figure 1-2: Sequence alignment of full-length human cTnC (161 residues) with full-length human sTnC (160 residues).

The secondary structure is shown above the alignment. The sequences were acquired from the Swissprot/TrEMBL database. The accession numbers for cTnC and sTnC is P63316 and P02585, respectively. Absolutely conserved residues are coloured white with red fill, similar residues within groups are coloured red, and similar residues across groups are surrounded by a blue box. The figure was generated using ESPript (Gouet 1999).

Skeletal TnC and cTnC have a very similar protein structure that resembles the shape of a “dumbbell” (figure 1-3). The globular N- and C-terminal domains are connected by a long central α-helix. Each domain contains a pair of an EF-hand (helix-loop-helix) motifs for Ca^{2+} binding (Kretsinger 1973). The four Ca^{2+} binding

sites are numbered I to IV, and the eight α-helices that make up each site are designated by letters A to H from N-terminus to C-terminus (Potter 1975; Zot 1982).

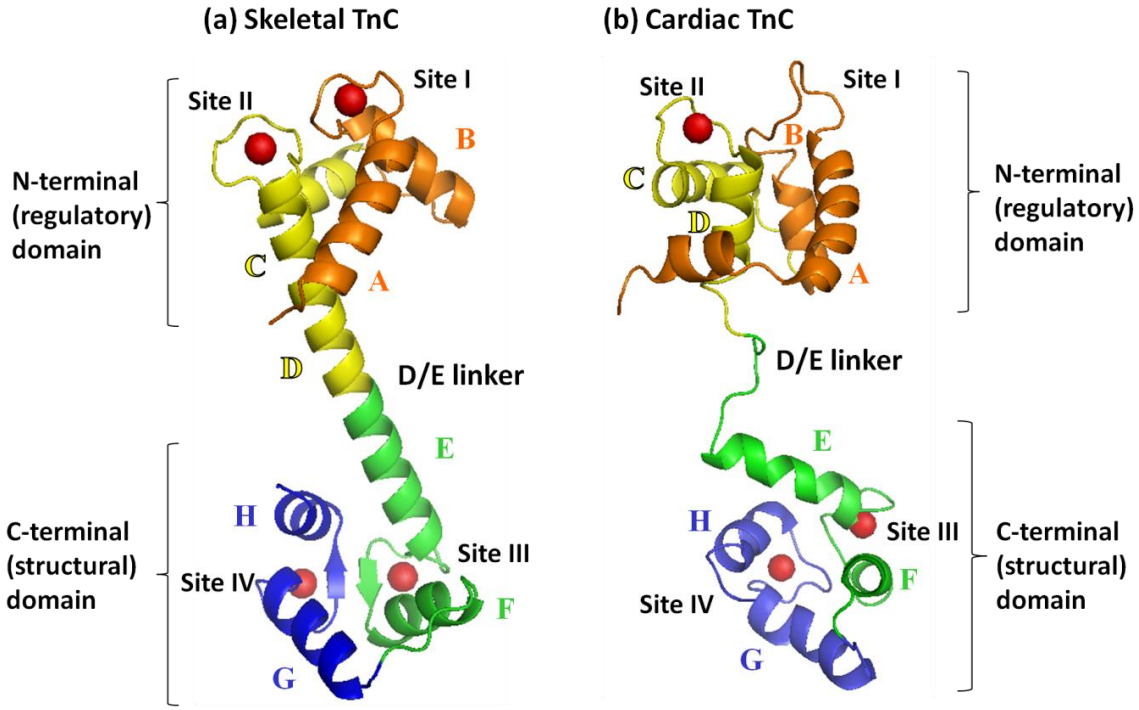

Figure 1-3: Full-length NMR structure of (a) sTnC and (b) cTnC.

(a) A cartoon diagram of the crystal structure of the full length rabbit sTnC (PDB: 1TN4) (Houdusse 1997). Helix A and helix B that make up the first Ca^{2+} binding site I are colored orange, and helix C and helix D that make up the Ca^{2+} binding site II are colored yellow. Helix E and helix F that make up Ca^{2+} binding site III are colored green, and helix H and helix G that make up Ca^{2+} binding site IV are colored blue. The D/E alpha linker connects the N-terminal domain and the C-terminal domain. (b) A cartoon diagram of the NMR structure of the full length chicken cTnC. (PDB: 1LA0) (Dvoretsky 2002). The colour code is the same as in (a). The D/E linker is less defined in cTnC. Only the NMR structure of the full-length cTnC is shown because electron density for the D/E linker of the crystal structure is not observed due to the high flexibility of this region (figure not shown) (Takeda 2003). These figures were generated using PyMol (DeLano 2002).

Site III and site IV in the C-terminal domain have high Ca^{2+} binding affinity and are generally occupied by Mg^{2+} and Ca^{2+} ions under physiological condition. Thus, the C-terminal domain almost always adopts a more “open” conformation, making it a “structural” domain that maintains the integrity of troponin (Potter 1975; Zot 1982). The N-terminal domain has lower Ca^{2+} binding affinity and is more sensitive to physiological Ca^{2+} concentration, making it the “regulatory domain” (Potter 1975; Zot 1982). The main difference between sTnC and cTnC lies within the N-terminal domain. In sTnC, both site I and site II are capable of Ca^{2+} binding. In cTnC, only site II is capable of binding Ca^{2+} while site I is dysfunctional due to a single valine insertion at residue 28 and the substitution of two chelating residues: asparate with leucine at residue 29 and aspartate with alanine at residue 31 (van Eerd 1975).

1.4 Ca^{2+} binding to EF hand and HMJ model

Each functional EF-hand motif consists of 12-13 residues that form a Ca^{2+} binding loop. Residues located at position 1, 3, 5, 7, 9 and 12, denoted as X, Y, Z, -X, -Y, and –Z, are directly involved in Ca^{2+} binding (figure 1-4 (a)) (Strynadka 1989; Marsden 1990). The sequence alignment for all four Ca^{2+} binding loops is shown in figure 1-4 (b). The six residues with either a carboxyl or hydroxyl group contributes an oxygen atom to coordinate Ca^{2+}, and the conserved Glu located at the 12^{th} position contributes two oxygen atoms for binding of Ca^{2+}. Together, the six or seven oxygen atoms coordinate Ca^{2+} in a pentagonal bi-pyramidal arrangement. Figure 1-5 shows the four Ca^{2+} binding sites in the full-length

human cTnC from the troponin complex model (PDB: 1J1D). Site I does not have a Ca^{2+} binding, and site II, III, and IV all show a classical Ca^{2+} coordination. In some structures, formation of a short anti-parallel β-sheet between the two Ca^{2+} binding loop is observed and helps maintain the association of the Ca^{2+} binding loops in each domain (Krudy 1992).

(a)

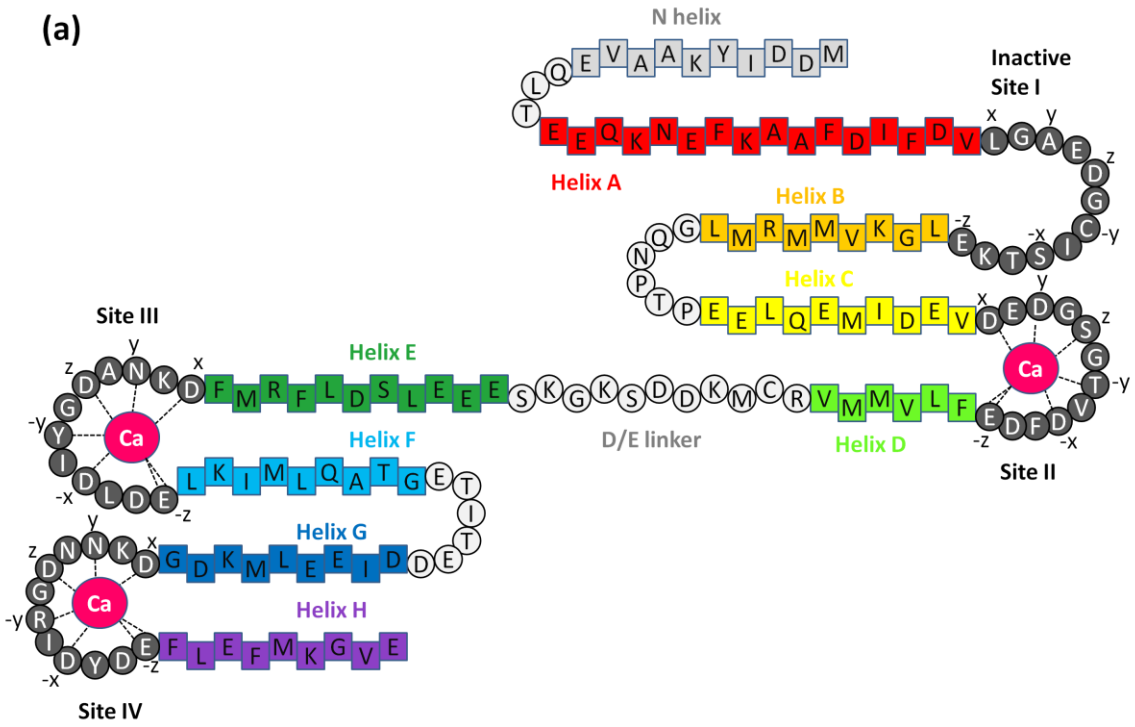

(b)

```
                1                 10
Site_I      VLGAEDGCISTKE
Site_II     .DEDGSGTVDFDE
Site_III    .DKNADGYIDLDE
Site_IV     .DKNNDGRIDYDE
```

Figure 1-4: (a) A schematic representation of the primary and secondary structure of human cTnC with Ca^{2+} binding in each functional binding site and (b) the alignment of the four EF-hand binding motif.

(a) The residues in alpha helices are represented in square, and the residues in beta sheet or random coils are in circles: the ones filled in dark grey participate in Ca^{2+} binding, the ones filled with lighter grey circles are in the loop region, and the ones filled with burgundy participate anti-parallel beta sheet interaction. In each functional Ca^{2+} binding region, the residues labelled X, Y, Z, -Y, -X, and –Z coordinate Ca^{2+} and the coordination bonds are shown in black dashed lines. Helix A-H are labelled and coloured-coded as indicated. Figure was adapted from Krudy, 1992. (b) The sequence alignment of the four EF-hand motif. Site I has 13 residues whereas site II, III, and IV has 12 residues. Absolutely conserved residues are coloured white with red fill, similar residues within groups are coloured red, and similar residues across groups are surrounded by a blue box. The figure is generated used ESPript (Gouet 1999).

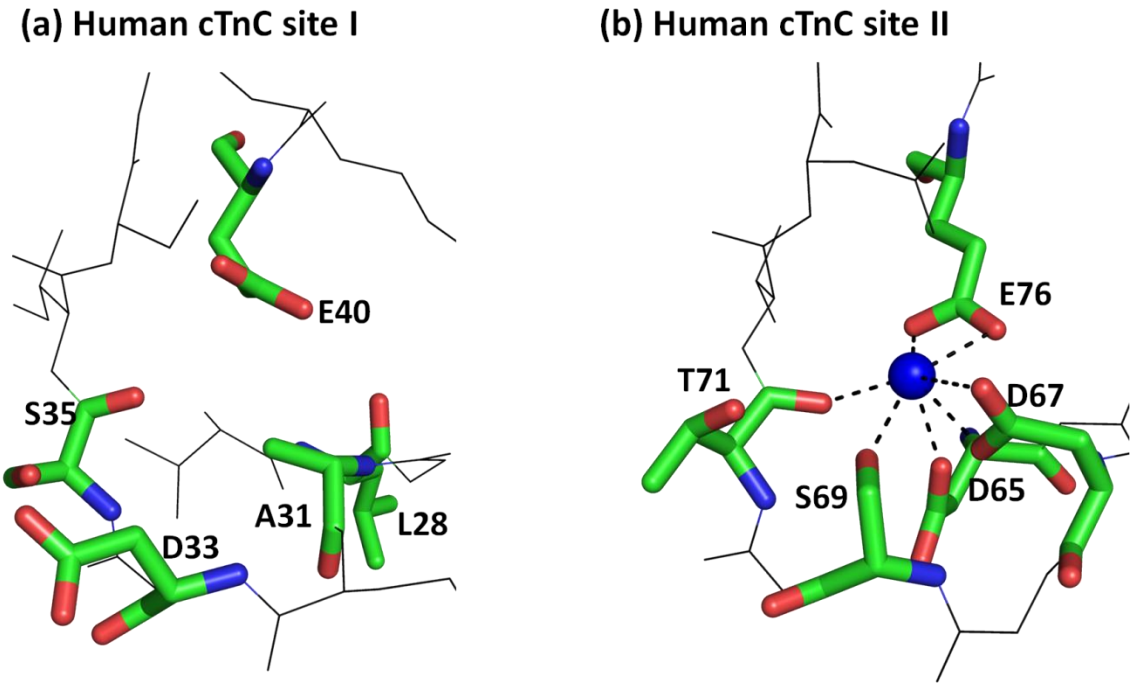

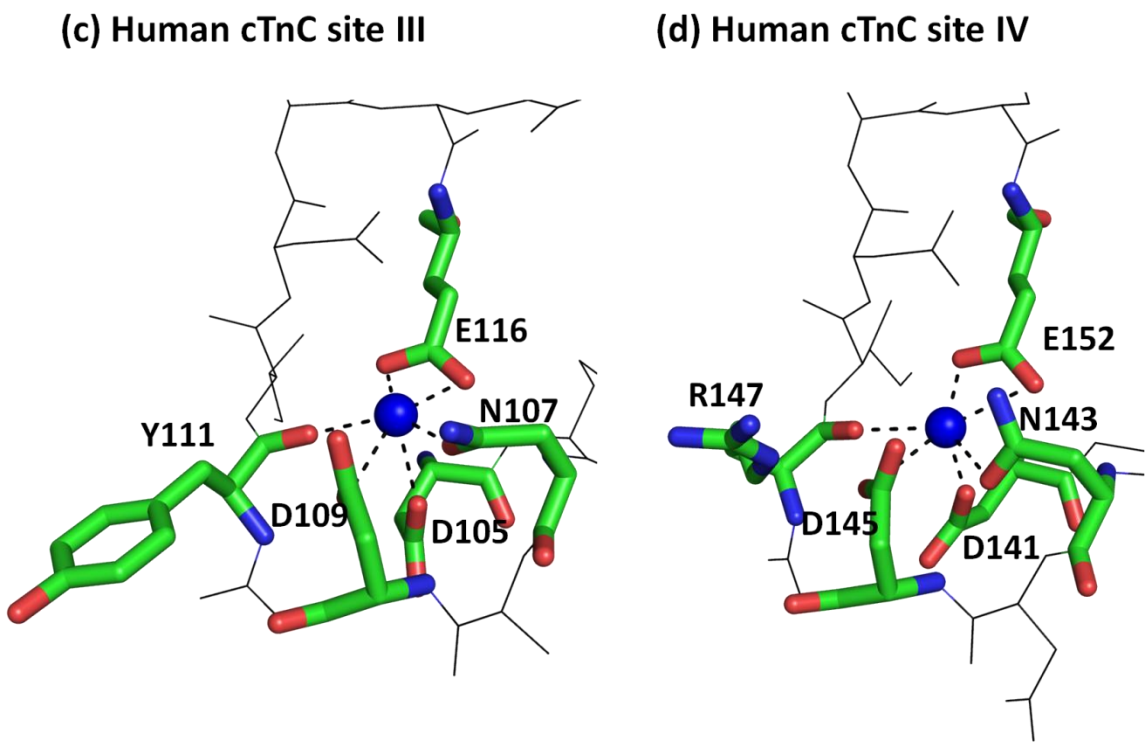

Figure 1-5: The four EF-hand Ca^{2+} binding site in full-length human cTnC (PDB: 1J1D).

Residues that participate in the coordination are shown as green sticks. The Ca^{2+} ion is shown in a blue sphere. (a) The dysfunctional site I. Ca^{2+} ion is not bound in this region. (b) Ca^{2+} binding site II adopts a classical seven-coordination to the Ca^{2+} ion. (c) Ca^{2+} binding site III adopts a six-coordination to the Ca^{2+} ion. (d) Ca^{2+} binding site IV adopts a six-coordination to the Ca^{2+} ion. The figures were generated using PyMol (DeLano 2002).

In 1985, the first crystal structure of sTnC was solved by two groups: Herzberg *et. al.* solved the crystal structure of turkey sTnC at 2.8 Å resolution (Herzberg 1985), and Sundaralingam *et. al.* solved the structure of chicken sTnC at 3.0 Å resolution (Sundaralingam 1985). These TnC crystal structures have the N-terminal domain free of Ca^{2+} and C-terminal domain saturated with two Ca^{2+}. Helix F, helix G, and helix H in C-terminal domain are oriented almost perpendicular to the central helix, whereas helix B and helix C in N-terminal

domain are oriented nearly parallel to the central helix. Although the sequence identity between the N- and C-terminal domain is only 26%, the overall structure is almost identical (figure 1-6). Therefore, Herzberg, Moult, and James proposed the “HMJ model” to describe the Ca^{2+} induced conformational change of the N-terminal domain based on the structure of the skeletal TnC (Herzberg 1986). It was proposed that as the N-terminal domain changes from a “closed” state to an “open” state upon Ca^{2+} binding, the positions of helix B and helix C are reoriented from being parallel to the central helix to almost perpendicular to it. The position of helix B and helix C change dramatically with an angle difference of almost 50° (figure 1-7). This reorientation of helices exposes the hydrophobic residues of the central helix, where the inhibitory domain of TnI binds and triggers the overall conformational change of the troponin complex.

Figure 1-6: The superposition of chicken skeletal N-domain of TnC from residue 1-90 (black) and C-domain from residue 91-161 (white) (PDB: 1YTZ).

The overall conformation of the two domain is almost identical in a Ca^{2+} bound form. The only difference is that the N-teminal domain has an extra short N-helix at the N-terminus. Ca^{2+} is shown as a blue sphere.

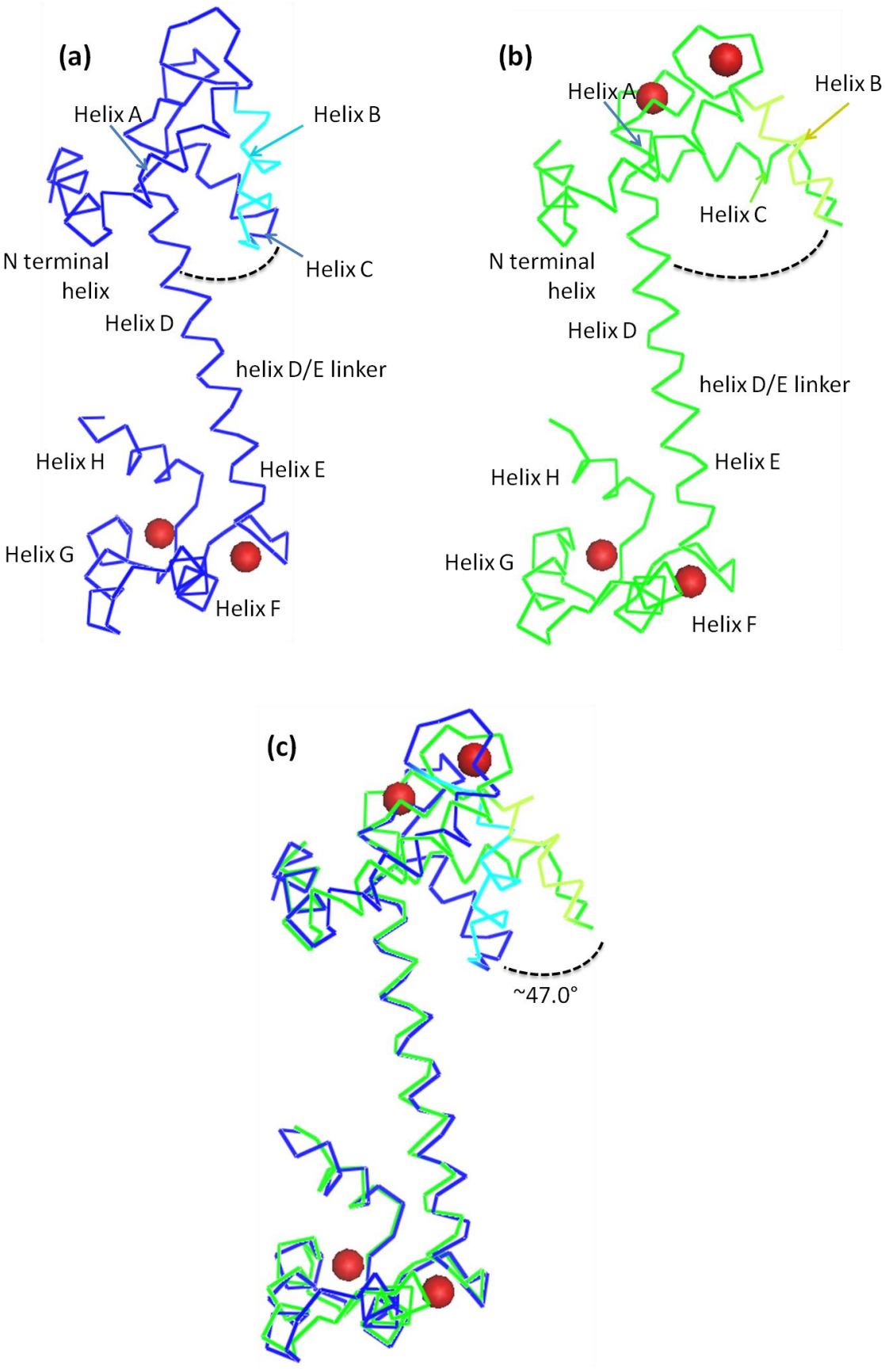
(a)
Helix A
Helix B
N terminal helix
Helix C
Helix D
helix D/E linker
Helix H
Helix E
Helix G
Helix F
(b)
Helix A
Helix B
Helix C
N terminal helix
Helix D
helix D/E linker
Helix H
Helix E
Helix G
Helix F
(c)
~47.0°

Figure 1-7: A Cα-trace of sTnC that shows the difference between Ca^{2+}-free and Ca^{2+}-bound structure of sTnC.

(a)The ribbon representation of the full length chicken Ca^{2+}-free sTnC. Helix B is shown in cyan colour. Helix B and helix C are located close to the central helix. (PDB code: 1TOP) (Satyshur 1988). (b) The ribbon representation of Ca^{2+}- bound skeletal TnC. Helix B is shown in lemon colour. Helix B and helix C are located almost perpendicular to the central helix (PDB code: 1TN4) (Houdusse 1997). (c) The superimposed skeletal TnC structure of (a) and (b). The largest angle difference of helix B/C between Ca^{2+}-free form and Ca^{2+} bound form is approximately 47.0°. The position of the helices in C-terminal domain, helix E-H, remain the same as the Ca^{2+} binding sites III and site IV are bound to Ca^{2+} in both forms. These figures are prepared using PyMol (DeLano 2002).

The HMJ model was verified by several biophysical experiments and site-specific mutations in certain residues of TnC. For example, in order to confirm the movement of helix B and helix C with respect to the central helix upon Ca^{2+} binding, Gragarek *et.al.* incorporated a disulfide bond between the linker region of helix B and C and the central helix to restrict the movement. As predicted, its Ca^{2+} binding ability was significantly decreased and its ability to regulate actomyosin ATPase activity was almost completely lost (Grabarek 1990). This decrease in Ca^{2+} sensitivity was also observed in an experiment done by Fujimori *et. al.*, in which a potential salt bridge was introduced between helix C and helix D in a Ca^{2+} free state (Fujimori 1990). These experiments agree with the hypothesis of the HMJ model. Finally, the model was conclusively confirmed by the crystal structure of rabbit sTnC that is completely saturated with Ca^{2+} (Houdusse 1997).

All the conformational changes of TnC depicted in the HMJ model describe the characteristics of sTnC. Cardiac TnC, however, does not have a

functional Ca^{2+} binding site I. Thus, the conformational change triggered by Ca^{2+} binding to N-terminal domain is less in cTnC than in sTnC (figure 1-8). Cardiac TnC tends to have a more closed conformation even when it is in a Ca^{2+}-bound state.

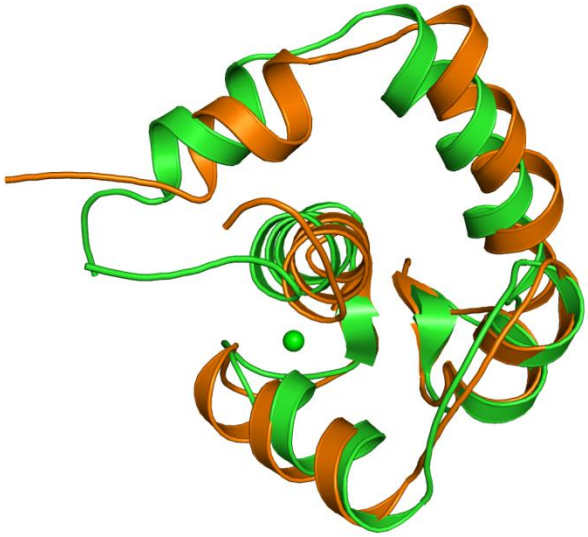

Figure 1-8: Superposition of the NMR structure of Ca^{2+}-free human N-cTnC (orange, PDB: 1SPY) with the NMR structure of Ca^{2+}-bound human N-cTnC (green, PDB: 1AP4).

Since structural data for the full-length Ca^{2+}-free cTnC is not available, only N-cTnC domain is used for comparison. The structural change shown here is much less dramatic than that of sTnC.

Despite this conformation, cTnC is still able to regulate the interaction of actin with myosin, which implies that the Ca^{2+} binding site II plays a significant role in regulating the activity of troponin complex. Sweeney *et. al.* constructed two cTnC mutants using mutagenesis to study the Ca^{2+} binding affinity of site I. One mutant has an active site I (L29D, G30A, A31D, E32G) and an active site II, while the other mutant has an active site I but an inactive site II (V28, L29D,

G30A, A31D, E32G, D65A) . Both constructs were able to associate with cTnI and cTnT to form a troponin complex and integrated in the slow-twitch skeletal muscle fibres. However, the cTnC with the mutated active site I was unable to restore Ca^{2+}-dependent contraction to TnC-depleted skinned slow muscle fibres. Only the one with wild type active site II was capable of restoring Ca^{2+}-dependent contraction. This demonstrates that only site II in cTnC can trigger muscle contraction in slow-twitch skeletal muscle fibres (Sweeney 1990). Similar results were obtained by Gluati *et al*'s experiments, in which the first 41 residues of sTnC were replaced with that of cTnC. This chimeric protein expressed the cardiac phenotype that is still capable of triggering conformational change despite of the inactivity of site I (Gulati 1992), suggesting that site II is important for cTnC to function. Finally, the difference in the Ca^{2+}-saturated N-terminal domain between cTnC and sTnC is demonstrated more clearly in the NMR structure of human N-cTnC (Sia 1997; Spyracopoulos 1997).

For sTnC, the Ca^{2+}-free form (figure 1-9 (a)) is remarkably different from that of Ca^{2+}-bound form (figure 1-9 (b)). Upon Ca^{2+} binding to site I and site II, all helices move with the largest difference in the relative orientation of helix B and helix C. Both helix B and helix C move outward in order to accommodate the Ca^{2+}, with the angle difference of ~45°and ~40°, respectively (figure 1-9 (c)). On the other hand, cTnC does not change its conformation as dramatically as sTnC. Since only site II is functional in cTnC, the relative orientation of helix B and helix C does not change as much compared to sTnC (figure 1-9 (f)). Thus, the overall

conformation of the Ca^{2+}·cTnC resembles more to that of apo sTnC (figure 1-9 (i)) rather than Ca^{2+}·sTnC, remaining in a more “closed” conformation.

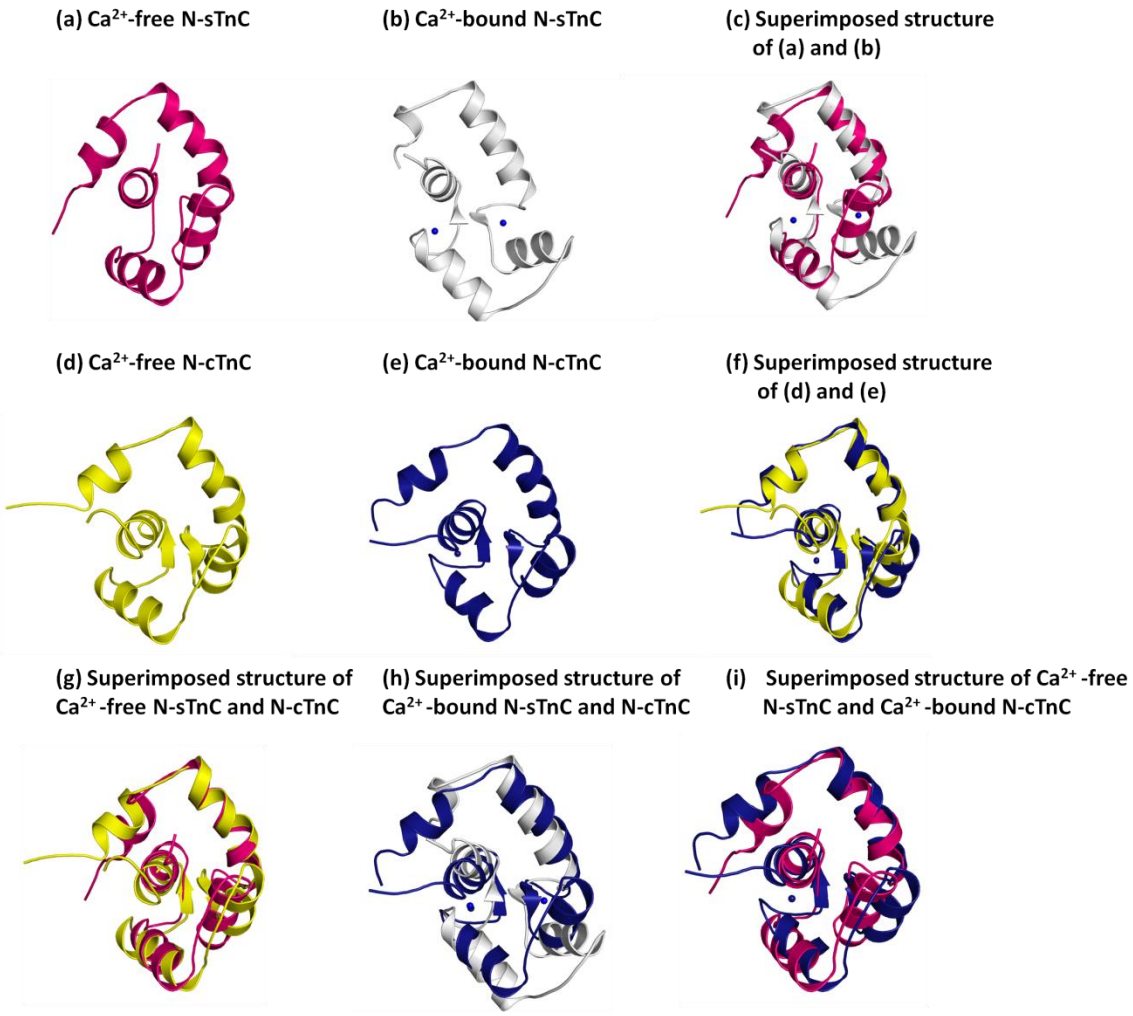

Figure 1-9: Cartoon representations of skeletal and cardiac TnC in Ca^{2+}-free and Ca^{2+}-bound form.

(a) An averaged NMR structure of Ca^{2+}-free chicken N-sTnC (PDB: 1SKT) (Tsuda 1999) ; (b) the crystal structure Ca^{2+}-bound chicken N-sTnC (PDB: 1AVS) ((Spyracopoulos 1997; Strynadka 1997); (c) the superimposed structure of Ca^{2+}-free and Ca^{2+}-bound N-sTnC. The structural difference is mainly observed in helix B and helix C. (d) An averaged NMR structure of Ca^{2+}-free human N-cTnC (PDB: 1SPY) (Spyracopoulos 1997); (e) an averaged NMR structure of Ca^{2+}-bound human N-cTnC (PDB: 1AP4) (Spyracopoulos 1997); (f) the superimposed structure of Ca^{2+}-free and Ca^{2+}-bound N-cTnC. The structural difference is less obvious in N-cTnC but is still observed in helix B. (g) The superimposed structure of Ca^{2+}-free chicken N-sTnC (pink) and Ca^{2+}-free human N-cTnC (yellow). Some structural difference is shown in helix B and helix C. (h) The superimposed structure of Ca^{2+}-bound chicken N-sTnC (white) and Ca^{2+}-bound human N-cTnC (blue). The obvious structural difference is shown in helix B. (i) The superimposed structure of Ca^{2+}-free N-sTnC and Ca^{2+}-bound N-cTnC. This figure shows that the structure of Ca^{2+}-bound N-cTnC resembles more to the Ca^{2+}-free N-sTnC since the Ca^{2+}-bound N-cTnC does not have a large conformational change upon Ca^{2+} binding. These figures were generated using PyMol (DeLano 2002).

1.5 Mutation in troponin C and its relation to familial hypertrophic cardiomyopathy

Mutations associated with each subunit of troponin complex can lead to various cardiovascular diseases, including one of the most common inherited cardiac muscle disorders, familial hypertrophic cardiomyopathy (FHC) (Fatkin 2002; Gomes 2004). It affects 1 in every 500 people, and is also the leading cause of sudden death for competitive athletes and young people under the age of 35 (Fatkin 2002; Gomes 2004). A distinct feature of FHC is that it has a wide range of clinical diversity. Patients diagnosed with FHC can show no or minimal symptoms; in some serious cases, FHC can develop into congestive heart failure and cause sudden death. Two hundred and forty protein mutations have been shown to date to cause FHC, and 50 of them arise from the troponin subunits, particularly within cTnI and cTnT (Gomes 2004). The first mutation found in cTnC

causes FHC is the single amino acid substitution of leucine with glutamine at residue 29 (L29Q) (Hoffmann 2001). It was found in a living 60-year-old male patient who still had preserved diastolic and systolic function. In addition, there are four more recently found cTnC mutants involved in FHC, including A8V, C84Y, E134D, and D145E (Pinto 2009). Circular dichroism measurements in different metal bound states of A8V, C84Y, and D145E cTnC mutants demonstrated changes in the secondary structure, while E134D was the same as the wild type. Since L29Q was involved in this project, it will be discussed in a greater detail.

During systole, Ca^{2+} binds to the regulatory domain of TnC and triggers a conformational change. This exposes a hydrophobic patch of TnC for TnI to bind, which causes TnI to release its inhibitory binding from the actin. This allows cross-bridge cycling and leads to muscle contraction. Afterwards, a fast relaxation of the muscle is required to allow an adequate amount of time to refill the heart with blood. This process is termed diastole, which is an important process for proper heart relaxation between each muscle contraction. This relaxation process is further enhanced by the phosphorylation of serine 23 and serine 24 of N-terminal arm of TnI by protein kinase A (Finley 1999; Kentish 2001). When these residues are phosphorylated, it weakens the interaction between non-phosphorylated residues TnI and TnC. As a result, the biphosphorylated TnI arm is released from TnC, facilitating Ca^{2+} to dissociate from the regulatory domain of TnC (Robertson 1982; Finley 1999; Ward 2004).

Thus, PKA phosphorylation of TnI leads to the decreased Ca^{2+} affinity of troponin, hence increase cross bridge cycling and facilitate the relaxation of muscle.

Leucine 29 of TnC is located at the surface of N-TnC in the dysfunctional Ca^{2+} binding site I (figure 1-10 (a)). Although it is not directly involved in Ca^{2+} binding, it is important in maintaining the structural integrity of helix A of N-cTnC (Sia 1997). It is located at the interaction site with the cardiac-specific non-phosphorylated N-terminal arm of cTnI (Finley 1999; Schmidtmann 2005). The replacement of a non-polar leucine with a polar glutamine may have an impact on overall function of troponin with tropomyosin. However, how exactly this mutation affects the Ca^{2+} sensitivity of TnC is still under debate (Dweck 2008). Several studies show that in the absence of phosphorylated TnI, the L29Q mutation can decrease, increase, or have no affect on Ca^{2+} sensitivity (Schmidtmann 2005; Baryshnikova 2008; Liang 2008).

According to CD spectroscopy data collected by Schmidtamnn *et. al.*'s, L29Q shows a loss of 2% helical content compared to the wild type, suggesting a possible destabilization of helix A (Schmidtmann 2005). Due to this loss of structural integrity, they hypothesized that the interaction between other residues in helix A of TnC and non-phosphorylated residues of TnI may be disrupted. In addition, their *in vitro* assay conducted on L29Q shows that the Ca^{2+} sensitivity of the ATPase in the reconstituted thin filament is no longer affected by PKA-dependent phosphorylation of TnI (Schmidtmann 2005). This finding implies that L29Q may decrease the Ca^{2+} sensitivity and disturb the transduction of the signal from the phosphorylated TnI to TnC. However, the former finding presents a

contradiction to the dogma because FHC-associated cardiomyopathy generally has a higher myofilament Ca^{2+} sensitivity (Karibe 2001; Gomes 2004; Chang 2005). Conversely, Liang *et. al.* demonstrated that L29Q significantly increases the Ca^{2+} sensitivity of force generation from the muscle when it is incorporated in a single skinned cardiac myocyte (Liang 2008). Phe^{27} → Trp substitution was used as a fluorescence reporter to monitor the Ca^{2+} binding *in vitro* and exchange with Ca^{2+} binding site II of TnC. They also studied the effect of these mutants on the sarcomere length (SL) dependence, which is an important factor that affects the Ca^{2+} sensitivity. The results showed that L29Q has a significantly increased Ca^{2+} binding affinity compared to the wild type, and its response to change in sarcomere length was significantly reduced. Recent NMR titration and UV/Vis titration studies showed that L29Q essentially has the same Ca^{2+} affinity as that of wild type TnC (Baryshnikova 2008). Therefore, the nature of the effect of this mutation and its relation to FHC still remain unclear. However, the use of experimental techniques can account for the different results. For instance, using a single cardiac myocyte lacks the geometric and mechanical constraints from other proteins within the sarcomere (Liang 2008). Using NMR technique prevents the use of Ca^{2+} chelator such as EGTA, so the concentration of the free Ca^{2+} in the μM range might not be accurately assessed (Liang 2008). Thus, from Liang *et. al.*'s experiment, which was conducted using single cardiac myocytes held at a constant sarcomere length, can be more precise and closer to the physiological condition.

In addition to the mutant L29Q cTnC, another mutant that has four amino acid substitutions, D2N, V28I, L29Q, and G30D (NIQD) was identified by our collaborator (Gillis 2005). It has a two-fold higher Ca^{2+} binding affinity compared to the wild type cTnC (Gillis 2005). This mutant was generated on comparing Ca^{2+} binding affinity between salmonid cTnC and bovine cTnC. By making a series of mutations, four amino acid substitutions in salmonid cTnC were identified to be responsible for the higher Ca^{2+} binding affinity (figure 1-10 (b)). Therefore, by studying the wild type human N-cTnC, L29Q, and NIQD mutant N-cTnC can provide an important insight on how these mutations affect the structural changes of N-cTnC and its Ca^{2+} binding affinity.

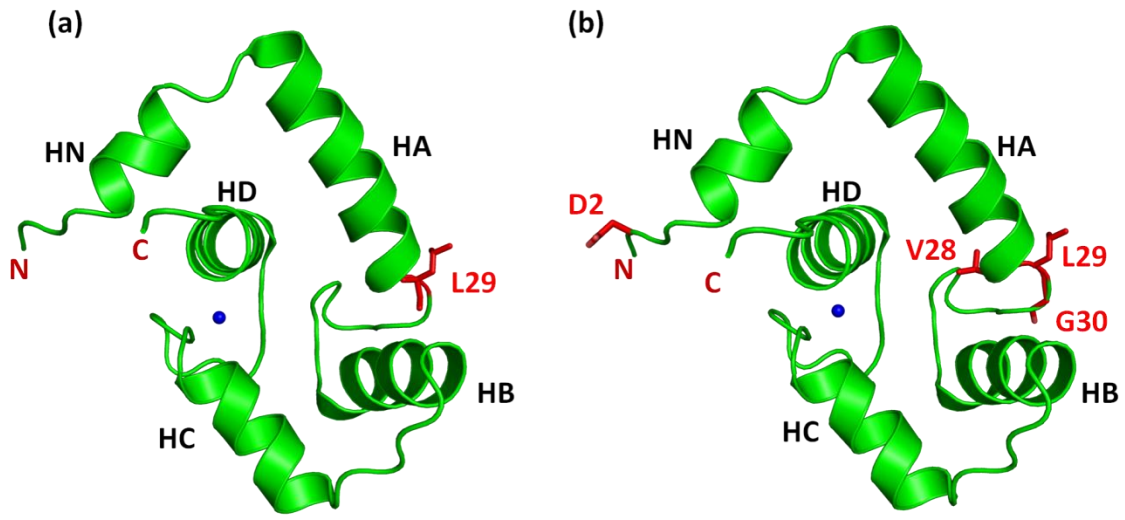

Figure 1-10: The cartoon representation of N-cTnC with (a) L29 highlighted and with (b) D2, V28, L29, and G30 highlighted (PDB: 1J1D).

(a) Residue L29 is located on the beginning of the inactive Ca^{2+} binding site I. Substitution of the non-polar leucine to polar glutamine may have some potential interaction with solvent and change the overall conformation. It is also important in maintaining the structural integrity of helix A of N-cTnC. (b) It was shown that by having mutation at the four following sites, D2, V28, L29, and G30 to D2N, V28I, L29Q, and G30D (NIQD), can have an significant increase in Ca^{2+} affinity although most of these residues are located in the inactive binding site I (Liang 2008).

1.6 Three dimensional structure of cardiac TnC

To date, there are 17 NMR structures and 5 crystal structures of cTnC and cTnC-related structure deposited in the PDB. Unlike the structure of sTnC, most cTnC structures were solved by NMR spectroscopy, including chicken, trout, rabbit, and human cTnC (table 1-1), and most of them are N-terminal cTnC structure. Since this project focuses on mammalian cardiac TnC, several important structures of cTnC are discussed in details in the following sections.

Table 1-1: The previously-solved cTnC related structures. If Ca^{2+} is included in the final structure, then an X is marked in the "Ca^{2+}-BOUND" category; if Ca^{2+} is not included in the final structure, the an X is marked in the "Ca^{2+}-FREE" category.

PDB CODE	CONSTRUCT	Ca^{2+}-FREE	Ca^{2+}-BOUND	METHOD	REFERENCE
Full-length					
2JT0	Human mutant F104W cTnC		X	NMR	Wang, 2007 Protein Sci.
2CTN	Chicken cTnC		X	NMR	
2JT3	Human mutant F153W cTnC		X	NMR	Wang, 2007 Protein Sci.
3CTN	Chicken cTnC	X		NMR	Sia 1997 J.Biol.Chem.
N-cTnC					
1AP4	Human N-cTnC		X	NMR	Li, 1997 Biochemistry
1R2U	Trout N-cTnC at 30°C		X	NMR	Blumenschein, 2003 Biochemistry
1R6P	Trout N-cTnC at 7°C		X	NMR	Blumenschein, 2003 Biochemistry
1SPY	Human N-cTnC	X		NMR	Spyracopoulos, 1997 Biochemistry
2JXL	Human mutant F77W-V82A		X	NMR	Julien, 2007 Biochemistry
C-cTnC with cTnI peptide					
1FI5	Chicken C-cTnC with N-cTnI (residue 33-80)		X	NMR	Gasmi-Seabrook, 1999 Biochemistry
1SBJ	Chicken C-cTnC with N-cTnI (residue 33-80)		X (Mg^{2+})	NMR	Finley, 2004 Biochemistry
1SCV	Chicken C-cTnC with N-cTnI		X	NMR	Finley, 2004 Biochemistry
1OZS	Human C-cTnC with cTnI peptide		X	NMR	Lindhout, 2003 J. Biol. Chem.
Full length, N-cTnC complexed with cTnI peptide or drug					
1DTL	Chicken cTnC with bepridil		X	X-ray crystallography	Li, 2000 Proc.Natl.Acad.Sci
1LXF	Human N-cTnC with cTnI peptide (147-163) and		X	NMR	Wang, 2002 J. Biol. Chem.

	bepridil				
1WRK	Human N-cTnC with TFP (orthorhombic crystal form)		X	X-ray crystallography	Takeda, 2004 To be published
1WRL	Human N-cTnC with TFP (monoclinic crystal form)		X	X-ray crystallography	Takeda, 2004 To be published
Cardiac troponin core complex					
1J1D	Human troponin (46kDa)		X	X-ray crystallography	Takeda, 2003 Nature
1J1E	Human troponin (52 kDa)		X	X-ray crystallography	Takeda, 2003 Nature

1.6.1 **TnC in complex with TnI and binding drug**

It is apparent that the interaction between cTnC and cTnI plays a significant role in transmitting Ca^{2+} dependant signal transduction to other proteins during cardiac muscle contraction. The cTnC and cTnI interface provides a potential drug target in treating cardiovascular disease. A substantial effort has been made to design a series of Ca^{2+} sensitizing or desensitizing drugs, including bepridil, trifluoperazine, anapoe, and the thiadiazinone derivative EMD 57033 (Li 2000; Takeda 2004; Vinogradova 2005; Takeda 2006; Li 2008). Figure 1-11 shows the drug binding site to the N-terminal and C-terminal domain of cTnC.

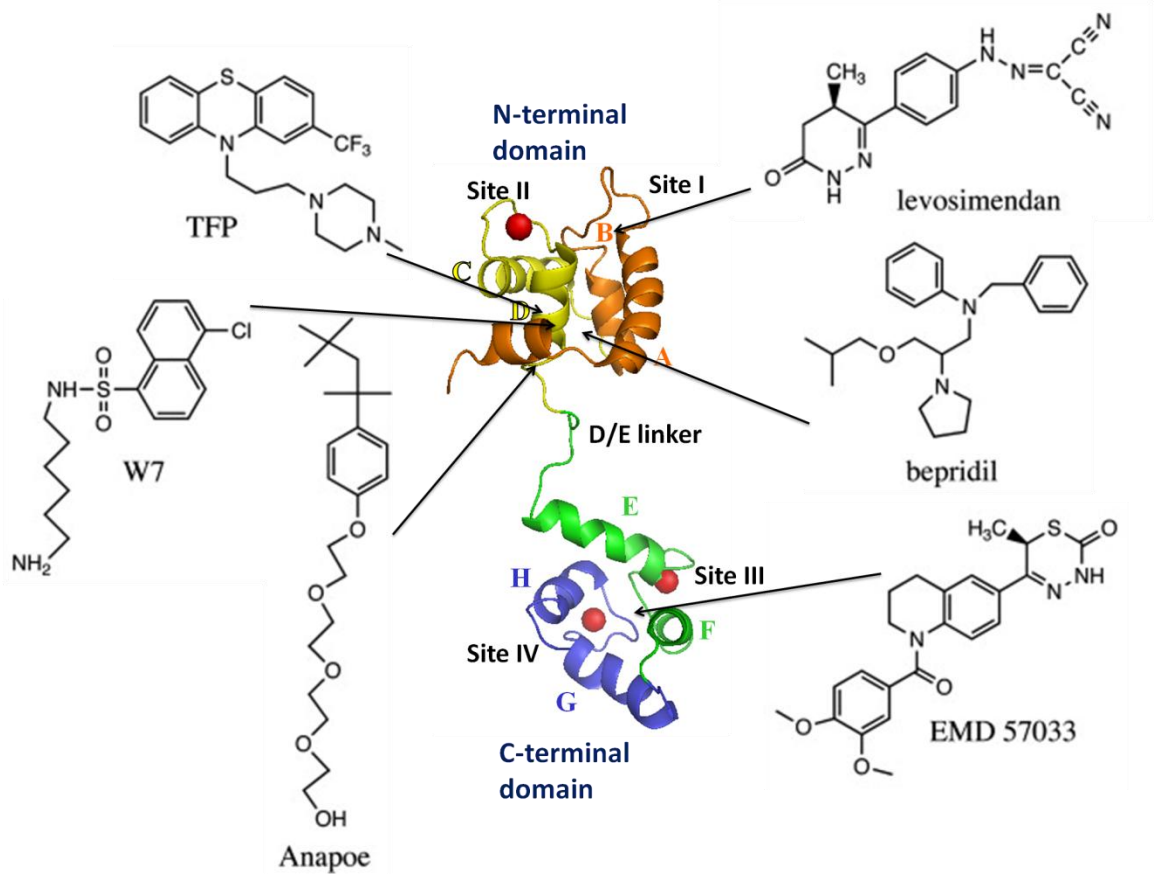

Figure 1-11: The chemical structures of Ca^{2+} sensitizing drugs and their binding site on TnC.

Levosimendan, TFP, bepridil, anapoe, and W7 are the Ca^{2+} sensitizing drugs that bind to N-TnC; EMD 57033 binds to C-TnC (PDB: 1AP4). The figure is adapted from (Li 2008).

1.6.2 **Bepridil**

Bepridil is a Ca^{2+} channel blocker that is able to enter cardiomyocytes and bind to the thin filament (Cramb 1983; Solaro 1986). From the early evidences, bepridil was shown to bind directly to Ca^{2+} saturated TnC and enhances Ca^{2+}

binding to the regulatory site in both free solution and muscle skin fibre (Solaro 1986). Several NMR studies also suggest the possible binding sites of bepridil, two are found in the C-terminal domain of cTnC and one within the N-terminal domain (Kleerekoper 1998; Abusamhadneh 2001). The binding sites and effect of bepridil on cTnC were further confirmed by the X-ray structure of chicken full-length cTnC with three bepridil molecules bound (PDB: 1DTL) (Li 2000) and the NMR structure of the ternary complex of N-cTnC·Ca^{2+}·$cTnI_{147-163}$ ·bepridil (1LXF) (Wang 2002).

The X-ray structure of three bepridil molecules bound to Ca^{2+}-saturated cTnC shows an overall compact shape of TnC (figure 1-12). Two bepridil molecules are located at the hydrophobic cavity between the N- and C-terminal domains, pulling them together to form the compact shape of TnC. The third bepridil is located at the hydrophobic cavity of the N-terminal domain, stabilizing the open Ca^{2+}-bound conformation of N-cTnC (Li 2000). The authors proposed that the two bepridil located between the two domains would be replaced by the presence of cTnI in the troponin complex, and the third bepridil that binds to N-cTnC slows down the Ca^{2+} release by stabilizing the open conformation. With their biochemical data that also show increased Ca^{2+} affinity by bepridil, they concluded that bepridil is able to enhance Ca^{2+} sensitivity of the myofilament by stabilizing the Ca^{2+} induced open form. However, this finding did not agree with other biochemical data, in which bepridil is shown to be an ineffective pharmacological Ca^{2+} sensitizer for treating heart failure associated with increased Ca^{2+} sensitivity (Gill 1992). This controversy led Wang *et. al.* to solve

the NMR structure of the ternary complex of N-cTnC·Ca^{2+}·$cTnI_{147-163}$ ·bepridil which provides a more clear answer to the effect of bepridil on cTnC.

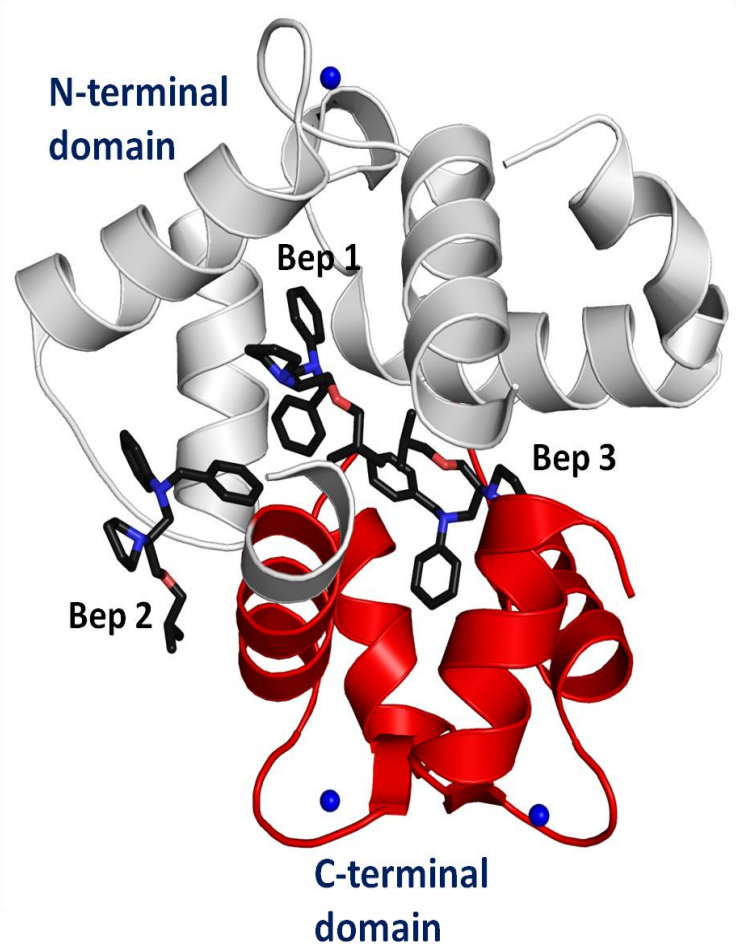

Figure 1-12: The structure of full-length chicken cTnC complex with three bepridil molecules.

Bepridil 1, 2, and 3 are coloured black (PDB: 1DTL). Bep2 and Bep 3 are located at the interface between the N-terminal domain (white) and C-terminal domain (red). The binding of the bepridil molecules brought the two domain together to form a compact globular conformation. The figure is generated using PyMol (DeLana 2002).

The NMR structure of the ternary complex of N-cTnC·Ca^{2+}·$cTnI_{147-163}$ ·bepridil shows the binding site of $cTnI_{147-163}$ is located at the interhelical interface formed by helix A and helix B of cTnC, whereas the binding for bepridil is in the hydrophobic cavity (figure 1-13) (Wang 2002).

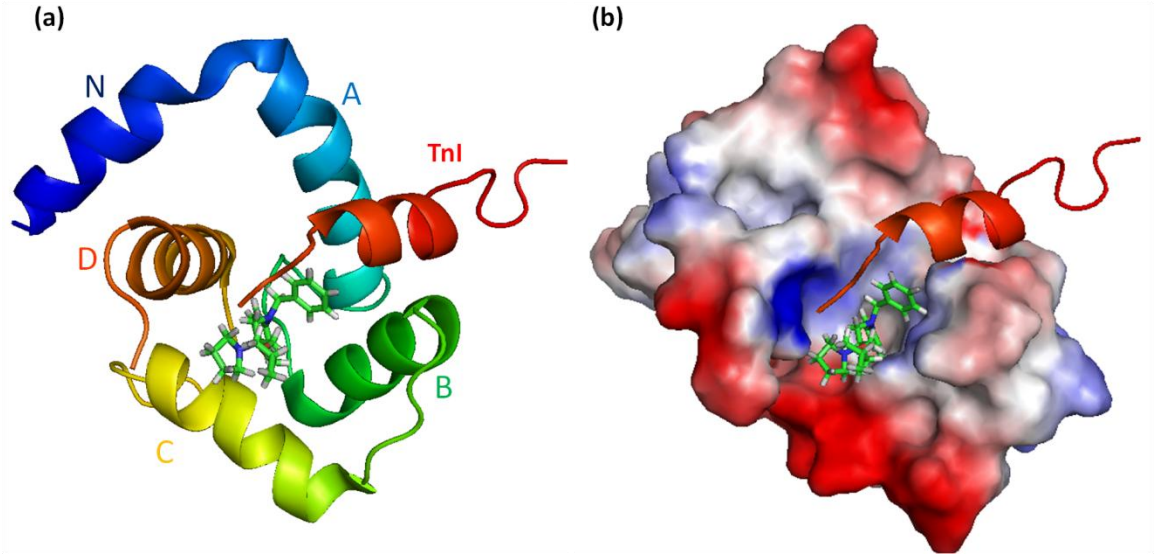

Figure 1-13: (a) cartoon representation of the NMR structure of the ternary complex of N-cTnC·Ca^{2+}·$cTnI_{147-163}$ ·bepridil (PDB: 1LXF) and (b) the electrostatic representation of the same model.

(a) The cartoon representation of the complex. Bepridil molecule is modelled as the green stick. $TnI_{147-163}$ is located between helix A and helix B. (b) The electrostatic representation of N-cTnC. The positively-charged area is colored in blue, and the negatively-charged area is colored in red. The neutral region is colored in white. The figures were generated using PyMol (DeLana 2002).

From 2D NMR spectroscopy experiments, bepridil was shown to bind to $cTnI_{147-163}$ and N-cTnC·Ca^{2+} simultaneously. However, in the presence of bepridil,

binding affinity for $cTnI_{147-163}$ to Ca^{2+}·cTnC is reduced by 3.5 fold and *vice versa* (Wang 2002). Figure 1-14 summarizes the effect of Ca^{2+}, $cTnI_{147-163}$, and bepridil on cTnC. Although bepridil appears to set the stage for the binding of $cTnI_{147-163}$, the ternary complex is very unstable as the Kd of cTnC for cTnI increases dramatically. This negative cooperativity between bepridil and $cTnI_{147-163}$ can be caused by two interactions. First, clashes are observed between the N-terminus of the TnI peptide and part of the bepridil molecule. Second, the positively charged R147 of $cTnI_{147-163}$ and the partial positive charge of the pyrrolidine group of bepridil generates an unfavourable repelling force. As a result, bepridil binds more weakly to the regulatory domain of N-cTnC·Ca^{2+}·$cTnI_{147-163}$ complex than binding to cTnC alone (Abusamhadneh 2001). This could explain why bepridil is not an effective Ca^{2+} sensitizer and its poor pharmacological effect. Since it decrease the binding affinity of TnI to TnC, it may be used as a potential Ca^{2+}-desensitizer for treating cardiac dysfunction associated with increased Ca^{2+} sensitivity, such as FHC.

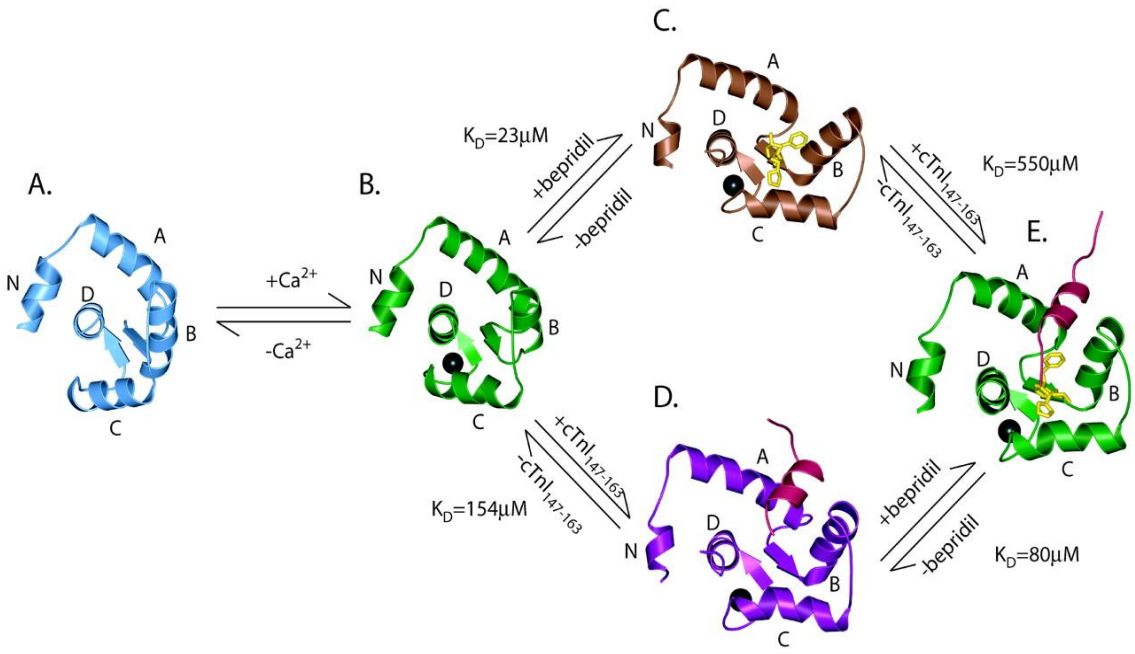

Figure 1-14: A stepwise mechanism of the effects of Ca^{2+}, bepridil, and the $cTnI_{147-163}$ peptide on the conformation of N-cTnC.

A) apo N-cTnC. B) N-cTnC bound with Ca^{2+}. C) N-cTnC·Ca^{2+} bound with bepridil. D) N-cTnC·Ca^{2+} bound with $cTnI_{147-163}$. E) N-cTnC·Ca^{2+} bound with both $cTnI_{147-163}$ and bepridil. Source from Wang *et. al.*, J. Biol. Chem. (Wang 2002).

1.6.3 **Trifluoperazine (TFP)**

TFP is an antipsychotic drug of the phenothizaine group that was shown to increase the Ca^{2+} affinity of TnC (Silver 1986). The X-ray crystal structure of TFP complexed with N-cTnC was solved by Takeda *et. al.* (figure 1-15(a)) (Takeda 2006). One TFP molecule is located in the hydrophobic area formed by helix A and helix D, the binding location of cTnI in the ternary complex of N-cTnC·Ca^{2+}·$cTnI_{147-163}$ ·bepridil. The second TFP molecule is located on the hydrophobic cavity formed by helix B and helix C, and it does not interfere with cTnI binding. Previous NMR studies show that the second TFP molecule is

capable of conferring a Ca^{2+} sensitizing effect while the first TFP molecule is likely to inhibit the cTnI association with cTnC (Kleerekoper 1998).

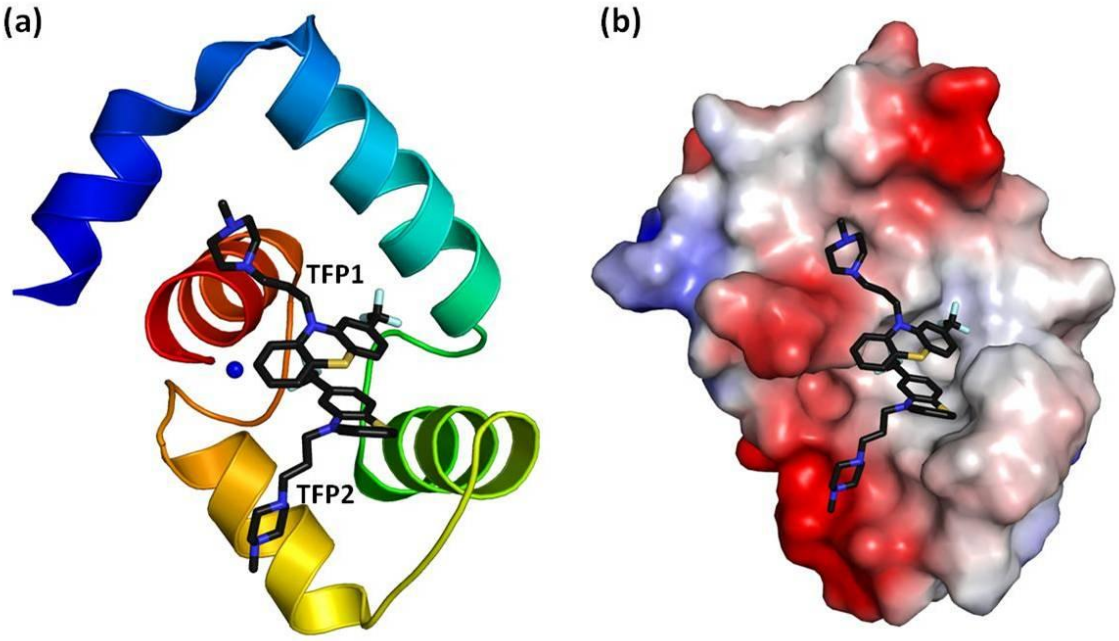

Figure 1-15: (a) The crystal structure of N-cTnC-Ca^{2+} bound with 2 TFP molecules. (PDB: 1WRK; Takeda *et. al.* 2003) and (b) the electrostatic representation of 1WRK with 2TFP molecules bound.

(a) Cartoon rendering coloured spectrally from the N-terminus (red) to the C-terminus (red). TFP molecules are presented as the black stick model. (b) The electrostatic representation of the same structure. The positively-charged area is colored in blue, and the negatively-charged area is colored in red. The neutral region is colored in white. The figure is generated using PyMol (DeLano 2002).

1.6.4 **Levosimendan**

Levosimendan is a calcium sensitizer that increases cardiac contractility and is used as a treatment for patients with severe heart failure (Sorsa 2001). Using heteronuclear NMR ad small angle x-ray scattering, Sora *et. al.* showed that levosimendan is capable of binding to both domains of TnC. They also used

NMR chemical shift mapping to show how Levosimendan binds cTnC in the presence of two cTnI peptides, $cTnI_{32-79}$ and $cTnI_{128-180}$, which corresponds to the N-terminus and the inhibitory-switch regions of cTnI, respectively (Sorsa 2003). In the C-terminal domain cTnC, there are no significant levosimendan-induced chemical shift changes, suggesting that the two levosimendan binding sites are blocked by the cTnI peptides. In the N-terminal domain, levosimendan-induced amide chemical shift changes were detected throughout this region, indicating that the N-terminal domain alters its conformation between the “closed” state and the “open” state upon levosimendan binding.

Since levosimendan is a pyridazinone derivative, Levijioki *et. al*. analyzed a group of levosimendan analogs (figure 1-16) and showed that both hydrogen donor and hydrogen acceptors on the pyridazinone ring or on the mesoxalonitrile hydrozone moieties are important for the Ca^{2+} saturated N-cTnC (Levijoki 2000). Furthermore, Robertson *et. al.* used 2D HSQC NMR spectroscopy to investigate several important features of levosimendan and its analogs to cTnC binding (Robertson 2008). First, only those analogs that contain a chiral methyl group induce chemical shift changes, suggesting that this group may be essential for the drug’s biological activity. Second, the hydrophobic pyridazinone rings form a favourable hydrophobic interaction with the center of the hydrophobic binding pocket formed by helix A and helix B. Third, the mesoxalontitrile hydrazone moieties of levosimendan interact with the N-terminus of the cTnI peptide, stabilizing its binding to Ca^{2+} ·N-cTnC. Therefore, they proposed that levosimendan has an overall stabilizing effect on the open conformation of

Ca^{2+} ·N-cTnC, conferring its Ca^{2+}-sensitizing property for the drug. However, the precise molecular details of levosimendan to cTnC are still not known because no high resolution data has been available.

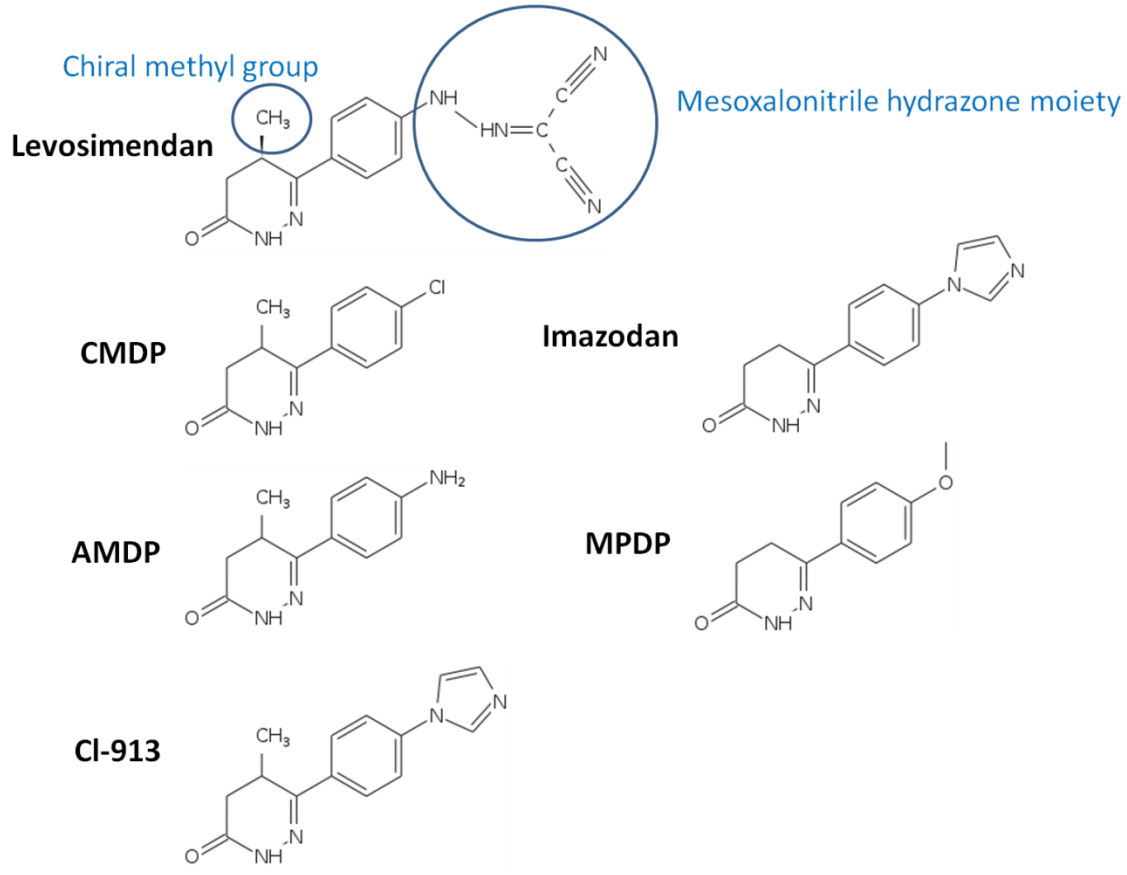

Figure 1-16: Levosimendan and analogs. Figures were generated using GChemPaint (Brefort 2001) and adapted from Li, 2008, Bicohm. Biophys. Res. Commun. (Li 2008) .

1.6.5 **EMD 57033**

EMD 57033 is a thiadiazinone derivative that has been shown to increases Ca^{2+} sensitivity in muscle fibres (Lues 1993; Solaro 1993). It was

shown that EMD 57033 binds to the C-terminal domain of TnC rather than the regulatory N-terminal domain (Pan 1996). The interaction of EMD 57033 with TnC is different from the aforementioned Ca^{2+} sensitizers. Figure 1-17 shows the difference in the NMR structure of Ca^{2+}-saturated C-terminal domain of TnC (Ca^{2+}·C-cTnC) with EMD 57033 (PDB: 1HIO) (Wang 2001). In this structure, EMD 57033 fits deeply inside the hydrophobic cavity (figure 1-17 (b)). The methyl group attached to the chiral carbon of EMD 57033 has hydrophobic interaction with I112, L117, and I148 of the β-sheet between the two Ca^{2+} binding site, strengthening the overall fit of EMD 57033 in the hydrophobic cavity.

(a)

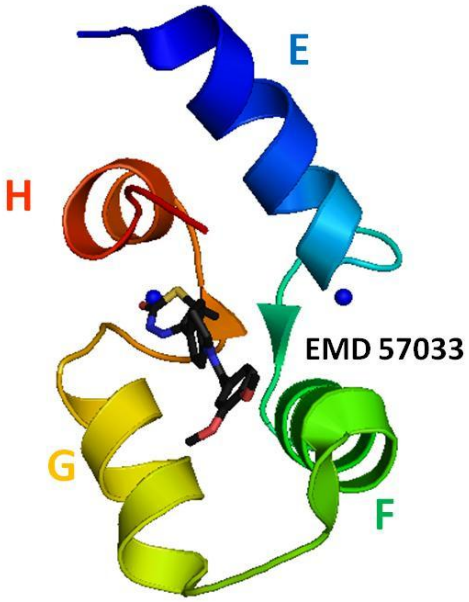

(b)

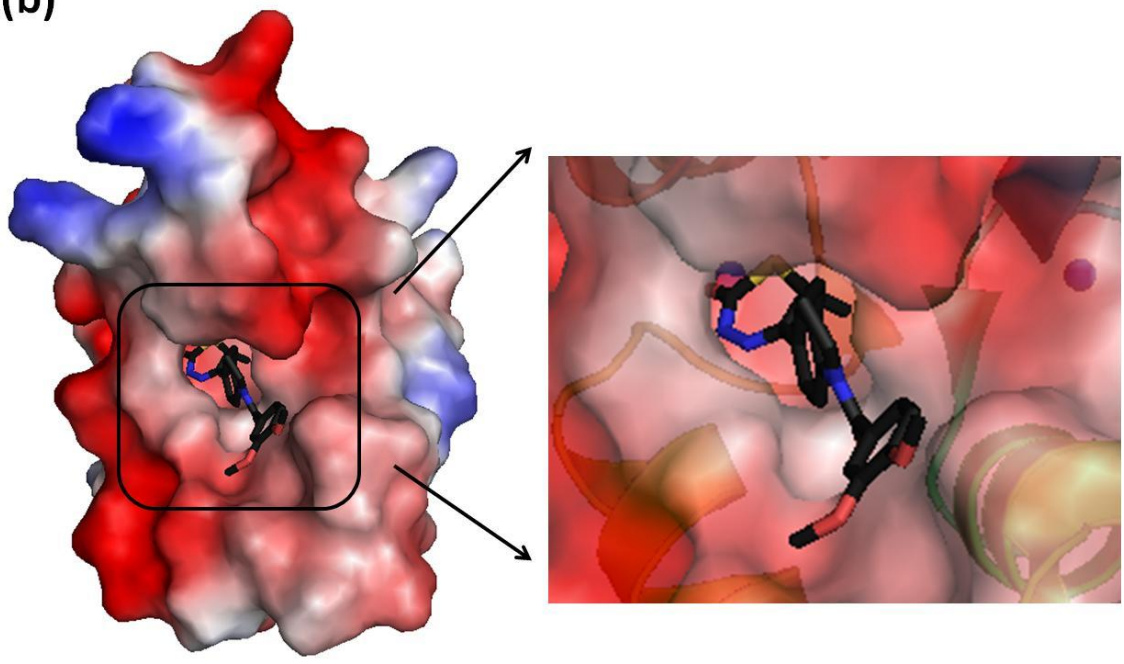

Figure 1-17: (a) The cartoon representation of the NMR structure of $2Ca^{2+}$·C-cTnC·EMD57033. (PDB: 1HIO) (b) the surface representation and

(a) Cartoon rendering coloured spectrally from the N-terminus (red) to the C-terminus (red). The Ca^{2+} ion is shown in a blue sphere. EMD57033 is colored black. (b) The surface representation of $2Ca^{2+}$-cCTnC-EMD57033. The EMD 57033 binding is enlarged as shown. The figures were generated using PyMol (DeLano 2002).

1.6.6 **Anapoe**

Anapoe is not a drug that binds to TnC. It was used as a detergent to optimize the crystal quality of the skeletal troponin complex (figure 1-18(a)) (Vinogradova 2005). Three anapoe molecules bind to the skeletal troponin complex, with one anapoe molecule making specific interactions with the N-terminal domain of sTnC and the switch segment of sTnI (figure 1-18(b)). The hydrophobic head group of anapoe fits into the Met-rich environment of the hydrophobic binding pocket formed by sTnC (figure 1-18 (c)), interacting with the hydrophobic side chains of the switch segment of sTnI (Met121, Leu122, and Leu125). The polar head of anapoe is located on the surface, interacting with the polar solvent environment. A crystal of the skeletal troponin complex formed with and without anapoe, but the diffraction without anapoe was poor. The other two anapoe molecules bind on the surface of TnI and TnT2 helices far from the regulatory domain of TnC, and they make fewer and weaker hydrophobic interactions at theses sites. In addition, the presence of anapoe does not change the unit cell dimensions of the crystal, and the structure is consistent with that determined by small angle neutron and x-ray scattering data (King 2005). Therefore, the authors suggest that anapoe is likely to stabilize the troponin complex in a Ca^{2+}-bound form (Vinogradova 2005). Anapoe also increases the

contractile force of cardiac muscle fibres, suggesting that this compound also binds to cTnC and affect its Ca^{2+} sensitivity (Vinogradova 2005).

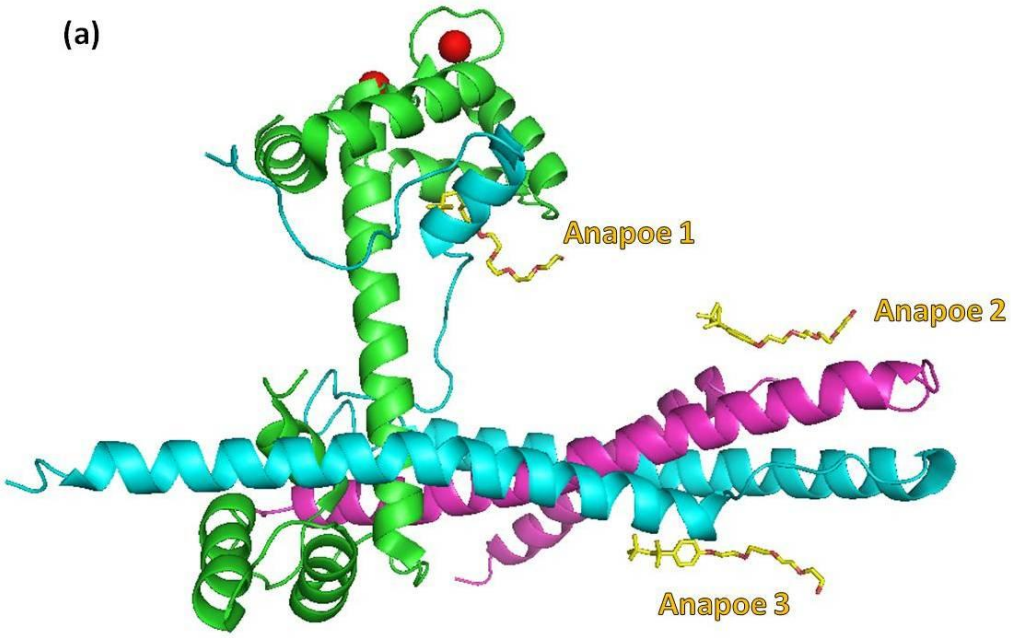

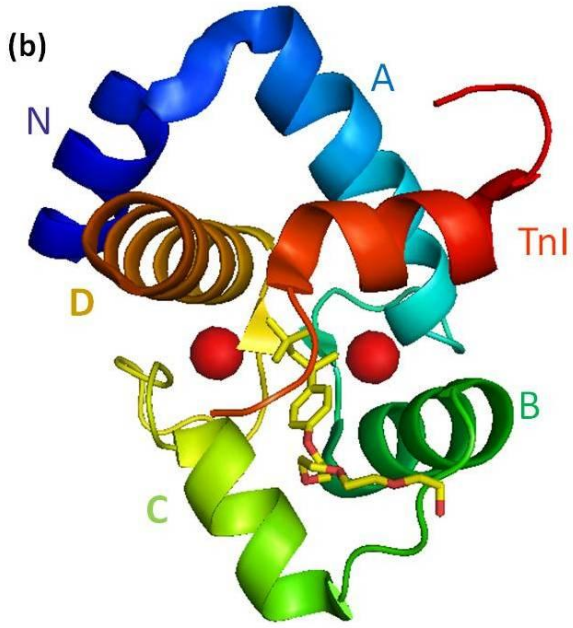

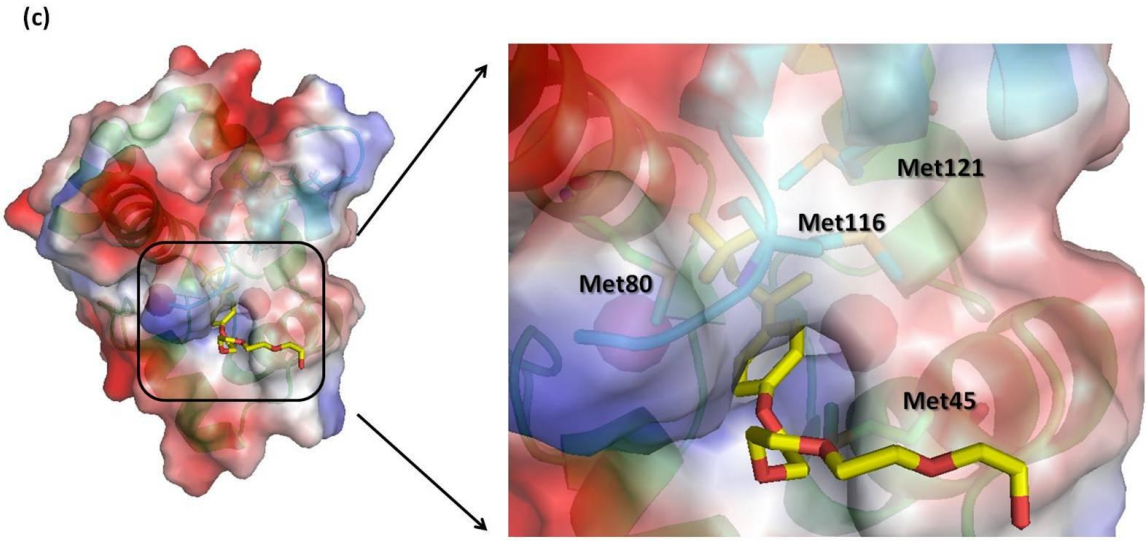

Figure 1-18: Crystal structure of the sTnC complex with Anapoe. (PDB: 1YTZ)

(a) The cartoon representation of the structure. The three anapoe molecules are labelled in yellow. sTnC is coloured in green, sTnI is coloured in cyan, and sTnT is coloured in purple. The Ca^{2+} ions are colored as red spheres. (b) The cartoon rendering coloured spectrally from the N-terminus (blue) to the C-terminus (red) with the amino and carboxyl termini and helices labelled. The switch segment of sTnI is colored red. Anapoe molecule is coloured yellow. (c) The surface representation of (b) with a cartoon structure underneath. The Anapoe binding cavity is enlarged to show the Met-rich environment for the hydrophobic head group of anapoe to bind. The figure was generated using PyMol (DeLano 2002).

1.6.7 Troponin complex

After more than 10 years of crystallization trials, Takeda *et. al.* solved the structure of the core domain of the human troponin complex in the Ca^{2+}-saturated state by X-ray crystallography (Takeda 2003). The core domain was reconstituted from *Escherichia coli*-expressed recombinant human cardiac troponin subunits. One construct has an overall mass of 46K, consisting of full length TnC (1-161), truncated TnI (31-163), and truncated TnT (183-288); the other construct has a mass of 52K, consisting of full length TnC (1-161), TnI (31-210), and TnT (183-288). Crystallization of the complete complex was

unsuccessful, probably due to the flexible, extended binding site of TnT to tropomyosin (Flicker 1982; White 1987). Truncation of TnI and TnT were needed in order to improve the quality of crystallization. Since there are two molecules in the asymmetric unit in each crystal structure of the 46K and 52K construct, there are a total of four molecular structures, namely as Tn46KA, Tn46KB, Tn52KA, and Tn52KB.

From the structure of troponin complex, the core domain is made of primarily alpha helices (figure 1-19). The full-length structure of TnC is observed except the flexible D/E linker region. The two helices H1 and H2 of TnT, and the four helices H1, H2, H3, and H4 of TnI are also shown. The structure of the core domain can be further divided into two sub-domains: the IT-arm domain, which consists of TnC residues 93-161, TnI residues 42-136, and TnT residues 203-271, and the regulatory head domain, which consists of TnC residues 3-84,and TnI residues 150-159.

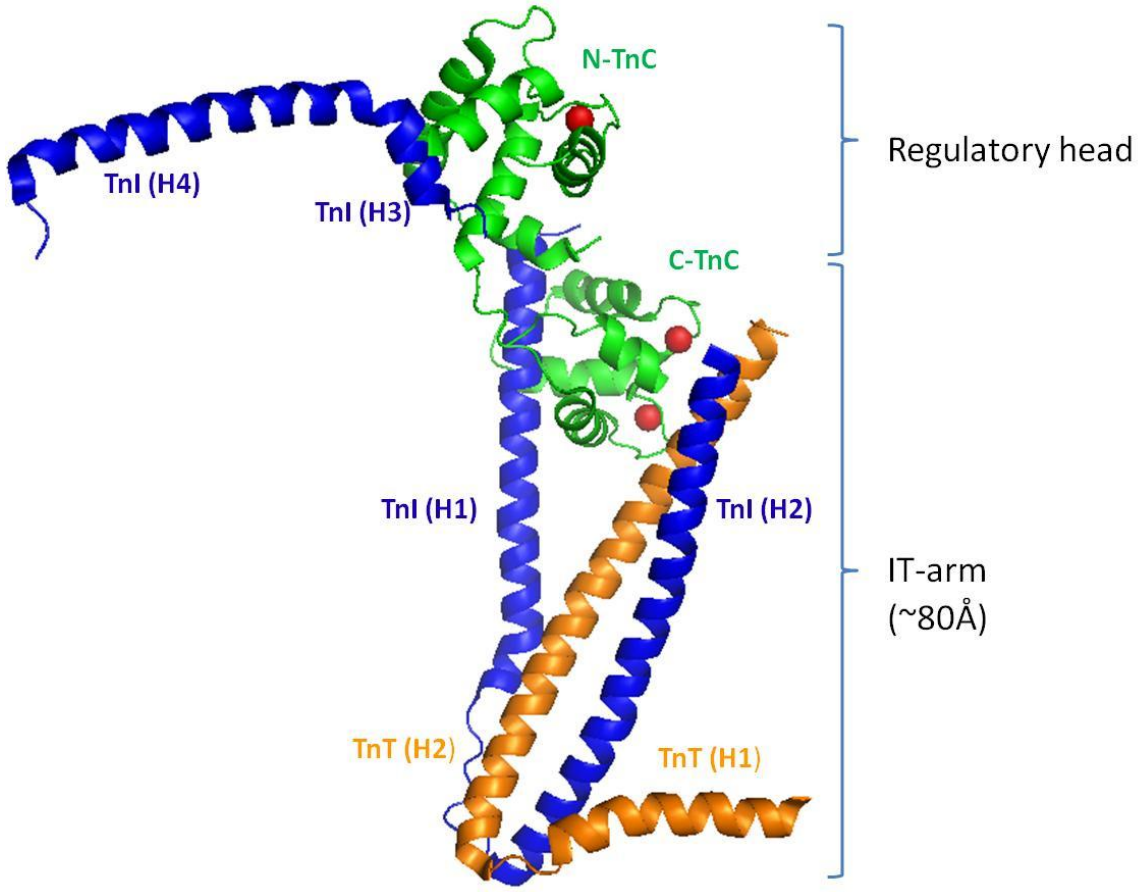

Figure 1-19: Crystal structure of the 52kDa domain of human cardiac troponin in the Ca^{2+} saturated form.

TnC is coloured in green; TnI is coloured in blue; TnT is coloured in orange; the three Ca^{2+} ions that bound to TnC are represented as a red sphere. The regulatory head region includes N-TnC, helix 3 and helix 4 of TnI. The IT-arm region includes C-TnC, helix 1 and helix 2 of cTnT, and helix 1 and helix 2 of cTnI (PDB: 1J1E). The figure is generated using PyMol (DeLana 2002).

Although the main core of the troponin complex is observed in the crystal structure, the electron density map of several other domains of the troponin molecule are not well defined. These domains include the inhibitory region (IR) of TnI, the C-terminal domain of TnI, and both N- and C-terminal domains of TnT

that have potential interactions with actin filaments. The overall B-factors for all four molecules are very high (the averaged B-factors are 73.0 $Å^2$ for Tn46K and 91.7 $Å^2$ for Tn52K). This is probably due to the extremely high flexibility of the molecules, a characteristic of a troponin complex that makes its crystallization very difficult. This extreme flexibility can also be observed by superimposing the structure of all four troponin molecules together, with the superposition of either the IT-arm (figure 1-20 (a)) or the regulatory head region (figure 1-20 (b)). With all four IT arm regions superimposed, the overall displacement of the regulatory head shows only a minor variance. However, when all the regulatory head regions are superimposed, a large displacement of the IT-arms is clearly observed among the four molecules. It is rotated by approximately 20° around the regulatory head region; as a result, this rotation brings about 30Å displacement at the end portion of the IT-arm, showing the unusual flexibility of the entire troponin molecule.

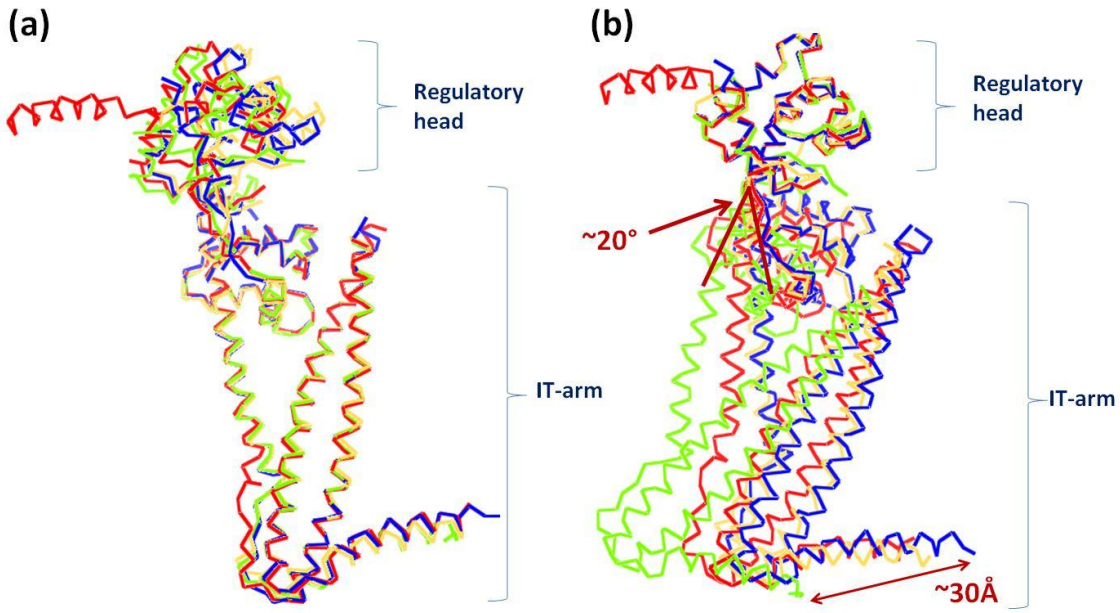

Figure 1-20: Structure comparison of the two molecules in the asymmetric unit of Tn46K (Tn46KA, green; Tn46KB blue) and the two molecules in the asymmetric unit of Tn52K (Tn52KA, red; Tn52KB, orange).

(a) Shows the large structural difference of the regulatory head region when the IT arm are superimposed. (b) The large structural difference of the IT arm region when the regulatory head regions are superimposed. One end of IT arm displays a 20 Å difference among all four models and the other end of IT arm displays a 30 Å difference. This figure is generated using PyMol (DeLana 2002).

The IT-arm is a large, elongated, and rigid domain that is composed of helix 1 (H1) and helix 2 (H2) of TnT, helix 1 (H1) and helix 2 (H2) helices of TnI, and the C-terminal domain of TnC. The helices from TnT and TnI form an overall shape that resembles a “W”, and it is stabilized by two interactions between the subunits. First, H2 of TnT and H2 of TnI form a parallel α-helical coiled-coil formation that is composed of heptad repeats with hydrophobic residues, which are highly conserved among distant species (Stefancsik 1998). The second hydrophobic stabilizing force involves the interaction between the amphiphilic helix H1 of TnI and the hydrophobic binding cleft of C-terminal domain of troponin C. This IT-arm region serves to anchor the troponin complex to the actin and tropomyosin.

The regulatory head is composed of the N-terminal domain of TnC, the two amphiphilic alpha helix 3 (H3) and helix 4 (H4) of TnI, and the C-terminal domain of TnI which is not shown in the current crystal structure. H3 of TnI is located between the inhibitory region of TnI and H4, and binds to actin-tropomyosin complex in the absence of Ca^{2+}. It acts as an important molecular switch to the whole troponin complex. Based on the previously solved NMR

structure of human N-TnC with fragment of TnI (H3) (Li 1999) and the skeletal TnC in complex with N-terminal domain of TnI (Vassylyev 1998), it has been suggested that H3 of TnI binds specifically to the highly conserved hydrophobic region of N-TnC in a Ca^{2+}-bound state. Combining the previous results and the crystal structure of the core domain, Takeda *et. al*. proposed the molecular mechanism of the troponin complex during Ca^{2+} regulation (figure 1-21). In the absence of Ca^{2+}, the troponin complex resides on the actin-tropomyosin complex, with the inhibitory region (IR) of TnI bound to an actin monomer. When Ca^{2+} is bound to site II of N-TnC, it exposes the hydrophobic site for H3 of TnI to bind. After binding to the hydrophobic site of N-TnC, TnI releases its inhibitory region on the actin-tropomyosin complex. The disposition of H4 of TnI and the C-terminal domain also changes dramatically as the mobile regulatory region of TnI detaches itself from the actin-tropomyosin complex (Geeves 2000).

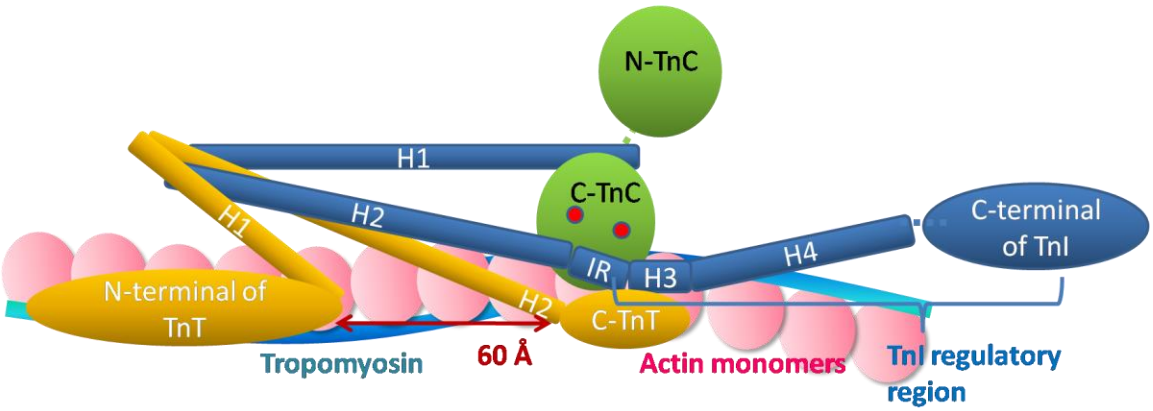

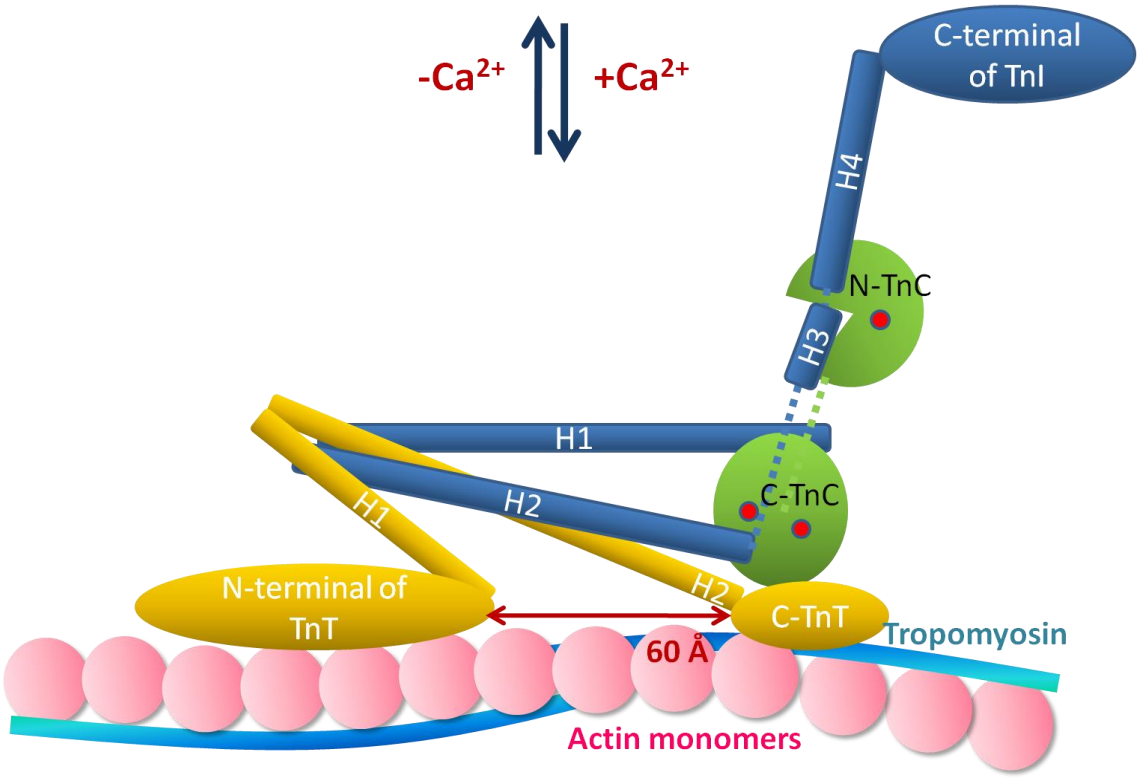

Figure 1-21: A schematic representation of the conformation of cardiac troponin in relation to thin filament in the absence and presence of Ca^{2+}.

This schematic representation is drawn based on the crystal structure of the core domain of the human troponin complex IR is the inhibitory region of TnI; it is not observed in the crystal structure. Both the N-terminal and C-terminal domain of TnT are also not observed in the crystal structures. The red dots represent Ca^{2+} ions. The figure is adapted from Takeda, 2003, Nature (Takeda 2003).

1.7 Overview of Objectives

This project is in collaboration with Dr. Glen Tibbits' group in Biomedical Physiology and Kinesiology department at Simon Fraser University. While they perform the *in situ* studies using cTnC mutants and *in vitro* kinetic studies on

cTnC proteins, we perform the structural analysis using X-ray protein crystallography. Since the N-terminal domain of cTnC serves an essential function as the Ca^{2+} sensor to initiate the cascade event of muscle contraction, understanding the structure of N-cTnC can provide valuable information on cTnC. To date, all native N-cTnC structures are solved by NMR spectroscopy. To understand the structural difference between the wild type N-cTnC and mutant L29Q and NIQD N-cTnC, obtaining the crystal structure of these proteins are essential. Therefore, the specific goals in this project are:

1) Crystallizing the human wild type N-cTnC, mutant L29Q N-cTnC, and mutant NIQD N-cTnC.
2) Collecting the X-ray diffraction data of the wild type N-cTnC and mutant N-cTnC crystals using the *SFU Macromolecular X-rays Diffraction Data Collection Facility* and *Synchrotron Radiation.*
3) Processing the X-ray diffraction data, solving, and refining the structures.
4) Analyzing the structure and comparing to the previously-solved cTnC homologous structures.

Ultimately, the structural changes of the mutant N-cTnCs will provide a significant insight into the etiology of familial hypertrophic cardiomyopathy, and give invaluable information on the rational drug design of novel Ca^{2+}-sensitizing drugs. In this project, I have solved the structure of the wild type human N-cTnC and successfully identified a new ligand that binds to the regulatory domain of N-cTnC. It is possible that deoxycholic acid may be used as a starting point for the

rational structure based design of drugs for the treatment of troponin-related cardiovascular diseases.

2: CRYSTALLIZATION OF THE AMINO-TERMINAL DOMAIN OF CARDIAC TROPONIN C IN THE TRIGONAL/HEXAGONAL SYSTEM – DEALING WITH TWINNED CRYSTALS

2.1 Introduction

The native full-length WT, L29Q, and NIQD TnC in pET21 constructs were obtained from Dr. Glen Tibbits' group. Site-directed mutagenesis was carried out to generate the truncated versions of each of the cTnC constructs that contain only the regulatory domain of residues 1-89 (N-cTnC). After confirming the constructs were successfully mutated, the three N-cTnC/pET21 constructs were transformed into BL21(DE3) expressing strains for overexpression. All three N-cTnC/pET21 constructs were successfully expressed, purified, and crystallized. The crystals were further optimized, and several datasets with a resolution range from 2.0Å to 3.3 Å were collected. From the initial data processing, the crystals for all three protein constructs were found to belong to the trigonal/hexagonal space group system. Because several homologous structures with high sequence identity are available, molecular replacement method was chosen for solving the crystal structure. It requires a model with highly conserved structure to generate a starting solution (Rossmann 1990). However, attempt to solve their structures by molecular replacement was completely unsuccessful. Two reasons could account for the apparent difficulties in finding a solution. First, the

homologous models used might not have conserved structural conformation despite of their high sequence identity with our N-cTnC constructs. Second, a crystal growth disorder known as “twinning” may have influenced the datasets.

Twinning is a crystal growth anomaly in which a single crystal is composed of two different crystal domains. As a result, each domain produces separate reflections that overlap with one another (Yeates 1999). Depending on the orientation of the two domain lattices, the crystal could have epitaxial twinning or merohedral twinning. Epitaxial twinning occurs when the two crystal lattices overlap less perfectly in three dimensions. Because of this, spots that belong to different lattices do not directly overlap and can be distinguished on the diffraction pattern (figure 2-1 (a)). Thus, the dataset from one crystal lattice can be separated from the other during data processing and can be used successfully for structure determination. On the other hand, merohedral twinning results from the two crystal lattices of different domains coinciding exactly in three dimensions. The reflections from each domain overlap completely so the resulting diffraction pattern appears to be from a single lattice. However, each reflection intensity is a weighed sum of two different intensities.

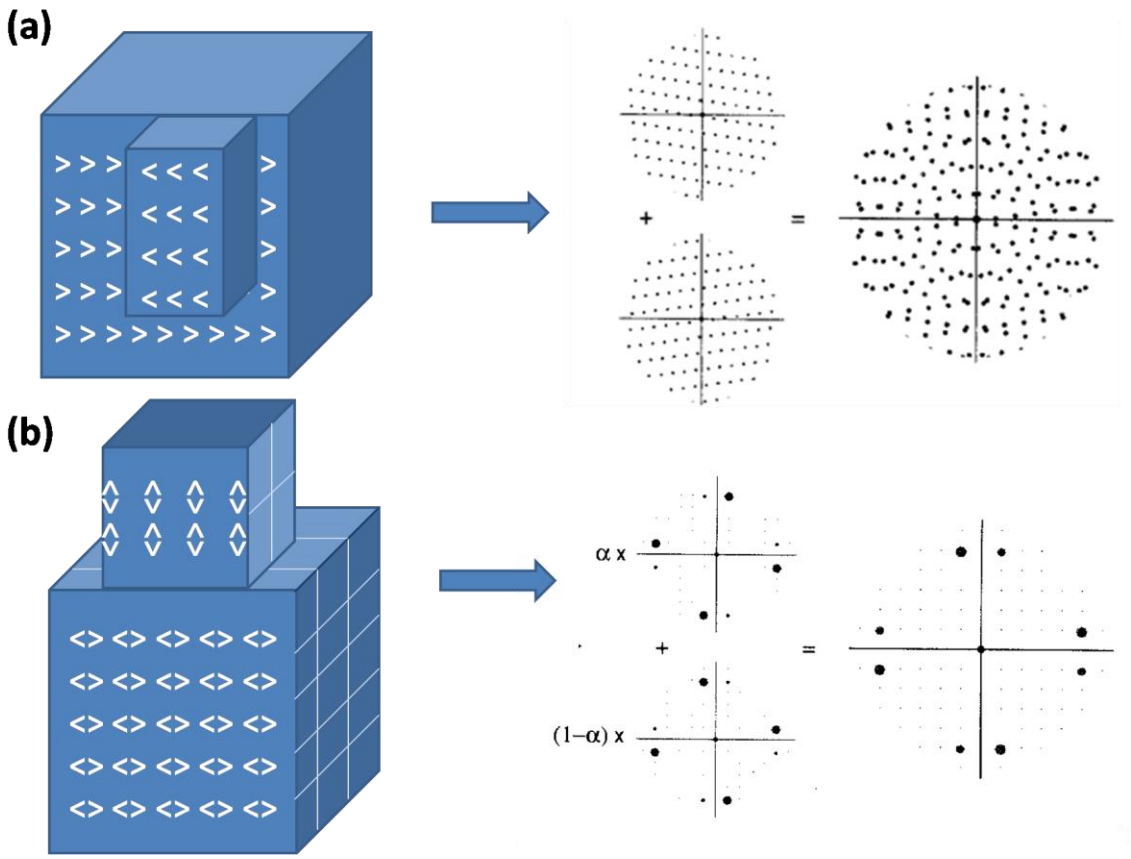

Figure 2-1: They hypothetical models of (a) epitaxial twinning and (b) merohedral twinning. Figure is adpated from Yeats, 1999 (Yeates 1999).

(a) Epitaxial twinning: the two crystal lattices do not overlap in three dimensions so the total diffraction pattern contains interpenetrating lattices. (b) Merohedral twinning: the two crystal lattice superimposed completely in three dimenions so the total diffration pattern appears to be a single lattice. The figure was adapted from Yeats 1999, Structure.

The observed intensity from the twinned crystal is related to the intensities from each of the two domain lattices by the following equation:

$$I_{total} = \alpha I_{hkl} + (1-\alpha) I_{h'k'l'}$$

I_{total} is the total intensity of the twinned crystal, and the twin fraction α represents the fractional volume of the crystal that is occupied by the smaller lattice of the two. The hkl and h'k'l' are reflection indices from different lattices related by a twin operator, which is the symmetry operation that relates the orientations of the two lattices. Depending on the value of α, two possible situations can occur: A) partial twinning when the twin fraction $\alpha < 0.5$, and B) perfect twinning when the twin fraction $\alpha = 0.5$. If partial twinning occurs and α is much less than 0.5, it is possible to 'detwin' the data using available computer programs and proceeds to structure determination. However, if α is large and close to 0.5, then the structure solving becomes difficult because of two factors. Firstly, the symmetry of the twinning operation is imposed on top of the crystallographic symmetry to give an erroneously high symmetry and thus determining the correct crystal space group becomes difficult. Secondly, the true crystallographic intensities of a single crystal domain required for solving the crystal structure cannot be recovered. For these reasons, it is frequently advisable to restart the search for a new crystallization condition that produces twin-free crystals (Yeates 1997). Table 2.1 shows the crystal space groups that allow twinning and the possible twin operators.

The crystallographic program DETWIN (Rees 1980; Yeates 1999) from CCP4 program suite uses the following equation to estimate the twinning fraction.

$$H = |I_{hkl} - I_{h'k'l'}| \; / \; |I_{hkl} + I_{h'k'l'}|$$

where I_{hkl} and $I_{h'k'l'}$ are the observed intensities of two reflections related by the twin operator. H is a function of the twinning fraction α and the two true crystallographic intensities. When the twinning fraction gets larger, both intensities become more similar therefore the absolute value of H becomes smaller. Since untwined reflection intensities follow normal distribution, it is possible to calculate the expected distribution for H as a function of α. DETWIN calculates the cumulative distribution of H in the twinned dataset and compares it against the expected cumulative distributions at different values of α. This comparison provides the estimate of the twinning fraction in the crystal (figure 2-2).

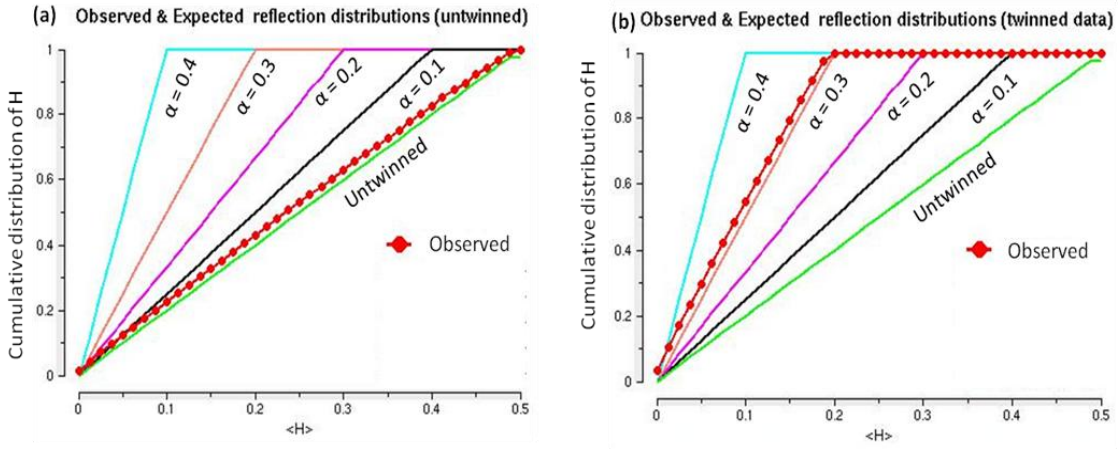

Figure 2-2: The H twinning test carried out by DETWIN.

The y-axis the cumulative distribution of H, and x-axis is the calculated value of H. The red line with the dots represent the experimental value. Green line represents α of 0.0, black line represents α of 0.1, pink line represents α of 0.2, orange line represents α of 0.3, and cyan line represents α of 0.4. The smaller the <H>, the higher α since α = 0.5 - <H>. The figure is from CCP4 twinning notes website.

The DETWIN program also produces Britton plot which display the number of negative intensities after detwinning as a function of the twin fraction α, which produces more accurate estimation of the twin fraction. Figure 2-3 shows examples of Britton plot for untwinned and twinned data.

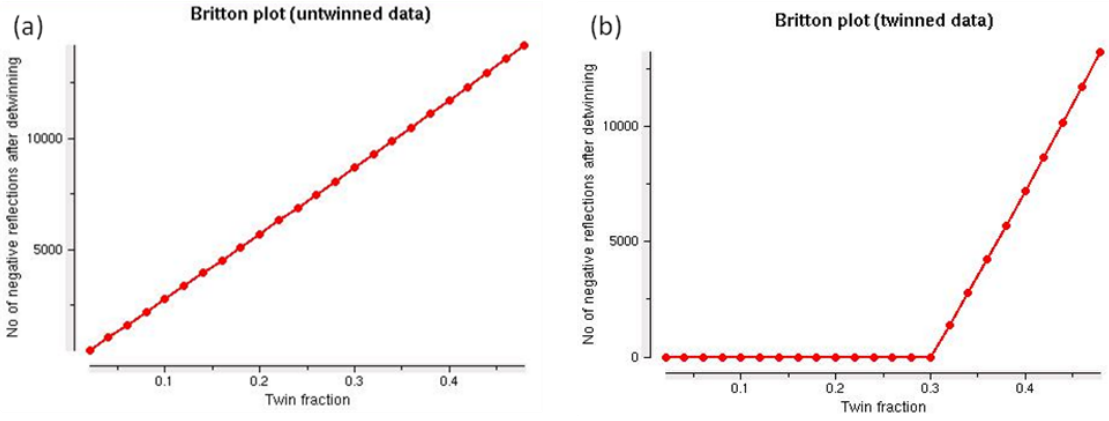

Figure 2-3: The example of Britton plot for (a) untwinned data and (b) twinned data. The figure is from CCP4 twinning notes website.

Table 2-1: The possible merohedral twin operators for tetragonal, trigonal, hexagonal, and cubic space group system (Chandra 1999).

space group number	space group	point group	possible twin operator
Tetragonal space group system – perfect twin appears as P422			
75	P4	PG4	k,h,-l
76	P41	PG4	k,h,-l
77	P42	PG4	k,h,-l
78	P43	PG4	k,h,-l
79	I4	PG4	k,h,-l
80	I41	PG4	k,h,-l
Trigonal space group system – perfect twin appears as P622			
143	P3	PG3	-h,-k,l; k,h,-l; -k,-h,-l
144	P31	PG3	-h,-k,l; k,h,-l; -k,-h,-l
145	P32	PG3	-h,-k,l; k,h,-l; -k,-h,-l
146	H3	PG3	k,h,-l
149	P312	PG312	-h,-k,l or k,h,-l
151	P3112	PG312	-h,-k,l or k,h,-l
153	P3212	PG312	-h,-k,l or k,h,-l

150	P321	PG321	-h,-k,l or -k,-h,-l
152	P3121	PG321	-h,-k,l or -k,-h,-l
154	P3221	PG321	-h,-k,l or -k,-h,-l
Hexagonal space group system – perfect twin appears as P622			
168	P6	PG6	k,h,-l
169	P61	PG6	k,h,-l
170	P65	PG6	k,h,-l
171	P62	PG6	k,h,-l
172	P64	PG6	k,h,-l
173	P63	PG6	k,h,-l
Cubic space group system – perfect twin appears as P43			
195	P23	PG23	k,h,-l
196	F23	PG23	k,h,-l
197	I23	PG23	k,h,-l
198	P213	PG23	k,h,-l
199	I213	PG23	k,h,-l

2.2 Materials and Methods

2.2.1 Mutagenesis of full-length troponin constructs

Full length WT TnC (WT TnC), mutant L29Q TnC and NIQD TnC (residue 1-161) in the pET21 vector were obtained. In order to truncate the construct to just the regulatory domain (residue 1-89) of troponin C, residue 90 (lysine) was converted to a termination codon using site-directed mutagenesis. Before carrying out site-directed mutagenesis, the plasmid constructs were purified from *E. coli* DH5α cloning strain. Site-directed mutagenesis was carried out using the Quick Change kit (Stratagene) with 39-base forward primer 5'-TGTATGAAAGATGACAGCTAAGGAAAATCTGAAGAGGAG-3' and a reversed primer 5'-CTCCTCTTCAGATTTTCCTTAGCTGTCATCTTTCATACA – 3'. The entire cTnC gene was sequenced to confirm the mutation.

2.2.2 **Overexpression of the native N-cTnC protein**

A small-scale protein expression test was carried out to confirm the expression of N-cTnC proteins. The N-cTnC/pET 21 constructs were transformed into BL21(DE3) expression host strains. A single colony was picked from a fresh plate containing BL21(DE3) transformants and was grown with shaking at 250 rpm in 5mL of LB containing 100μg/mL ampicillin at 37°C for 4 hours and was induced with a final concentration of 1mM IPTG at 37°C for an additional 4 hours. The protein expression was visualized by SDS-PAGE with a 15% acrylamide gel (Sambrook 1989) .

For large-scale protein expression, a fresh LB agar/ampicillin plate was streaked with N-cTnC/pET21/BL21(DE3) cells and incubated at 37°C overnight. A single colony was picked from the plate and was grown in 100mL of LB media with 100ug/mL of ampicillin at 30°C overnight. The next day, each litre of LB culture was inoculated with 10mL of overnight cell culture and allowed to grow at 37°C for 4 hours with shaking at 250 rpm until the OD^{600} reached to 0.8. The cells were the induced with a final concentration of 1mM IPTG and allowed to grow for additional 4 hours. After the induction, cells were harvested by centrifugation at 5000 rpm for 15 mins and stored at -80°C.

2.2.3 **Native N-cTnC purification by column chromatography**

The purification procedure was adapted from Xu *et. al*'s purification of full-length avian troponin C with some modification (Xu 1988). A similar purification procedure was used in purifying chicken N-sTnC (Strynadka 1997).

Cell pellets were thawed and resuspended in 30 mL of resuspension buffer (50 mM Tris-HCl pH 7.5, 25% sucrose, 0.5mM PMSF), with 1 tablet of complete protease inhibitor (Roche) and 50µl of 1M $MgCl_2$. The cell solution was properly mixed with the resuspension buffer for 30 minutes at 4°C. the cell pellet was collected by centrifugation at 15,000rpm (Beckman JLA10.5) for 30 mins at 4°C to harvest N-TnC proteins in the supernatant. 1mM $MgCl_2$, 5mM $CaCl_2$, 50mM NaCl, and 1mM DTT were added to the supernatant before purification.

The first purification was carried out using a phenyl-sepharose fast flow hydrophobic interaction column at room temperature (GE Health Care). Five millilitre of the beads were equilibrated with the equilibration buffer (50 mM Tris-HCl pH 7.5, 5 mM $CaCl_2$, 1 mM $MgCl_2$, 50 mM NaCl, and 1 mM DTT). Ten mL of N-TnC supernatant was loaded onto the phenyl sepharose column and washed with 10 mL of equilibration buffer. The column was washed with high salt buffer (1M NaCl, 50mM Tris-HCl pH 7.5, 0.1mM $CaCl_2$, and 1mM DTT). Finally N-cTnC was eluted using elution buffer (50 mM Tris-HCl pH 7.5, 1 mM EDTA, and 1 mM DTT). The elution fractions containing N-cTnC were visualized by 15% SDS-PAGE gel. They were combined and further purified using an AktaPrime instrument with a HiTrap 26/60 Sepharacryl S-100 size exclusion column (GE Health Care). The column was previously equilibrated with a buffer containing 50 mM Tris-HCl pH 7.5, 0.2 mM $CaCl_2$, and 1 mM DTT. The fractions containing purified N-cTnC were pooled together, concentrated to between 10 and 20 mg/mL, and stored at -80°C. The purity of the protein was confirmed by 15% SDS-PAGE.

2.2.4 **Crystallization of native N-cTnC protein**

All initial crystallization trials were set up using the sitting-drop vapour diffusion method at room temperature. The 24 well sitting drop plate (Hampton Research) was used. Crystal Screen I (50 reagents, Hampton Research), crystal screen II (48 reagents, Hampton Research), Peg/Ion screen (48 reagents) were used to screen for crystallization conditions. Each crystallization drop was prepared by mixing 1μL of purified protein solution (10 to 20 mg/mL) with 1μL of reservoir solution and then equilibrating the drop against 1mL of reservoir solution.

2.2.5 **Data collection for WT N-cTnC**

Prior to data collection, crystals were transferred to a cryoprotectant solution which consisted of the original crystallization solution with 30% of the water replaced with glycerol. The optimized WT N-cTnC crystal was collected at the Macromolecular X-ray Diffraction Data Collection Facility at Simon Fraser University. It uses a MicroMax-007 rotating-anode microfocus generator which operates at 40mV and 20mA, VariMax Cu HF optics, an R-AXIS IV++ image-plate area detector (MSC-Rigaku), and an X-stream 2000 cryosystem. The crystal-to-detector distance was 200mm with 1º oscillation angle. 360 images were collected and the spots were visible up to 2.4Å.

2.2.6 **Data collection for L29Q N-cTnC**

The optimized L29Q N-cTnC crystal was collected at the Macromolecular X-ray Diffraction Data Collection Facility at Simon Fraser University. It uses a

MicroMax-007 rotating-anode microfocus generator which operates at 40mV and 20mA, VariMax Cu HF optics, an R-AXIS IV++ image-plate area detector (MSC-Rigaku), and an X-stream 2000 cryosystem. The crystal-to-detector distance was 120mm with 1º oscillation angle. 360 images were collected and the spots were visible up to 1.8 Å.

2.2.7 **Data collection for NIQD N-cTnC**

Diffraction data for mutant NIQD N-TnC crystal was collected at beamline Ray2 at the Macromolecular X-ray Data Collection Facility at University of British Columbia. The crystal-to-detector distance was 250mm with 1º oscillation angle. 180 images were collected and spots were visible up to 3.0 Å.

2.2.8 **Data processing**

The datasets from WT N-cTnC, L29Q N-cTnC, and NIQD N-cTnC were processed by the HKL2000 software package (Otwinowski 1997). Molecular replacement was carried out using MOLREP(Vagin 1997), PHASER (McCoy 2007), and MRBUMP (Keegan 2007). Twinning analysis was performed using DETWIN (Rees 1980; Yeates 1999) and TRUNCATE (French 1978). Homology models were built from web servers such as CaspR (Claude 2004), Phyre (Bennett-Lovsey 2008), and CHAINSAW (Stein 2008).

2.3 Results and Discussion

2.3.1 Mutagenesis of full-length troponin constructs

The mutagenesis was successful for all three N-TnC constructs. Lysine 90 was converted to a stop codon and the whole sequence was confirmed by DNA sequencing (figure 2-4).

```
WT N-TnC                MDDIYKAAVEQLTEEQKNEFKAAFDIFVLGAEDGCISTKELGKVMRMLGQ 50
Full length WT TnC      MDDIYKAAVEQLTEEQKNEFKAAFDIFVLGAEDGCISTKELGKVMRMLGQ 50
                        **************************************************

WT N-TnC                NPTPEELQEMIDEVDEDGSGTVDFDEFLVMMVRCMKDDS-GKSEEELSDL 99
Full length WT TnC      NPTPEELQEMIDEVDEDGSGTVDFDEFLVMMVRCMKDDSKGKSEEELSDL 100
                        ************************************* ***********

WT N-TnC                FRMFDKNADGYIDLEELKIMLQATGETITEDDIEELMKDGDKNNDGRIDY 149
Full length WT TnC      FRMFDKNADGYIDLEELKIMLQATGETITEDDIEELMKDGDKNNDGRIDY 150
                        **************************************************

WT N-TnC                DEFLEFMKGVE 160
Full length WT TnC      DEFLEFMKGVE 161
                        ***********


L29Q N-TnC              MDDIYKAAVEQLTEEQKNEFKAAFDIFVQGAEDGCISTKELGKVMRMLGQ 50
Full length WT TnC      MDDIYKAAVEQLTEEQKNEFKAAFDIFVLGAEDGCISTKELGKVMRMLGQ 50
                        ***************************** ********************

L29Q N-TnC              NPTPEELQEMIDEVDEDGSGTVDFDEFLVMMVRCMKDDS-GKSEEELSDL 99
Full length WT TnC      NPTPEELQEMIDEVDEDGSGTVDFDEFLVMMVRCMKDDSKGKSEEELSDL 100
                        ************************************* ***********

L29Q N-TnC              FRMFDKNADGYIDLEELKIMLQATGETITEDDIEELMKDGDKNNDGRIDY 149
Full length WT TnC      FRMFDKNADGYIDLEELKIMLQATGETITEDDIEELMKDGDKNNDGRIDY 150
                        **************************************************

L29Q N-TnC              DEFLEFMKGVE 160
Full length WT TnC      DEFLEFMKGVE 161
                        ***********
```

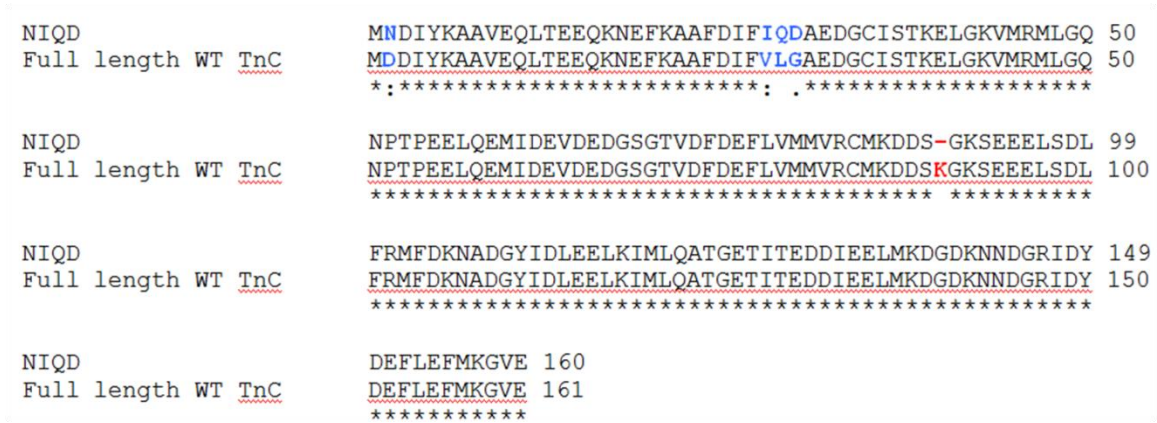

Figure 2-4: Sequence alignment between N-TnC and full length WT bovine TnC (Swiss-Prot accession number P63315) to confirm the site-directed mutagenesis.

Lysine at position 90 (shown in red) for all three TnC constructs was successfully mutated to a stop codon, which is represented by a red dash. The difference between WT N-TnC and mutant N-TnC are shown in blue. The sequence alignment is generated using ClustalW 2.0.10 (Thompson 2002).

2.3.2 Over-expression and purification of native N-TnC proteins

The small-scale protein expression for N-TnC proteins was successful, and N-TnC proteins migrated as a 10kDa species on a 15% SDS-PAGE gel (figure 2-5).

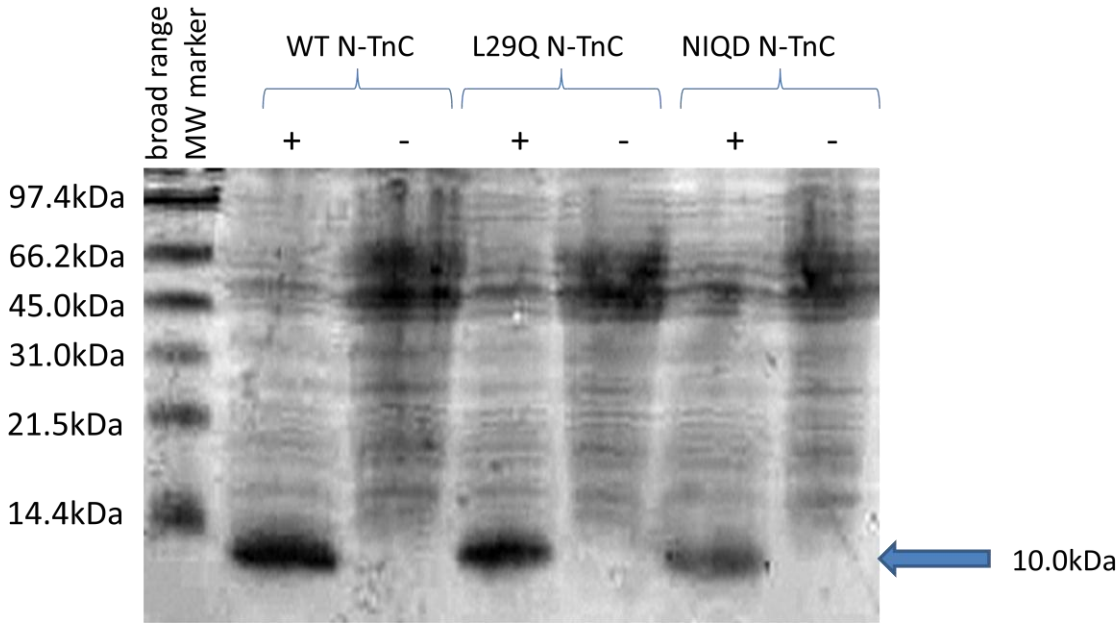

Figure 2-5: A small scale protein expression for N-TnC/pET21/BL21(DE3).

The lanes indicated by (+) present cells induced with 1mM IPTG; the lanes indicated by (-) present cells without IPTG induction. This is a 15% SDS-PAGE gel stained with Coomassie Blue dye.

After centrifuging the cell lysate using JA17 rotor at 14,500 rpm for 30 minutes, N-cTnC was found in the soluble fraction. The cell lysate was then incubated with $CaCl_2$ for 30 min to ensure that all of the N-cTnC proteins were bound by Ca^{2+} ions. Upon Ca^{2+} binding, cTnC undergoes a conformational change that exposes its hydrophobic binding site which interacts with the hydrophobic matrix (Tanaka 1984). Most N-cTnC proteins were eluted in the fraction that contained EDTA, but some were found in the washing fraction (figure 2-6). To capture this protein, the wash fractions containing N-cTnC were reloaded on the column. The fraction obtained by hydrophobic interaction column

chromatography were analyzed on a 15% SDS-PAGE gel stained with Page Blue solution.

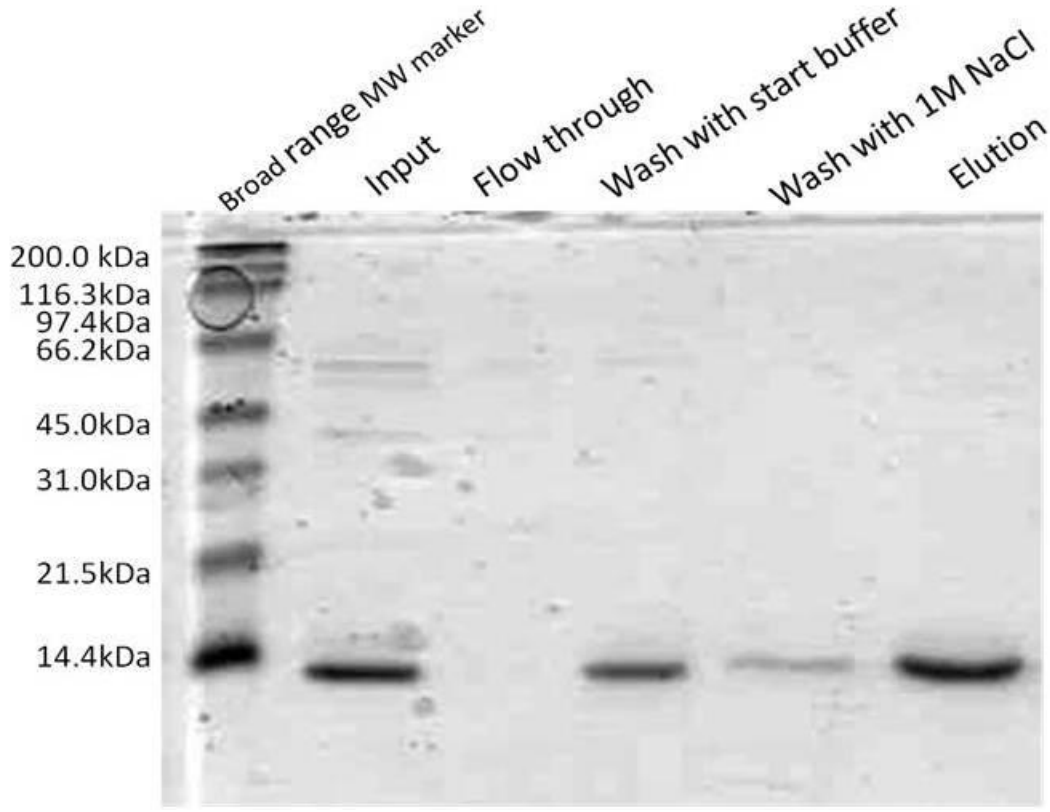

Figure 2-6: Purification of WT N-cTnC proteins by hydrophobic interaction chromatography.

All the fractions collected from hydrophobic interaction column were run at a 15% SDS-PAGE and the gel was stained by Page Blue solution.

All the elution fractions containing N-cTnC were combined and further purified by size-exclusion chromatography. The purified N-cTnC eluted at 140 mL and migrated as a 10kDa species on the gel (figure 2-7). All the fractions containing N-TnC were combined and concentrated to 10 to 20 mg/mL. All three N-cTnC constructs behaved similarly throughout the purification process.

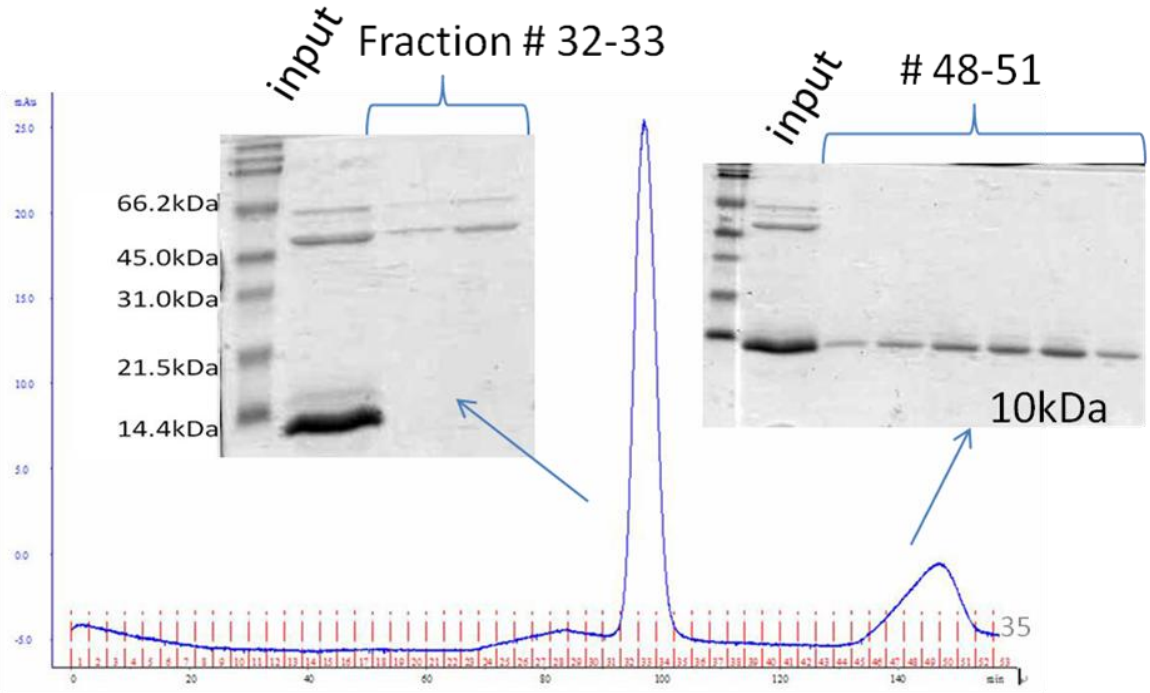

Figure 2-7: Gel filtration chromatogram of WT N-cTnC.

The large peak, eluted at the void volume at 100 mL, represents the proteins of higher molecular weight. The smaller peak, eluted at about 150 mL, represents the 10kDa N-cTnC proteins.

2.3.3 Crystallization of native troponin C

The initial crystallization for the WT N-cTnC protein and the mutant L29Q and NIQD N-cTnC protein were found in condition #34 of Crystal Screen II, which contained 0.05M cadmium sulphate ($CdSO_4$), 1.0M sodium acetate (NaOAc), and 0.1M Hepes pH 7.5. The crystal of WT N-cTnC protein appeared within the first 24 hours at room temperature. The crystals of L29Q mutant and NIQD N-cTnC mutant were small, and a high rate of nucleation was observed. The concentration of NaOAc was varied (0.6-1.2 M) and a range of different pH

buffers from 4.5 to 9.5 were tried. Both mutant proteins tended to crystallize better in a more basic pH range (8.0-9.5) and with a lower concentration of NaOAc (0.5-0.7M). In addition, in order to reduce the nucleation, a lower protein concentration (~10 mg/mL) was used. Additives from the additives screen were added to the crystallization drop. Both L29Q and NIQD N-cTnC mutant formed better crystals that were free of aggregated crystals. L29Q N-cTnC also formed much larger crystals with the addition of 1µl of acyl alcohol in the crystallization drop. The crystallization condition for NIQD N-cTnC protein was 0.05M $CdSO_4$, 0.7 M NaOAc, and 0.1M Hepes pH 7.5 using the hanging-drop method. Figure 2-8 shows the optimized crystals for each protein construct.

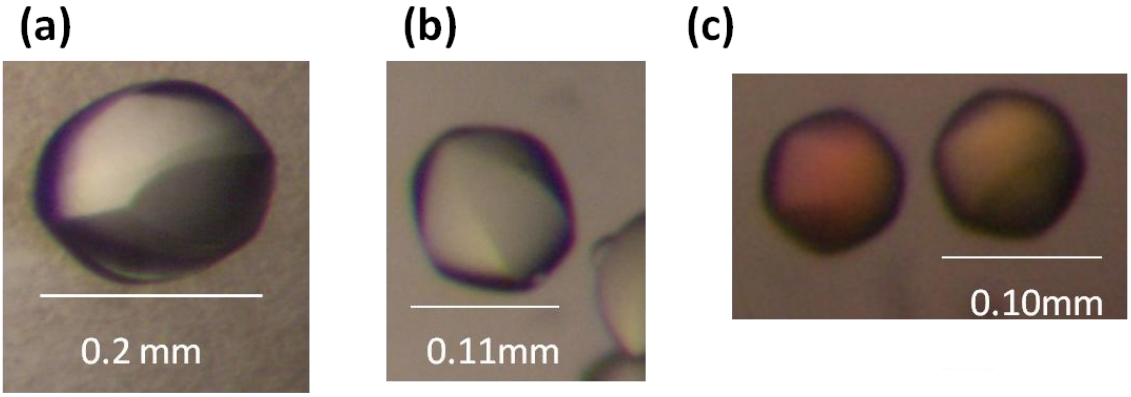

Figure 2-8: The trigonal/hexagonal crystal of (a) WT N-TnC; crystal dimension is approximately of 0.20 mm × 0.15 mm × 0.02 mm. (b) The trigonal/hexagonal crystal of L29Q N-cTnC; crystal dimension is approximately of 0.11 mm × 0.11 mm × 0.02 mm. (c) The trigonal/hexagonal crystal of NIQD N-cTnC; crystal dimension is approximately 0.10 mm × 0.10 mm × 0.02 mm.

2.3.4 **Data processing on the trigonal/hexagonal crystal**

The crystal of WT N-cTnC, L29Q N-cTnC, and NIQD N-cTnC appeared to belong to the hexagonal P622 space group. Each one of them has one molecule per asymmetric unit with a Matthews coefficient of 2.03 (39.6% solvent), 2.07(40.6%), and 2.01(38.8%), respectively. WT N-cTnC diffracted beyond 2.2 Å, while L29Q N-cTnC diffracted beyond 2.0 Å and NIQD N-cTnC diffracted beyond 3.3 Å (Table 2-2).

Table 2-2: Data collection statistics for hexagonal WT N-cTnC, L29Q N-cTnC, and NIQD N-cTnC.

	WT N-cTnC	**L29Q N-cTnC**	**NIQD N-cTnC**
Crystal parameters			
Space group	P622	P622	P622
a, b, c (Å)	45.6 x 45.6 x 115.3	49.7 x 49.7 x 116.9	49.6 x 49.6 x 114.5
α, β, γ (°)	90.0 x 90.0 x 120.0	90.0 x 90.0 x 120.0	90.0 x 90.0 x 120.0
Data collection statistics			
Wavelength	1.54		
Resolution (Å)	2.44-50.0 (2.44-2.53)	2.00-50.0 (2.00-2.07)	3.30-50.0 (3.30-3.41)
Total reflections	67460	42635	27370
Unique reflections	3541	5675	1506
R_{merge}	0.120 (0.308)	0.100 (0.221)	0.163 (0.422)
Mean (I)/σ(I)	17.5 (9.2)	59.4 (43.5)	15.6 (6.8)
Completeness	99.9 (100.0)	90.0 (90.8)	99.9 (98.5)
Redundancy	19.1 (19.3)	7.5 (8.0)	18.2 (19.0)
Mosaicity	0.703	0.683	0.668
% solvent	39.56	40.58	38.81
Matthew coefficient	2.03	2.07	2.01

There are a total of fifty-seven deposited NMR and crystal structures of N-TnC and N-TnC-related molecules in the RCSB PDB protein databank (http://www.rcsb.org). All of them were utilized as search models for molecular

replacement. The crystallographic programs PHASER (McCoy et al., 2007) and MOLREP (Vagin et al., 1997) in the CCP4 program suite were initially used to search for the correct solution. Both full-length models and truncated 'core' domains were used in the search. The truncated domains only contained helix A, helix B, and helix C because the termini and the loop regions of N-TnC appeared very flexible in these structures. While some of the structures had virtually identical sequence with our wild type N-cTnC construct, others were 'modelled' by homology modelling programs such as CHAINSAW (Stein 2008). Approximately fifty homology models were generated and used. However, numerous searches with either the full-length or the core domain did not produce any promising solutions. The program MRBUMP (Keegan et al., 2007) was also used. It is an automated CCP4 program that uses the same molecular replacement programs as the above but automation allows the program to carry out more exhaustive searches with the available N-cTnC structures. For example, it uses all the available chains from the homologous NMR solution structures, which totals over 303 N-cTnC chains of different conformations. The automated searches did not result in a useful solution. The unsuccessful molecular replacement could be due to two possible reasons. Firstly, the overall conformations of the homologous structures might be significantly different from that of our N-cTnC crystals despite of the high sequence identity. High variability in structural conformations between N-TnC homologous structures suggested that this was a possibility. Secondly, there could be fundamental problems with the crystal datasets and twinning was therefore suspected.

2.3.5 **Twinning analysis**

The twinned crystals can not be distinguished by examination of the crystal morphology. However, three aspects of the datasets appeared to suggest possible twinning. Firstly, the crystals belonged to the trigonal/hexagonal space group system which is prone to twinning. Secondly, as seen in table 2-1, crystals in trigonal/hexagonal space groups system ‘appear' to have P622 space group as our datasets when they are perfectly twinned (Yeates 1999). If this is the case, then the true space group might be any space group that belongs to the trigonal/hexagonal space group system listed in table 2-1. Thirdly, when the space group is erroneously assigned, the unit cell may not appear large enough to accommodate the number of molecules because of the erroneously high symmetry (Yeates 1997). In our case, there is only 1 molecule in the asymmetric unit with the Matthew coefficient of approximately around 2.0 $Å^3$/Da (less than 40% solvent content). The solvent content is below the average value (~50%) and this suggests an unusually tight packing of the protein chain in the unit cell, indicating the possibility of twinning.

Twinning analysis was carried out using the program DETWIN on the crystal datasets rescaled as P6 or P3 space groups. Figure 2-9 shows the typical resulting plots of cumulative distribution of H versus absolute H values after performing the H-test for twinning on all three datasets. The plotted lines corresponding to the experimental data occurred with high predicted value of

α, which suggested almost perfect twinning with twin fraction value approaching 0.5. These observation was in agreement with the results obtained from Britton plots (figure 2-10), which also showed that all three datasets have a twinning fraction of approximately 0.45. Twinning analysis performed by another crystallographic program TRUNCATE also agreed with this finding and α was calculated to be between 0.45 to 0.48 for all three datasets. These observations therefore suggested that twinning could have influenced the datasets and that the existing crystallization condition invariably result in twinned crystals.

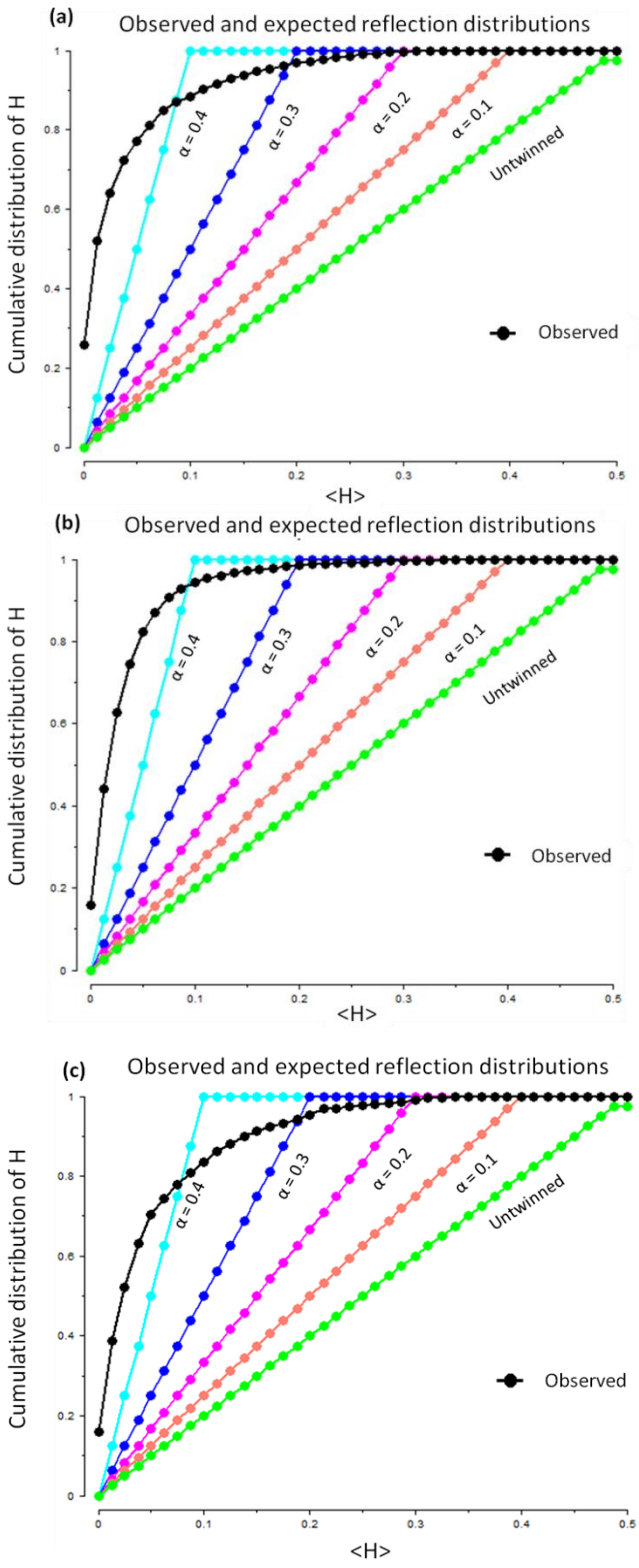
(a)
Observed and expected reflection distributions
Cumulative distribution of H
<H>
α = 0.4
α = 0.3
α = 0.2
α = 0.1
Untwinned
Observed
(b)
Observed and expected reflection distributions
Cumulative distribution of H
<H>
α = 0.4
α = 0.3
α = 0.2
α = 0.1
Untwinned
Observed
(c)
Observed and expected reflection distributions
Cumulative distribution of H
<H>
α = 0.4
α = 0.3
α = 0.2
α = 0.1
Untwinned
Observed

Figure 2-9: The H-test for twinning performed by DETWIN for (a) WT N-cTnC, (b) L29Q N-cTnC, and (c) NIQD N-cTnC.

The x-axis is the parameter H, which is the fractional difference between a pair of twin-related intensities, where $H = |I_{hkl} - I_{h'k'l'}| / |I_{hkl} + I_{h'k'l'}|$. The y-axis is the cumulative distribution of H. The observed value for the dataset is shown in black. All three calculate H are very close to 0.05, which suggests the twin fraction of 0.45, very close a perfect twin value of 0.5.

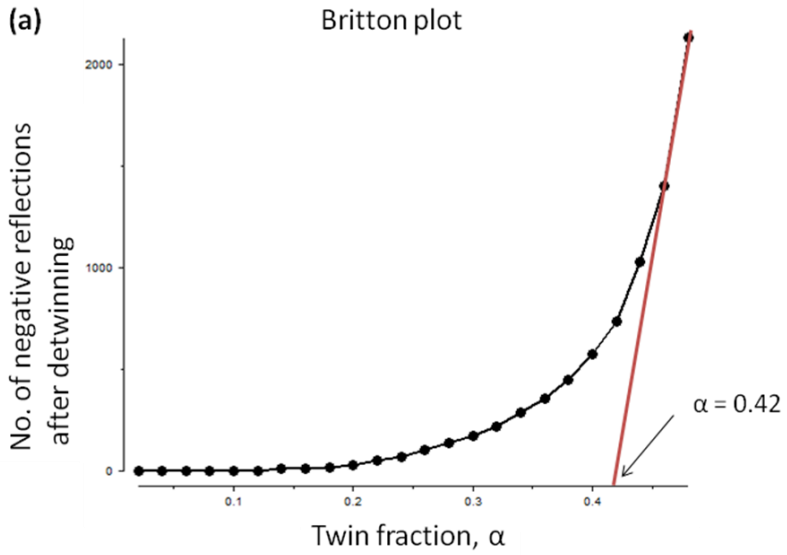

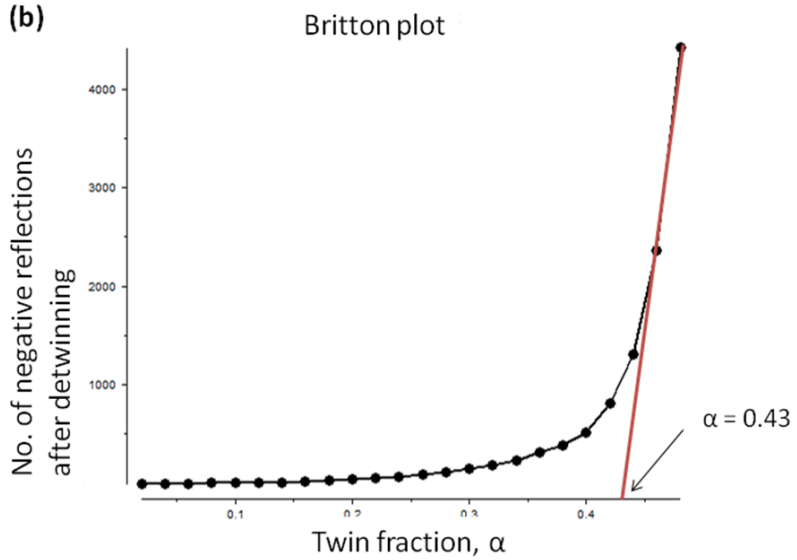

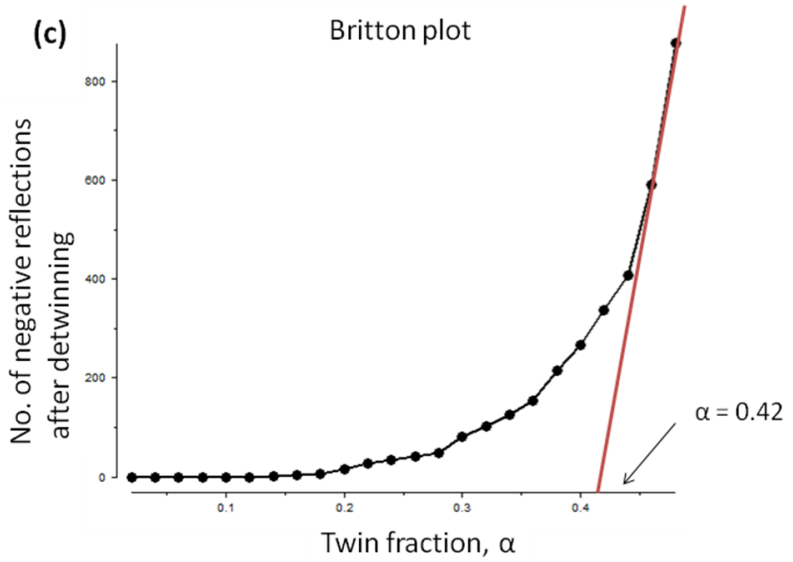

Figure 2-10: The Britton plot obtained from DETWIN shows the twinning fraction of (a) WT N-cTnC, (b) L29Q N-cTnC, and (c) NIQD N-cTnC.

The Britton plot is the number of negative intensities after detwinning as a function of the twin fraction α. Twinning fraction is estimated by where the plot starts to increase significantly. Thus, the twinning fraction estimated for WT N-cTnC, mutant L29Q N-cTnC and mutant NIQD N-cTnC is 0.40, 0.45, 0.40, respectively.

After the structure of our human N-cTnC structure was solved (discussed in chapter 3 and 4), the molecular replacement was repeated using the new structure as a search model. A single chain was used, and the flexible N-terminus and C-terminus were removed from the search model to produce a model containing only the core domain (residue 32-80). However, even this model did not yield a possible solution and thus each of the three datasets that belong to the trigonal/hexagonal space group remained unsolved.

2.4 Conclusion

WT N-cTnC, L29Q N-cTnC and NIQD N-cTnC constructs were successfully produced by site-directed mutagenesis. They were overexpressed, purified, and crystallized in a trigonal/hexagonal crystal form. The wild type N-cTnC diffracted beyond 2.4 Å, and the mutant L29Q N-cTnC and NIQD N-cTnC diffracted beyond 2.0 Å and 3.3 Å respectively. As various homologous structures are already available, molecular replacement method was initially carried out to solve the crystal structure. However, after exhaustive searches with the full-length models or models containing only the core domain generated from the extensive structure library in the PDB database, no promising solutions were found. The searches also involved over fifty models generated from the homology modelling web servers. No solutions were found using these models. Because of the failure in finding a solution, twinning was suspected to occur in the crystals. Twinning analysis performed by DETWIN and TRUNCATE indicated that the twin fraction, α, was approximately equal to 0.45, which is very close to the perfect twinning of 0.5. Since perfectly twinned crystals produce seriously flawed datasets, the best option was to grow crystal that are either untwinned or have a sufficiently low twinning fraction to allow detwinning (Yeates 1997). Therefore, a new crystallization condition was searched for and a new crystal that belonged to the twin-free orthorhombic space group was produced. Eventually, the structure was solved using the dataset collected from the new orthorhombic crystal by single anomalous diffraction method (SAD) and it will be described in details in Chapter 3 and Chapter 4.

3: CRYSTALLIZATION OF THE N-TERMINAL DOMAIN OF CARDIAC TROPONIN C IN THE ORTHORHOMBIC SYSTEM – DEALING WITH RADIATION DAMAGE

3.1 Introduction

Because the trigonal/hexagonal form of the N-cTnC crystals could not be used for structure solution, a new crystal form was searched for and discovered. The new crystal form of WT N-cTnC was obtained by the addition of deoxycholic acid and further optimization of the original crystallization condition. This new crystal form resembled an ordered hexagonal plate and belonged to a different space group, orthorhombic $P2_12_12$. In general, orthorhombic crystals are free from merohedral twinning. Molecular replacement was then used as the initial method to obtain phase information. However, after an exhaustive search with numerous homologous structures, no solution was produced. Therefore, other phasing methods, such as multi-wavelength anomalous diffraction (MAD) and single wavelength anomalous diffraction (SAD) were carried out. For this purpose, a Se-Met-incorporated version of WT N-cTnC was generated and successfully crystallized under a condition similar to the native crystal. Eventually, the structure was solved by SAD. This solution presented serious challenges as the datasets appeared to suffer from radiation damage during data collection.

Radiation damage is the physical deterioration of the crystal caused by its prolonged exposure to the oncoming X-ray beam during diffraction data collection. The data parameters that are affected by radiation damage are far

ranging and include the reflection signals (I/σI), the resolution limit, scaling B-factor, mosaicity, and unit cell dimension (Borek 2007). The scaling B-factor and mosaicity tend to increase proportionally with the exposure time to the X-ray beam. However, dramatic global damages involving loss of resolution and expansion of the unit cell volume of the crystal can even change the structural information (Borek 2007). Significantly, these effects of radiation damage can be detrimental on SAD or MAD phasing. Radiation damage results in the phasing signals from heavy atoms such as selenium decay at different rates, and this eventually leads to deterioration of the total phase information in the dataset (Gonzalez 2007). Therefore, radiation damage is often a major obstacle to solving crystal structures

The best indicator of radiation damage is increase in the scaling *B*-factor (Borek 2007). One unit of *B*-factor is equal to radiation dose of 1 MGy, which is the amount of energy absorbed per unit mass. The maximum resolution-dependent dose limit is 10 MGy per Å of resolution (Howells 2005). For example, a 2.2 Å resolution dataset would have a maximum dose limit of ~22 MGy. Alternative indicator is the plot of χ^2 as a function of exposure time (Borek 2007). χ^2 indicates how close the observed errors are close to the predicted errors for the diffraction images, and a value of 1 is theoretically an ideal value. When radiation damage occurs during data collection, the reflections collected in the middle of the overall exposure time are closer to the average (closer to ~1) than reflections collected at the beginning and the end. This creates a characteristic

U-shaped plot of χ^2 as a function of exposure time (figure 3-1) (Ramagopal 2005; Borek 2007).

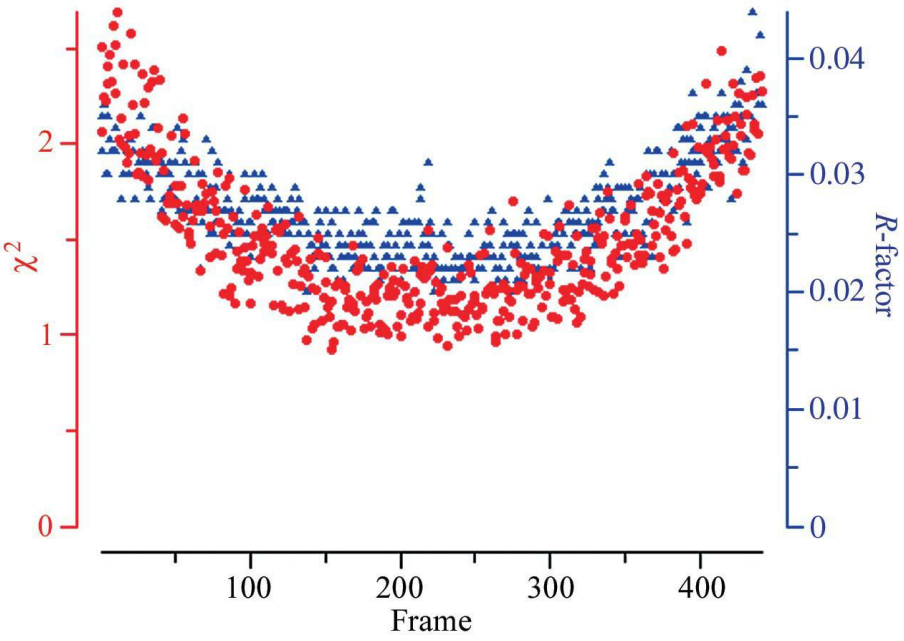

Figure 3-1: Statistics from scaling the individual images with the average of the data.

The presence of radiation changes creates a characteristic U-shape in the scaling statistics. The red circles is for value of χ^2 for individual diffraction images, and the blue triangles show the traditional scaling factor R. Figure is from Borek, 2007, J. Synchrotron Radiation (Borek 2007).

Radiation damage can also induce specific chemical changes on the protein involving loss of side chains (Holton 2009). Examples include the breakage of disulfide bonds (Addlagatta 2001; Banumathi 2004) and 'decarboxylations' of acidic residues which could even lead to misinterpretation of biochemical mechanism (Ko 1999). Several studies have been done on the effect of specific radiation damage on protein side chains (Burmeister 2000; Ravelli 2000; Weik 2000) and found that cysteine, tyrosine, and acidic residues such as

aspartic acid and glutamatic acid are particularly susceptible for radiation damage.

In summary, two SAD datasets were collected from selenium-methionine (Se-Met) incorporated N-cTnC protein crystals. They were used to yield the phase information of the wild type human N-cTnC and to refine it to 2.2 Å resolution. This chapter outlines the method used to solve the structure of N-cTnC. The solved structure also revealed the role played by the essential additive, deoxycholic acid, added to the crystallization of the new crystal form. The protein fold, the cadmium binding sites, the deoxycholic acid binding site, and comparison with other homologous structures will be discussed in the next chapter.

3.2 Materials and methods

3.2.1 Crystallization of the native orthorhombic crystal of WT N-cTnC

Several methods were tried to produce a twinning-free crystal. First, an additive screen kit was used with the original crystallization condition (0.05M $CdSO_4$, 1.0M NaOAc, and 0.1M Hepes pH 7.5). 1 µL of additive solution listed in table 3-1 was added to the final crystallization drop. Second, drugs such as bepridil that have been shown to bind to homologous N-cTnC protein were added to the crystallization drop (Li 2000). Third, new crystal growth techniques were also tried, such as the hanging drop method and the oil batch method. In the oil batch method, a thin layer of paraffin oil with a volume of 200µL was laid on the crystallization reagent (Hampton Research) in the 24-well plate. Fourth, different

temperatures (4°C and 19°C) and various drop sizes (0.5 µL, 1 µL, and 2µL) of protein solution were tried. Finally, the WT N-cTnC produced crystals that was significantly different from the trigonal/hexagonal crystal form with the addition of the additive, 0.1M deoxycholic acid (D7 from table 3-1), in the final crystallization drop. It was further optimized by screening different pH buffer (pH 4.6 to pH 9.5) and concentration of cadmium sulphate and sodium acetate in the original condition. After all, the native WT N-cTnC produced crystals that belonged to orthorhombic $P2_12_12$ space group with unit cell dimensions of 51.7 Å × 81.7 Å × 100.3 Å. The new crystallization drop contained mixture of the protein and the reservoir (0.05M $CdSO_4$, 0.60 M NaOAc, and 0.1 M Tris pH 8.0) with the addition of 1 µL of 0.1M deoxycholic acid. Crystals formed in the sitting-drop 24-well plate at room temperature after one week. Prior to data collection, the crystal was transferred to a cryoprotectant solution, consisting of the same components as the mother liquor but with 30% of the water replaced with glycerol, and the omission of deoxycholic acid. Crystals were incubated in the cryoprotectant condition for approximately 10 minutes before it was flash-frozen in liquid nitrogen.

Table 3-1: List of additives screened during crystallization experiments.

1-2	0.1M Cadmium Chloride
1-3	0.1M Calcium Chloride
1-4	0.1M Cobalt Chloride
1-5	0.1M Copper Chloride
1-6	0.1M Magnesium Chloride
1-7	0.1M Manganese Chloride
1-10	0.1M Zinc Chloride
1-11	30% v/v Ethylene glycol
1-12	30% v/v Glycerol
1-13	30% w/v 1, 6 Hexanediol

1-14	30% v/v 2-Methyl-2,4-Pentanediol
1-15	50% v/v PEG 400
1-17	1.0M Guanidine HCl
1-18	0.1M Urea
1-19	20% w/v 1,2,3-Heptanetriol
1-20	20% w/v Benzamidine HCl
1-21	30% v/v Dioxane
1-22	30% v/v Ethanol
1-23	30% v/v iso-Propanol
1-24	30% v/v Methanol
2-2	0.1M L-cysteine
2-3	0.1M EDTA sodium salt
2-6	30% w/v D(+)-Glucose
2-7	30% w/v D(+)-Sucrose
2-15	1M Glycine
2-17	0.1M Hexaminecobalt trichloride
2-24	30% v/v Dimethyl Sulfoxide
3-1	1.0M NH4SO4
3-2	1.0M CeCl
3-3	1.0M KCl
3-4	1.0M LiCl
3-5	2.0M NaCl
3-7	0.5M Na thiocynate
3-9	50% v/v Jaffamine
3-14	40% v/v tert-Butanol
3-16	40% v/v Acetonitrile
3-20	40% v/v Acetone
3-24	0.1M DTT
D-1	1% Triton X-100
D-2	0.1M IPTG
D-3	1% (v/v) Elugent detergent
D-4	0.1M nOctyl-2-D-Glucopyranoside
D-5	0.1M CHAPS
D-6	0.1M N-Dodecyl-N,N-dimethylamine
D-7	0.1M Deoxycholic acid
D-8	5% (w/v) Lubrol
D-9	0.1M CHAPSO
D-10	0.1M nonanoyl-N-methyl-glucamide-mega-9
D-11	0.1M BIGCHAP
D-12	0.1M Dodecyl-2-D-maltoside

3.2.2 **Data collection for the native orthorhombic WT N-cTnC crystal**

Data collection for the native WT N-cTnC crystal was performed at Beamline 8.2.1 of the Advance Light Source Center in Lawrence Berkeley Laboratory, University of California at Berkeley. It used a Quantum 315 ADSC

area detector with a crystal-to-detector distance of 270mm and 1º oscillation angle. The exposure time was 3 seconds. Three hundred and sixty images were collected and the reflections were detectable beyond 2.0Å.

3.2.3 Data processing for the native orthorhombic WT N-cTnC crystal

The datasets from the native orthorhombic WT N-cTnC were indexed, integrated, and scaled by the HKL2000 software package (Otwinowski 1997). Molecular replacement was carried out using MOLREP(Vagin 1997), PHASER (McCoy 2007), and MRBUMP (Keegan 2007). Twinning analysis was performed using DETWIN (Rees 1980; Yeates 1999) and TRUNCATE (French 1978). Homology models were built from web servers such as CaspR (Claude 2004), Phyre (Bennett-Lovsey 2008), and CHAINSAW (Stein 2008).

3.2.4 Over-expression of Se-Met-incorporated N-cTnC proteins and purification

Se-Met-incorporated protein was grown in M9 minimal media. It was prepared by adding 200 mL 5 × M9 salts (The 5X m9 salts were prepared by dissolving 64.0 g of sodium phosphate penta-hydrate, 15.0 g of dibasic potassium phosphate, 2.5 g of sodium chloride, and 5.0 g of ammonium chloride in 1 litre of deionized water. The solution was then autoclaved.), 2 mL of 1M magnesium sulphate, 20 mL of 20% glucose, and 0.1 mL of calcium chloride were added to 750 mL of sterile autoclaved water. The Se-Met-incorporated N-TnC was first prepared by growing an overnight culture of N-TnC/pET21/BL21(DE3) in 100 mL of LB media supplemented with 100µg/mL ampicillin at 37°C. Sixteen hours later, 500 µL of the overnight culture was

transferred to 100mL of M9 minimal medium supplemented with 100 µg/mL ampicillin and grown at 37°C overnight. Twenty millilitres of the overnight culture was transferred to 2 ×1 litre volumes of M9 minimal media and were grown for 5-6 hours at 37°C until the OD^{600} reached 0.6. Each 1 litre culture was then supplemented with the following combination of amino acids: 100 mg of lysine, phenylalanine, threonine; 50 mg of isoleucine, leucine, valine; 60 mg of L-selenomethionine. After 15 minutes, the cells were induced with 1mM isopropyl-1-thio-β-galactopyranoside (IPTG) and grown for an additional 6 hours at 37ºC. Cell pellets were then collected by centrifugation using a JLA 10.5 rotor (Beckman) at 5,000rpm for 15 min and stored at -80°C. The Se-Met-incorporated N-TnC proteins were purified using the same procedures as the native N-TnC.

3.2.5 Confirmation of Se-Met incorporation by Matrix-assisted laser desorption/ionisation-time of flight mass spectrometry (MALDI-TOF MS)

To confirm the full incorporation of selenium atoms into the N-cTnC protein, Matrix-Assisted Laser Desorption Ionization (MALDI) mass spectrometry was performed on a MALDI-LR time of flight (TOF) spectrometer (Waters Corp., Manchester, UK) in positive ion mode, using a matrix of Sinapic acid saturated in 50% acetonitrile. The instrument was operated in linear mode with a pulse voltage = 1400 V, source voltage = 15, 000 V, a multichannel plate detector potential difference of 1850 V and a TLF delay of 500 ns. Samples were desorbed with a nitrogen laser (l = 337 nm) and the ion signals detected from 50 laser shots with sample times of 5ns were summed for each mass spectrum archived. Mass spectra were recorded over an m/z range of 2000-20000.

Myoglobin, Cytochrome C, and Adrenocorticotropic hormone fragment 18-39 (Sigma Chemical Co., St. Louis, MO, USA) were used as calibration standards.

3.2.6 **Crystallization of Se-Met-incorporated WT N-cTnC**

The crystals used for MAD and SAD data collection were grown by the sitting-drop vapour-diffusion method. The crystallization drop was prepared by mixing 1 µL of purified protein (10-12 mg/mL) with 1µL of reservoir solution and equilibrated against 1mL of reservoir solution. The Se-Met-incorporated WT N-cTnC protein produced crystals in the space group $P2_12_12$ with unit cell dimensions of 51.9 Å × 81.9 Å × 100.5 Å (α = β = γ = 90°). It has four molecules in the asymmetric unit and a Matthews coefficient of 2.65 (53.5% solvent). The optimized crystallization reservoir condition was 0.05M $CdSO_4$, 0.9M NaOAc, pH 8.0 Tris buffer with the addition of 1µL of 0.05M deoxycholic acid to the final crystallization drop. The crystallization was conducted at room temperature for one week. Prior to data collection, the crystal was transferred to a cryoprotectant solution, which consists of the same components as the reservoir solution but with 30% of the water replaced with glycerol the omission of deoxycholic acid. Crystals were incubated in the cryoprotectant solution for approximately 10 minutes before they were flashed cooled in liquid nitrogen.

3.2.7 **Data collection for Se-Met-incorporated WT N-cTnC**

Data collection on the Se-Met-incorporated WT N-cTnC crystal was performed at Beamline 081D-1 of the Canadian Light Source, Canadian Macromolecular Crystallography Facility, University of Saskatchewan at

Saskatoon using the Mar225CCD X-ray detector. The crystal-to-detector distance was 180mm with 1º oscillation angle. Peak, remote, and inflection datasets were collected for each Se-Met-incorporated crystal. The best two datasets collected were the ALI_A peak data and AL281_C4a_peak data. For ALI_A peak data, 150 images were collected with 1° of oscillation. The crystal-to-detector distance was 180mm and reflections were detectable up to 2.07Å. For AL281_C4a peak data, 180 images were collected with 1° of oscillation. The crystal-to-detector distance was 180mm and reflections were detectable up to 2.20 Å.

3.2.8 **Phasing, structure determination, and refinement**

The peak dataset of AL281_C4a collected at the wavelength λ = 0.98086 was used for phase calculation by the single wavelength anomalous dispersion (SAD) method. Diffraction images were processed with HKL3000 (Otwinowski 1997; Otwinowski 2000; Minor 2006). Heavy atom position search was performed with HKL3000 using a combination of SHELXC and SHELXD (Sheldrick 2008). The refinement of heavy atoms positions and the initial phasing was performed with MLPHARE (Otwinowski 1991) followed by solvent flattening with DM program (Cowtan 1994). Only 10% of the structure could be built automatically using SOLVE/RESOLVE (Terwilliger 1999) and ARP/wARP (Tikhonov 1977; Perrakis 1997). The rest of the model was built manually by visual inspection of the electron density map using COOT (Emsley 2004). Iterative steps of manual improvement of the model and subsequent density

modification in PHENIX (Adams 2002) was carried out to trace each of the protein chains.

The peak dataset of ALI_A collected at wavelength λ = 0.98066 was used for structure refinement. The structure was refined using the program REFMAC5 (Winn 2001) and Simulated Annealing (Afonine 2005) in PHENIX version 1.3 (Adams 2002). The final models were obtained by running restrained refinement with Translation Liberation Screw Rotation (TLS) restraints obtained from the TLS motion determination server (Painter 2006).

3.3 Results and discussion

3.3.1 Crystallization of the native orthorhombic crystal of WT N-cTnC

Several approaches were used to obtain a twinning-free crystal for WT N-cTnC, L29Q N-cTnC, and NIQD N-cTnC. However, only the WT N-cTnC was able to produce the new crystal form that belonged to the orthorhombic $P2_12_12$ space group (figure 3-2). Addition of bepridil to the purified protein did not produce any crystals. The optimal temperature for crystal growth was at room temperature for a period of one week.

Figure 3-2: The orthorhombic crystal of native WT N-cTnC. The crystal dimension is approximately 0.30 mm × 0.25 mm × 0.05 mm.

3.3.2 Data processing for the native orthorhombic crystal of WT N-cTnC

The crystal of WT N-cTnC appeared to belong to the orthorhombic $P2_12_12$ space group. It has four molecules per asymmetric unit with a Matthews coefficient of 2.6 $Å^3$/Da (53.0% solvent content). It diffracted beyond 2.2 Å (table 3-2). Analysis of the dataset indicated that this crystal was free of twinning. Molecular replacement method was chosen to solve the crystal structure. Similar approaches to those described in chapter 2 were used. The full-length N-cTnC models or models containing only the core domain from the homologous structures were used. Fifty models built with the homology modelling programs such as CHAINSAW were also used. However, molecular replacement trials carried out with PHASER, MOLREP, and MRBUMP were completely unsuccessful. This finding suggested that the models might have a significantly different conformation from our structure. Other phasing methods such as MAD and SAD were used for structure determination. For this purpose, Se-Met-incorporated version of WT N-cTnC was produced.

Table 3-2: Data collection statistics for native orthorhombic WT N-cTnC.

	Native WT N-cTnC
Crystal parameters	
Space group	$P2_12_12$
a, b, c (Å)	51.7 x 81.8 x 100.3
α, β, γ (°)	90.0 x 90.0 x 90.0
Data collection statistics	

Number of images collected	360
Wavelength	1.00
Resolution (Å)	2.20-50.0 (2.20-2.28)
Total reflections	292289
Unique reflections	21636
R_{merge}	0.71 (0.267)
Mean (I)/σ(I)	52.8 (5.6)
Completeness	97.5 (84.0)
Redundancy	13.5 (10.5)
Mosaicity	0.311
% solvent	53.0
Matthew coefficient	2.6

3.3.2 Purification and crystallization of Se-Met-incorporated WT N-cTnC

The purification procedure described in section 2.3.3. was used for Se-Met-incorporated WT N-cTnC protein and it behaved similarity to the native WT N-cTnC. The elution fractions obtained from the hydrophobic interaction column (figure 3-3) were combined and further purified by size-exclusion chromatography (figure 3-4). The purified N-cTnC eluted at 140 mL and migrated as a 10 kDa species on a 15% SDS-PAGE gel. The N-cTnC eluting at 140 mL elution volume, which corresponded to molecular weight of approximately 30 kDa, could have suggested that it forms a trimer. However, multi-angle light scattering analysis of the N-cTnC revealed that the protein is monomeric in solution (figure 3-5). Fractions containing N-TnC were combined and concentrated to a final concentration between 10 and 20 mg/mL. Se-Met-incorporated WT N-cTnC crystallized in a similar condition as the native WT N-cTnC. The final crystallization drop contained 1µL of approximately 15 of purified protein, 1µL of optimized crystallization regent (0.05M $CdSO_4$, 0.9M NaOAc, and 0.1M Tris pH 8.0), and 1 µL of 0.1M of deoxycholic acid. The crystal resembled a plate (figure 3-6).

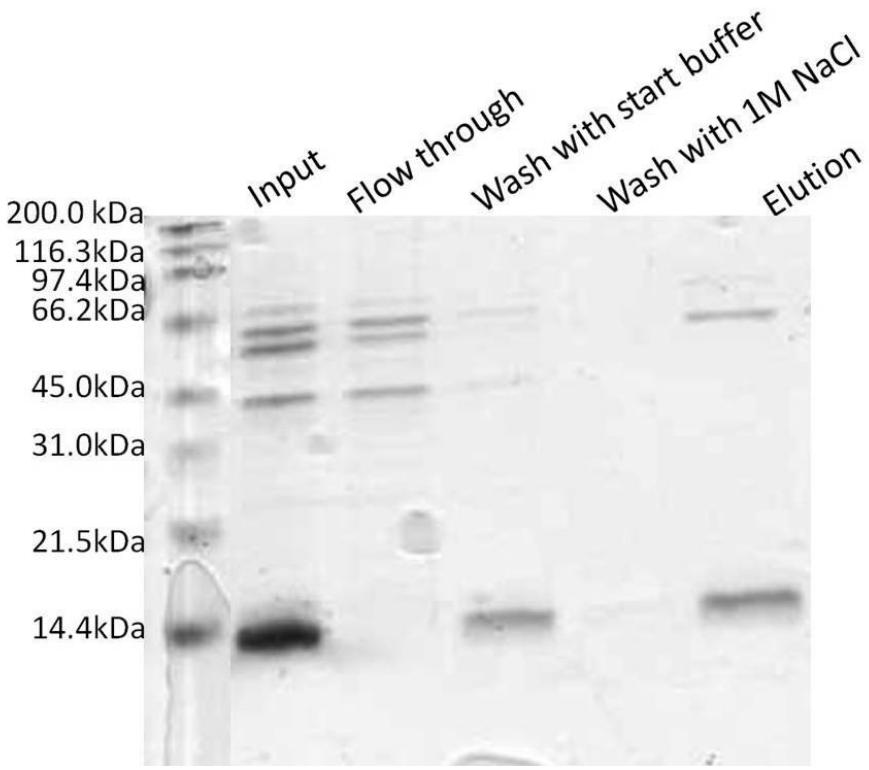

Figure 3-3: Purification of Se-Met-incorporated WT N-cTnC by phenyl-sepharose hydrophobic interaction chromatography.

All the fractions collected from the hydrophobic interaction column were analyzed by 15% SDS-PAGE and the gel was stained with Page Blue solution.

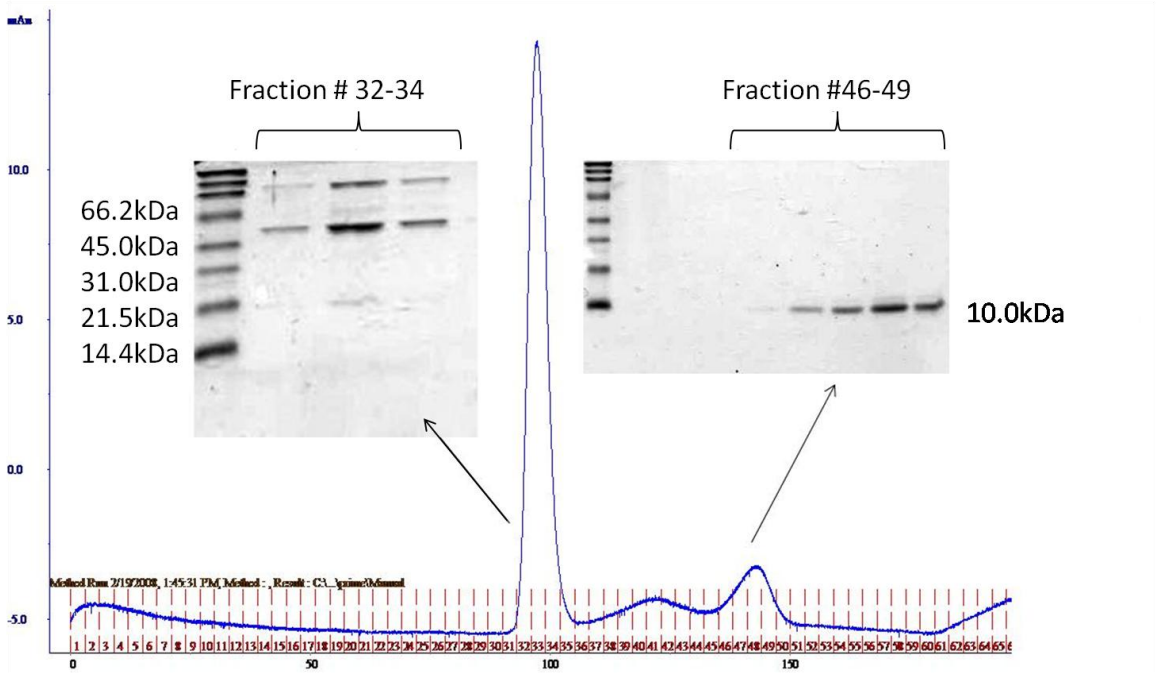

Figure 3-4: Chromatogram obtained from gel-filtration for Se-Met-incorporated WT N-cTnC.

The large peak, eluted at the void volume at 100 mL, represents the proteins of higher molecular weight. The smaller peak at approximately 140 mL, represents the 10kDa N-cTnC protein. The fractions were analyzed by 15% SDS-PAGE and the gel was stained with the Page Blue solution.

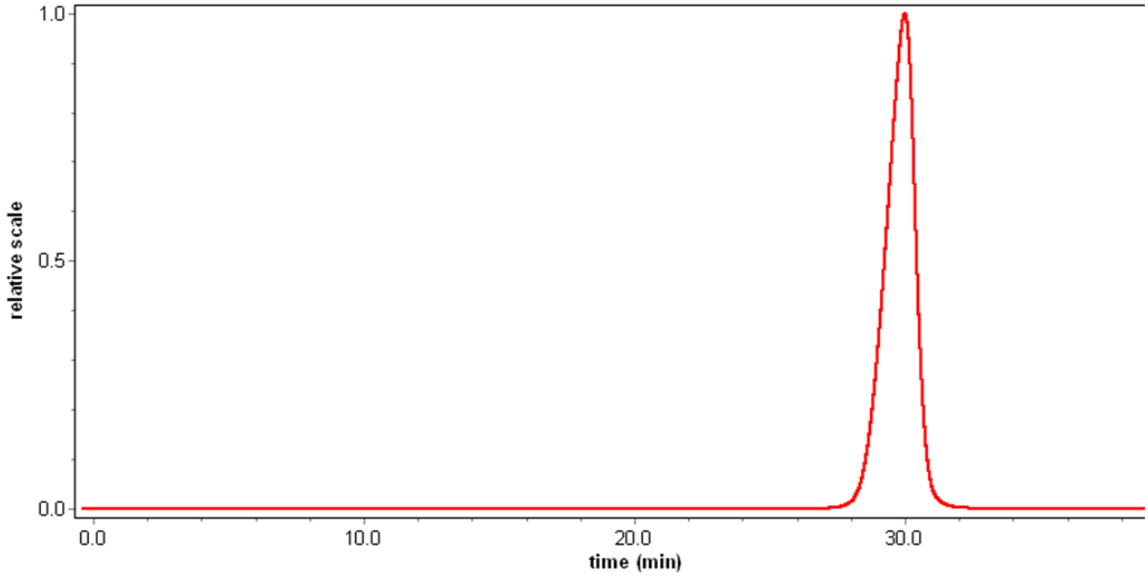

Figure 3-5: The light scattering analysis of WT N-cTnC.

The elution of WT N-cTnC from the column Superdex 200 shows that WT N-cTnC is mono-dispersed in solution, and the molar mass calculated for the peak is ~10.0kDa, which is the molecular weight of an N-TnC monomer.

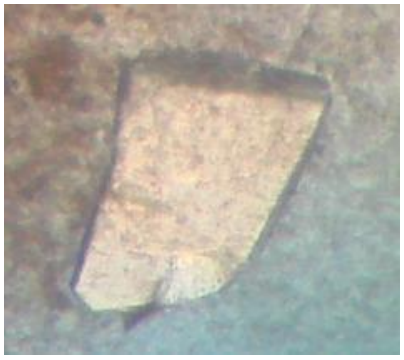

Figure 3-6: The orthorhombic crystal of Se-Met-incorporated WT N-cTnC. The dimension of the crystal is approximately 0.25 mm × 0.20 mm × 0.05 mm.

3.3.3 Confirmation of Se-Met incorporation

In order to confirm that all seven methionine residues (Met1, Met45, Met47, Met60, Met80, Met81, Met85) in the protein chain were labelled with selenium atoms, purified samples of N-cTnC protein were analyzed by MALDI-TOF mass spectroscopy. The mass spectra obtained from the native (control) and the Se-Met-incorporated proteins were compared for differences in the molecular mass (figure 3-7). The strongest peak at 10062.1Da observed in the control sample corresponds to the molecular weight of WT N-cTnC. The strongest peak at 10394.6 Da observed in the Se-Met-incorporated sample corresponds to the molecular weight of Se-Met-incorporated WT N-cTnC. The calculated mass difference is 332 Da, which approximately corresponds to the

weight difference caused by seven selenium atoms replacing the sulphur atoms in all the methionine residues, which is 328.2 Da.

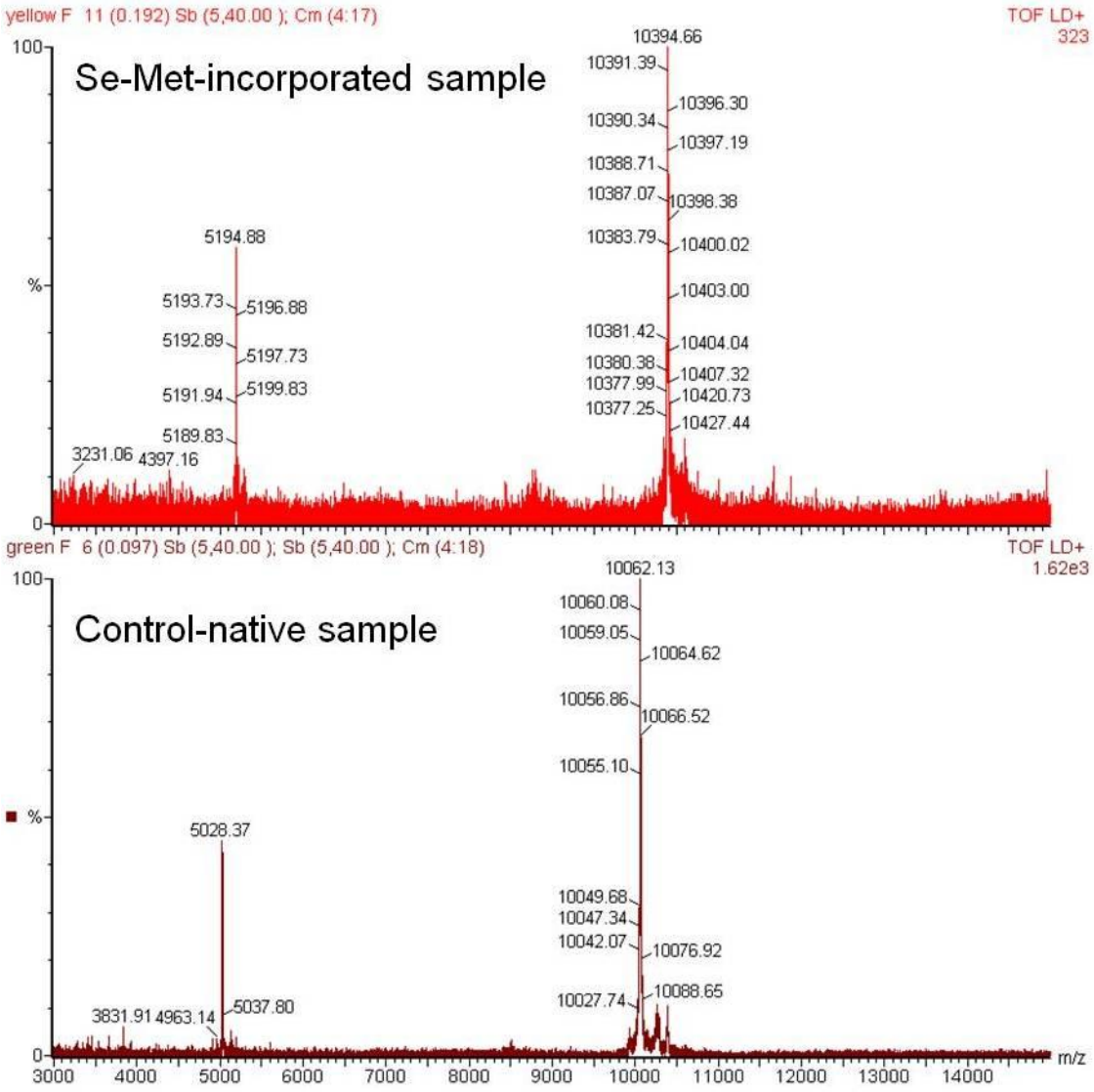

Figure 3-7: The mass spectra of the Se-Met-incorporated sample (top) and the native sample of the WT N-cTnC protein (bottom).

The strongest peak at 10062.1Da observed in the control sample corresponds to the molecular weight of WT N-cTnC. The strongest peak at 10394.6 Da observed in the Se-Met-incorporated sample corresponds to the molecular weight of Se-Met-incorporated WT N-cTnC. The calculated mass difference is 332 Da, which approximately corresponds to the weight difference caused by seven selenium atoms replacing the sulphur atoms in all the methionine residues, which is 328.2 Da.

3.3.4 Data analysis for Se-Met-incorporated WT N-cTnC

The presence of radiation damage in the AL281_C4a_peak data used for structure determination was very noticeable. Although the unit cell expansion was not significant and the average mosaicity was consistently low (~0.391), each of the B-factor and χ^2 graphs suggest radiation damage occurred during data collection. The scaling B-factor increased steadily from the beginning to the end, reaching as high as 16 in the complete dataset (figure 3-8 (a)). The plot of χ^2 as a function of exposure time fluctuates and tends to increase at the beginning and the end of the data collection (figure 3-8 (b)).

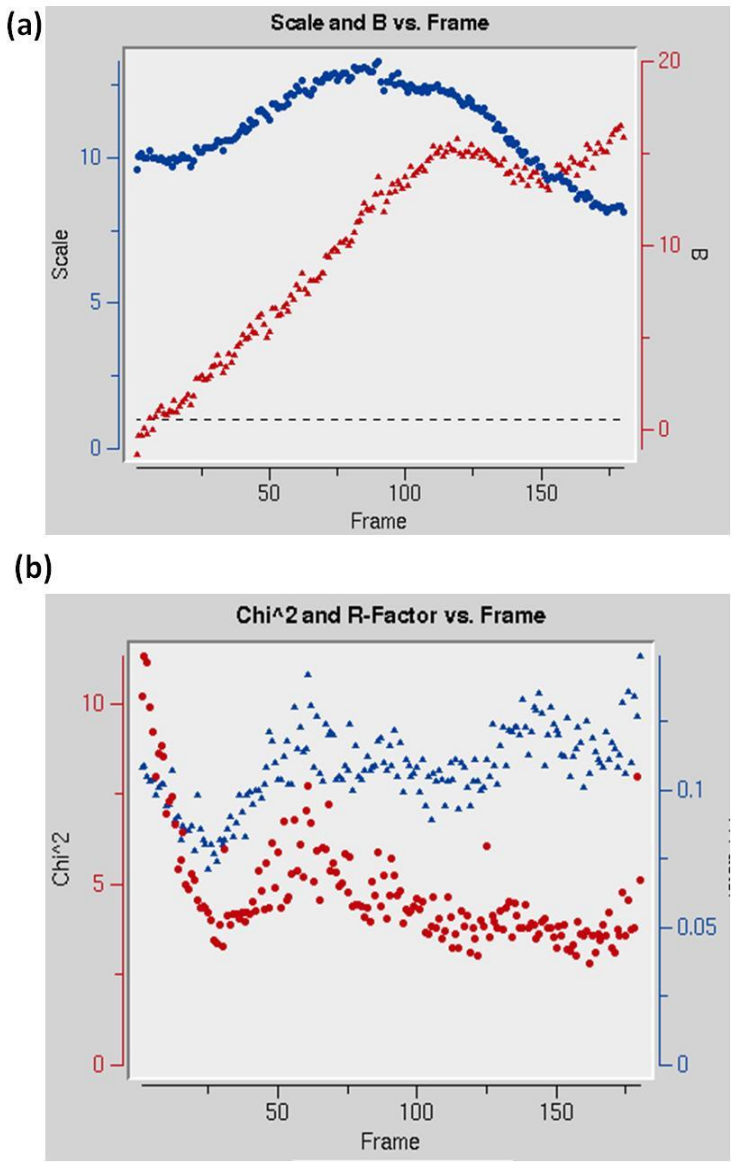

Figure 3-8: The statistical output of scaling suggests the presence of radiation damage based on the plots of (a) *B*-factor versus image number and (b) the X^2 and R-factor versus frame number.

(a) The steadily increasing value of *B*-factor (red) to as high as 16 towards the end of the image collection indicates severe radiation damage. The blue line represents the scale factor. (b) The X^2 value (red) is unstable and tends to increase at the beginning and at the end, also suggesting the presence of radiation damage. The blue line represents the R_{factor}.

3.3.5 **Phasing**

Two datasets were used to solve and refine the structure of WT N-cTnC. Table 3-3 lists the complete data collection statistics for each dataset. First, the peak dataset AL281_C4a was used for heavy atom position search and phase calculation. Because of the radiation damage, only 100 images (from 10^{th} –110^{th}) were indexed, scaled and used for the subsequent heavy atom search and phasing. SHELXC (Sheldrick 2008) analysis indicated that the anomalous signal level extended only to 2.8 Å, therefore, the heavy atom search was limited to this resolution range.

Because there are 7 Met residues per protein chain and four protein chains were predicted in the asymmetric unit, the total expected number of heavy atoms was 28. However, because Met1 and Met85 are located within the flexible C- and N-terminal regions, they might not contribute strong anomalous signal that can be used for phasing. The initial search resulted in 39 heavy atom positions with a correlation coefficient of 43.99%. The refinement of the heavy atom positions performed by MLPHARE (Otwinowski 1991) resulted in 20 refined heavy atom positions that were separated from another 19 weaker heavy atom positions. These 20 heavy atoms corresponded to the Se-Met residues located in the core domain of the protein chains. Despite the presence of 20 stronger heavy atom positions, the electron density maps generated were not clear enough for automated model building. Therefore, most of the model was built manually thorough inspection of the electron density map in COOT (Emsley 2004).

The density map was gradually improved by many iterative steps of model building and incorporating the improved model in the subsequent runs of density modification using PHENIX (Adams 2002). Almost 90% of the model was completed using this method. The other ALI_A peak dataset scaled using only 100 images was used for subsequent structural refinement for two reasons. First, it was a higher resolution dataset that extended to 2.2 Å with 99.1% completeness in the highest resolution bin. Second, its lower R_{merge} statistic and larger mean(I)/σI overall indicated that it was more reliable dataset with a stronger signal-to-noise ratio.

Table 3-3: The data collection statistics for AL281_C4a peak data and ALI_A peak data.

	AL281_C4a_peak		**ALI_A_peak**	
	SAD data		SAD data	
	180 images	100 images	150 images	100 images
Crystal parameters				
Space group	$P2_12_12$	$P2_12_12$	$P2_12_12$	$P2_12_12$
a, b, c (Å)	52.0, 83.0, 100.8	51.8, 81.8, 100.5	51.9, 81.9,100.5	51.8, 81.8, 100.5
α, β, γ (˚)	90.0, 90.0, 90.0	90.0, 90.0, 90.0	90.0, 90.0, 90.0	90.0, 90.0, 90.0
Data collection statistics				
Wavelength	0.98068		0.98066	
Resolution(Å)	2.5-50.0 (2.5-2.6)		2.2-50.0 (2.2-2.8)	
Total reflection	104687	759354	134481	85499
Unique reflection	15373 (1442)	14864 (1414)	22287 (2174)	22061 (2192)
R_{merge}	0.100 (0.292)	0.081 (0.091)	0.072 (0.209)	0.067 (0.176)
Mean (I)/σ(I)	33.7 (4.6)	26.2 (4.1)	35.4 (6.5)	28.4 (5.7)
Completeness	98.8 (95.6)	95.5 (93.8)	99.4 (98.1)	98.4 (99.1)
Redundancy	6.8 (5.7)	4.0 (3.4)	6.0 (5.6)	3.9 (3.8)

3.3.6 **Structure determination and refinement**

In summary, the human N-cTnC protein that spans residues 1-89 produced an orthorhombic crystal ($P2_12_12$) with unit cell dimensions of 51.9 × 81.9 × 100.5 Å (α = β = γ = 90°). There are 4 molecules in the asymmetric unit with a Matthews coefficient of 2.7 $Å^3$ Da^{-1}(53.5% solvent). Two of the protein chains in the asymmetric unit are related to other two chains by a translation with a (0.5, 0.5, 0.5) vector, a condition described as translational pseudosymmetry. The final refined structure of all four chains has an R_{factor} of 20.4 % and an R_{free} of 29.2 %. The average B-factor of the structure is 42.0 $Å^2$ (see table 3-4 for summary of refinement statistics). The high B-factor normally correlates with flexible regions, which is a feature observed in other homologous structures (Takeda 2003). Several residues at the N-terminus and C-terminus could not be modelled due to a lack of electron density, indicating the high thermal motion within these regions. In addition to the protein chain, there were eighteen cadmium ions found in the structure. They are probably derived from cadmium sulphate, which was an essential component of the crystallization reservoir solution. Sixteen of these Cd ions are bound within the EF-hand motif, and 2 of them are found outside the binding loop. There are 8 deoxycholic acid (DXC) molecules found associated with the protein chains. Each chain is associated with 2 DXC molecules, one located in the central hydrophobic cavity, and the other located in between helix N and helix A. The root mean square deviations of bonds and angles were close to ideal values. The Ramachandran plot analysis was used to assess the main-chain conformational angles of the proteins. The

majority of the non-glycine residues are sterically favoured, and no non-glycine residues are found in the sterically disallowed area (figure 3-9).

Table 3-4: Refinement statistics for Se-Met-incorporated orthorhombic WT N-cTnC

	Se-Met-incorporated WT N-cTnC	
Refinement statistics		
Protein molecules in ASU	4	
Residues	356	
Water molecule	220	
Total number of atoms	2992	
R_{factor}/R_{free} (%)	20.4/29.2	
Average *B*-factor (Å^2)	42.0	
r.m.s.d on angels (°)	1.958	
r.m.s.d on bonds (Å)	0.020	
Ramachandran analysis (%)		
Preferred regions	219	(93.6%)
Allowed regions	15	(6.4%)
Outliers	0	(0.00%)
B-factor		
Overall	42.0	
Deoxycholic acid	70.5	
Cadmium ion	35.5	
Calcium ion	64.3	
Residues missing from the models due to a lack of electron density	Chain A: 1-2, 86-89 Chain B: 1-4, 83-89 Chain C: 1-2, 86-89 Chain D: 1-4, 83-89	

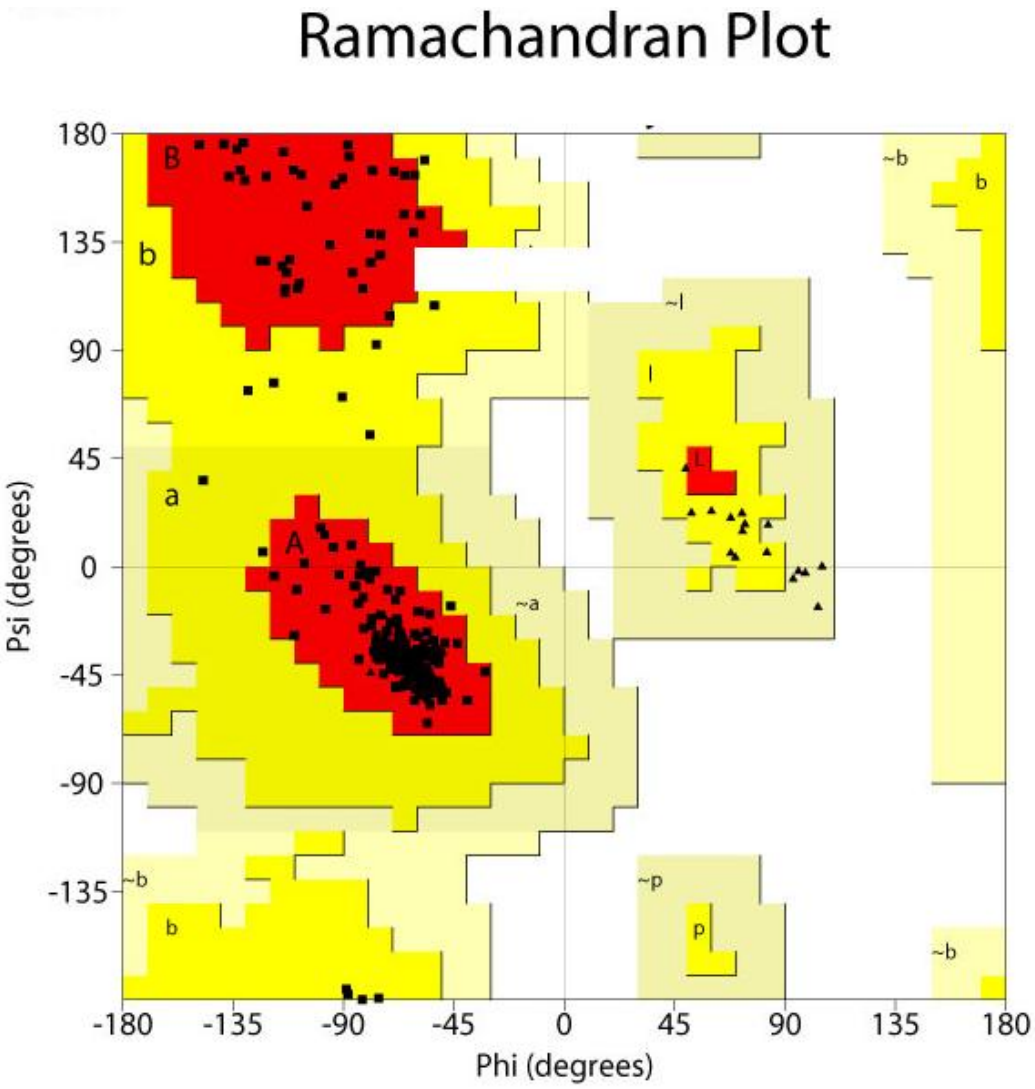

Figure 3-9: Ramachandran plot of the crystallographic model of WT human N-cTnC.

The read area indicates the most favoured region and the yellow area indicate allowed region. Black solid triangles indicate glycine residues and black solid squares indicate other residues rather than glycine.

4: STRUCTURAL ANALYSIS OF HUMAN N-CTNC

4.1 Protein fold of N-cTnC

Human N-cTnC is a small protein that is 89 residues in length and has a molecular weight of 10kDa. In this crystalline form, four molecules form two dimers in the asymmetric unit. These molecules are named chains A through D (figure 4-1). The core structure of each chain contains two EF-hand motifs. Each EF-hand motif contains a helix-loop-helix conformation. Chain A and B assemble as a dimer, which is related to the chain C and D dimer by a two-fold non-crystallographic symmetry (figure 4-2).

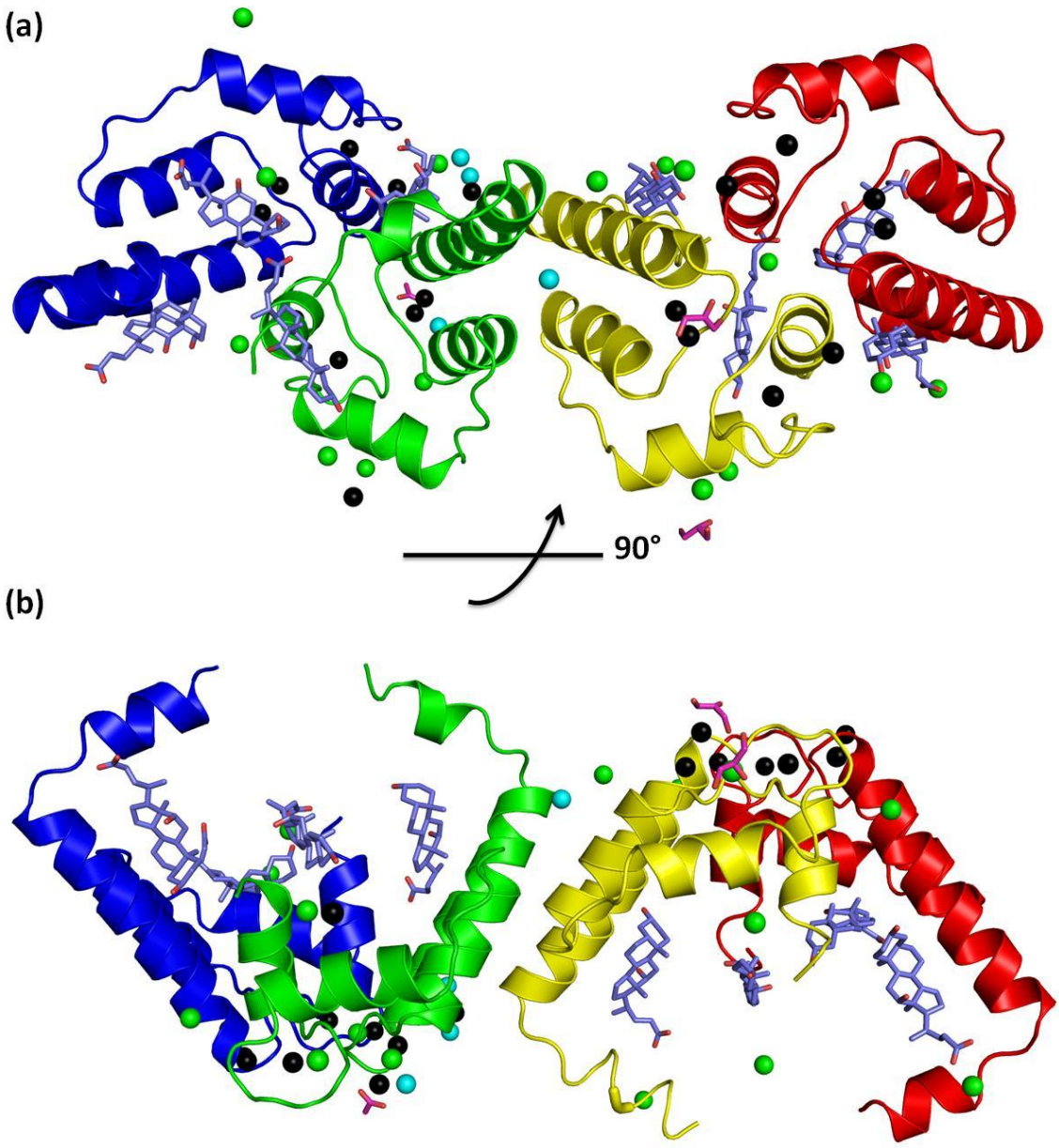

Figure 4-1: The overall conformation of the four proteins chains in the asymmetric unit.

(a) The cartoon representation of the overall conformation of all four chains. Chain A (blue) and chain B (green) forms a dimer, which is related to chain C (yellow) and chain D (red) by a two fold symmetry. Cd^{2+} ions are shown in black sphere, Ca^{2+} ions are shown in green spheres, and Cl^{-} ions are shown in cyan spheres. The deoxycholic acid ligands are shown in blue sticks. The glycerol molecule and acetate ion are shown in magenta. (b) The side-view of (a).

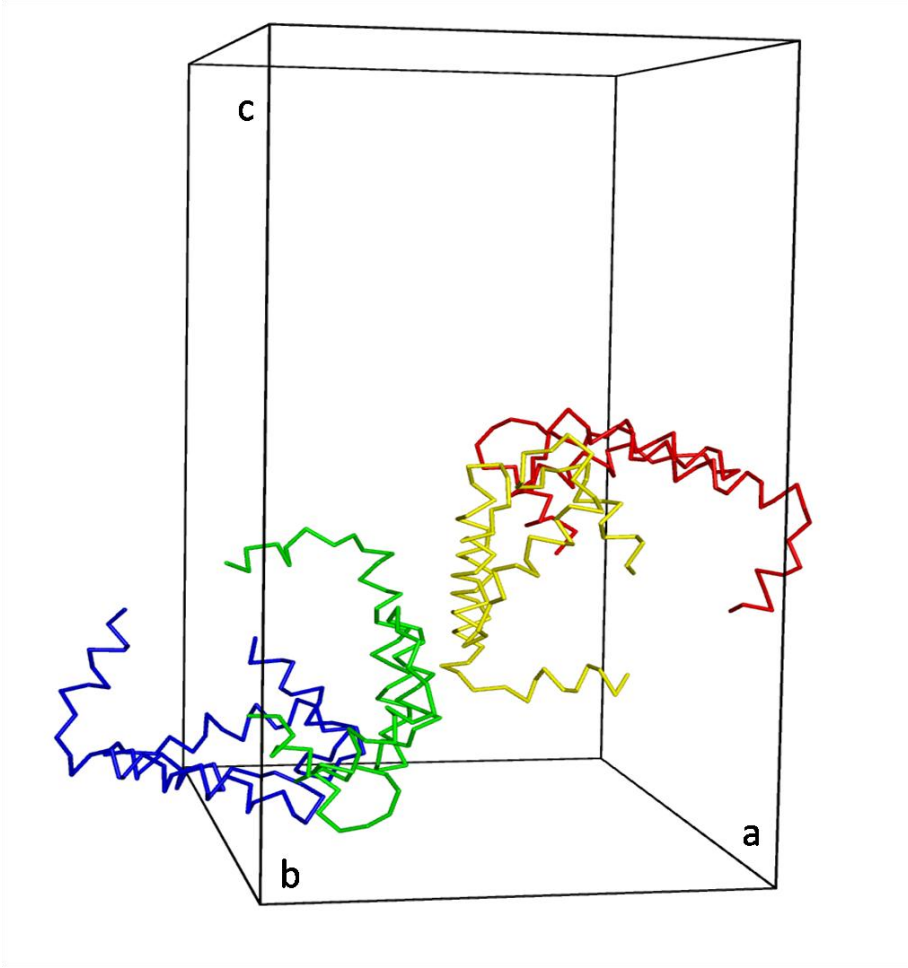

Figure 4-2: The orientation of the four protein molecules (chains) in the asymmetric unit.

Chain A (blue) and chain B (green) form a dimer, which is related to a dimer formed by chains C (yellow) and chain D (red) by a two-fold symmetry operation. The axis is labelled (a = 52.0 Å, b= 83.0 Å, c= 100.8 Å).

Because all four molecules in the asymmetric unit adopt an identical protein fold, chain A is used as an example for protein analysis. Figure 4-3 shows that N-cTnC is a small protein constructed from two-EF hand motifs and an short α-helix at the N-terminus (residues 3-11). The first EF-hand motif consists of a long α-helix A (residues 14-28), the EF-hand binding loop I (residue 28-40), and α-helix B (residues 38-47). The second EF-hand motif consists of α-helix C (residues 54-64), the EF-hand binding loop II, and α-helix D (residues 74-81). The two EF-hand motifs are connected by a linker region that spans residues 48-53.

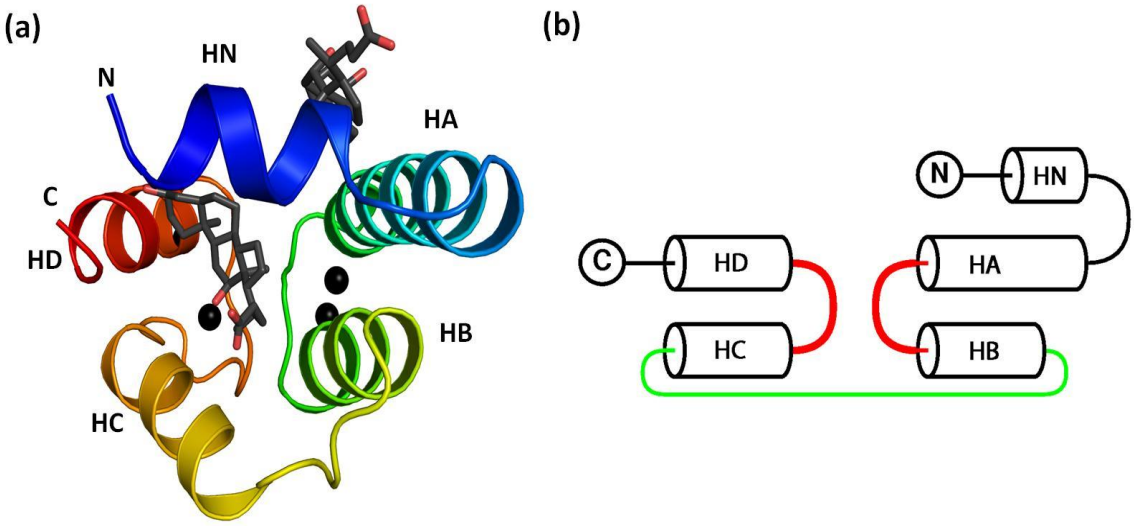

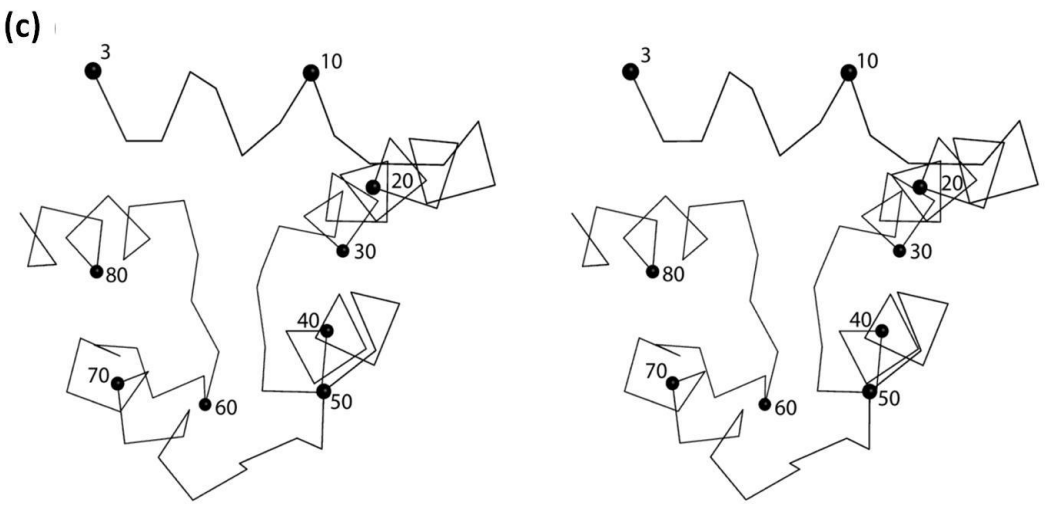

Figure 4-3: The protein fold of human N-cTnC.

(a) A cartoon rendering coloured spectrally from the N-terminus (blue) to the C-terminus (red) with the amino- and carboxyl-termini labelled. Helix N is labelled as HN, helix A is labelled as HA, helix B is labelled as HB, helix C is labelled as HC, and helix D is labelled as HD. The Cd^{2+} ions are shown as black spheres, and the deoxycholic acid molecules are shown as black sticks. (b) Schematic diagram of the N-cTnC topology. Helices are labelled as in (a). The EF-hand binding site is shown in red, and the linker region that connects HB and HC is shown in green. (c) A stereo view of N-cTnC. Every 10th residue is labelled with a sphere.

Although all four chains adopt a similar fold, there is still some structural difference. The backbone superimposition of the four chains gives a root-mean-square deviation (r.m.s.d) of 0.733 Å. The major difference between the chains lies within the terminal helices and the linker region that connects helix A and helix B. The superimposed regions with the least deviation are the two EF-hand binding loops (figure 4-4). The structural integrity within this region is well maintained because each binding loop is involved in a tight network of Cd^{2+} ion coordination that will be described in Section 4.3.

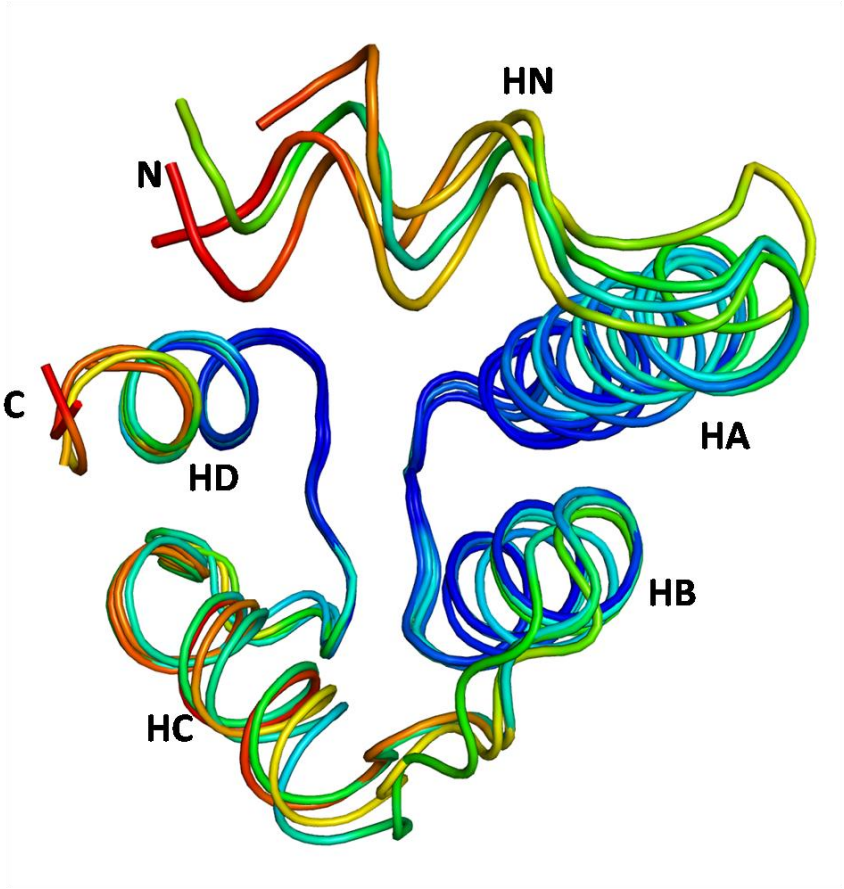

Figure 4-4: The superposition of the four chains coloured spectrally by B-factor, in which red denotes the most disordered regions and the most ordered regions are coloured blue.

The two EF-hand binding sites as well as helix A and helix B are the most ordered region. The N-terminus and C-terminus are the most disordered regions.

4.2 The dimerization interface

The two dimers of N-cTnC are held together by non-polar protein/protein interactions. The protein/protein interface between chain A and B buries approximately 668 $Å^2$ of molecular surface and is linked by one salt bridge but no hydrogen bonds. The interface is about 64% non-polar, and the residues that contribute to the interface include 27-36 of helix A and 72-82 of helix B for both

chains (figure 4-5). The second dimer formed by chain C and D has very similar protein/protein interactions. Approximately 650 $Å^2$ of the molecular surface is buried, and no hydrogen bonds are found at the interface. The interface is also about 64% non-polar and the residues that contribute to the interface are similar to those found in the AB dimer.

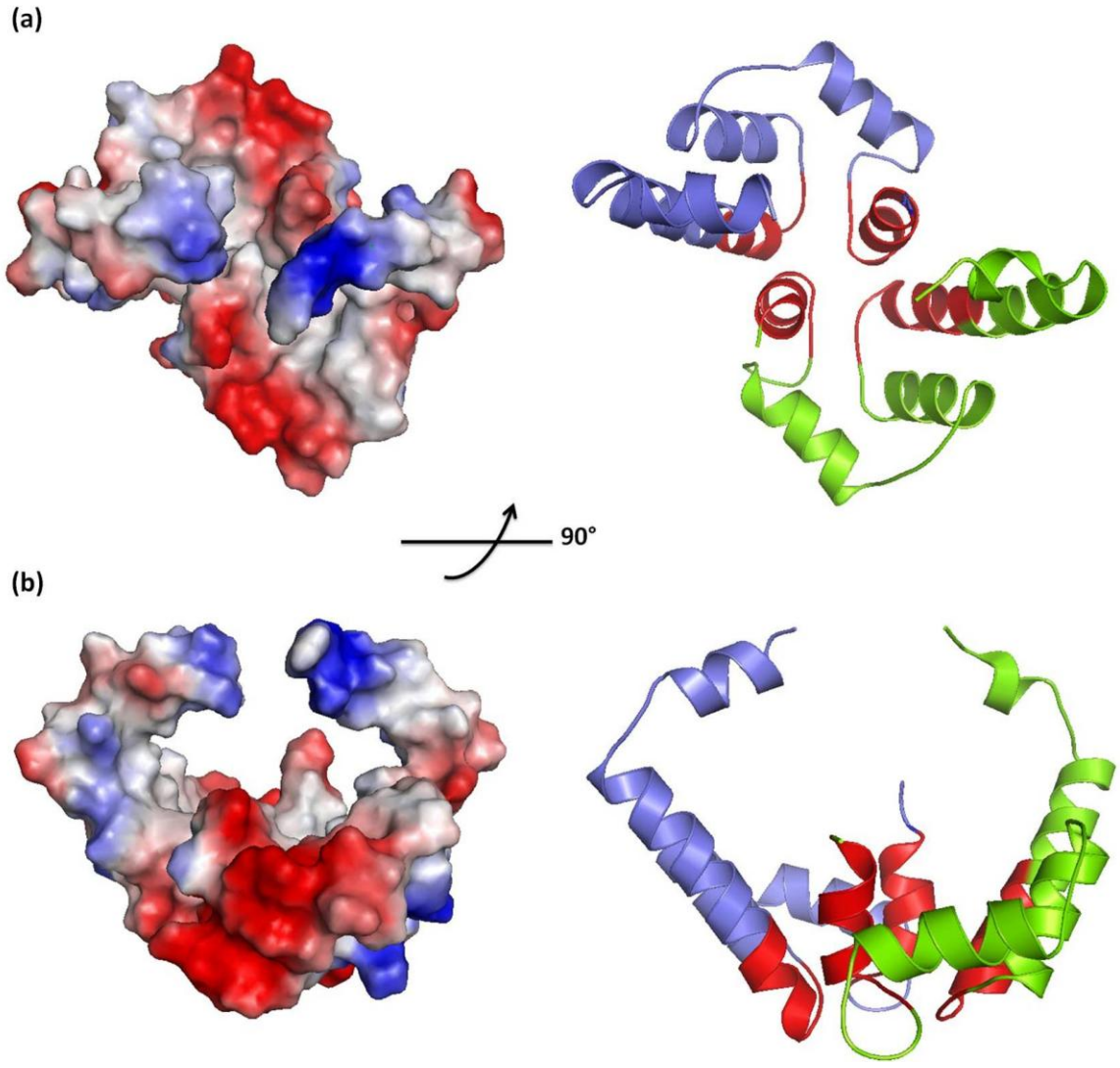

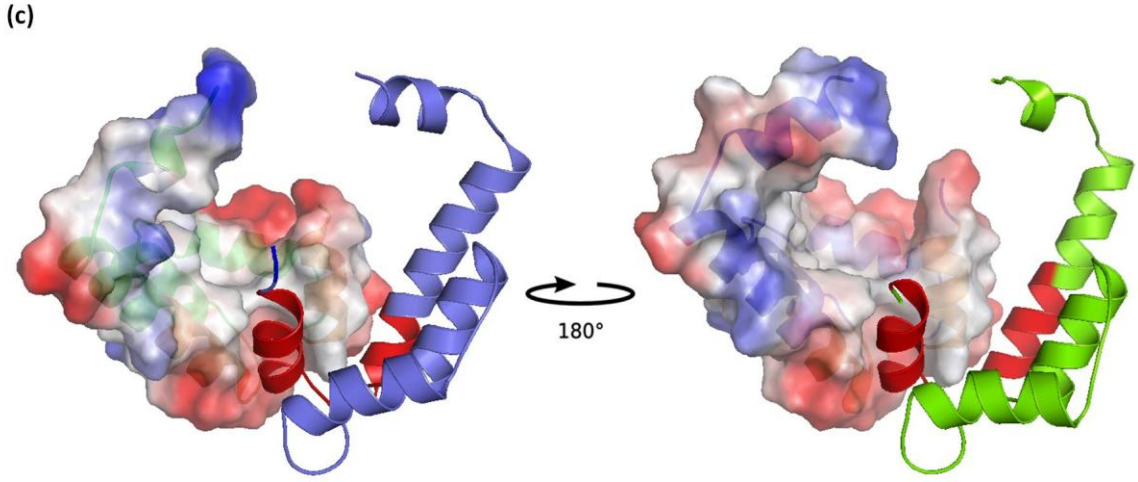

Figure 4-5: The electrostatic surface properties of the AB dimer

(a) The top view of the AB dimer. Both the vacuum electrostatic surface representation (positively charged regions, blue; negatively charged regions, red; neutral, white) and the cartoon representation (chain A, blue; chain B, green) are shown. The residues that contribute to the interface are coloured red. (b) The side view of (a). (c) The half surface representation for each monomer. The monomers are held together by non-polar interactions between the residues highlighted in red.

Although there are no hydrogen bonds at the dimer interface, there are some important hydrogen bonds that mediate the contact between the AB and CD dimers (Table 4-1). They occur through the side chains as well as the main chain atoms of chain B and C and are important for the packing between the dimers (figure 4-6).

Table 4-1: The inter-chain hydrogen bonds between the two dimers of N-cTnC.

Donor		**Acceptor**		
Residue	**Atom**	**Residue**	**Atom**	**Distance (Å)**
Lys43/B	Nζ	Glu19/C	$O^{\varepsilon 1}$	2.87
Lys43/B	Nζ	Glu19/C	$O^{\varepsilon 2}$	3.29
Arg46/B	N^{δ}	Gly49/C	O	2.85
Arg46/B	$N^{\omega 2}$	Gly49/C	O	2.84
Arg46/C	$N^{\omega 2}$	Asn51/B	$O^{\delta 1}$	2.71
Arg46/C	$N^{\omega 1}$	Gln50/B	O	2.91

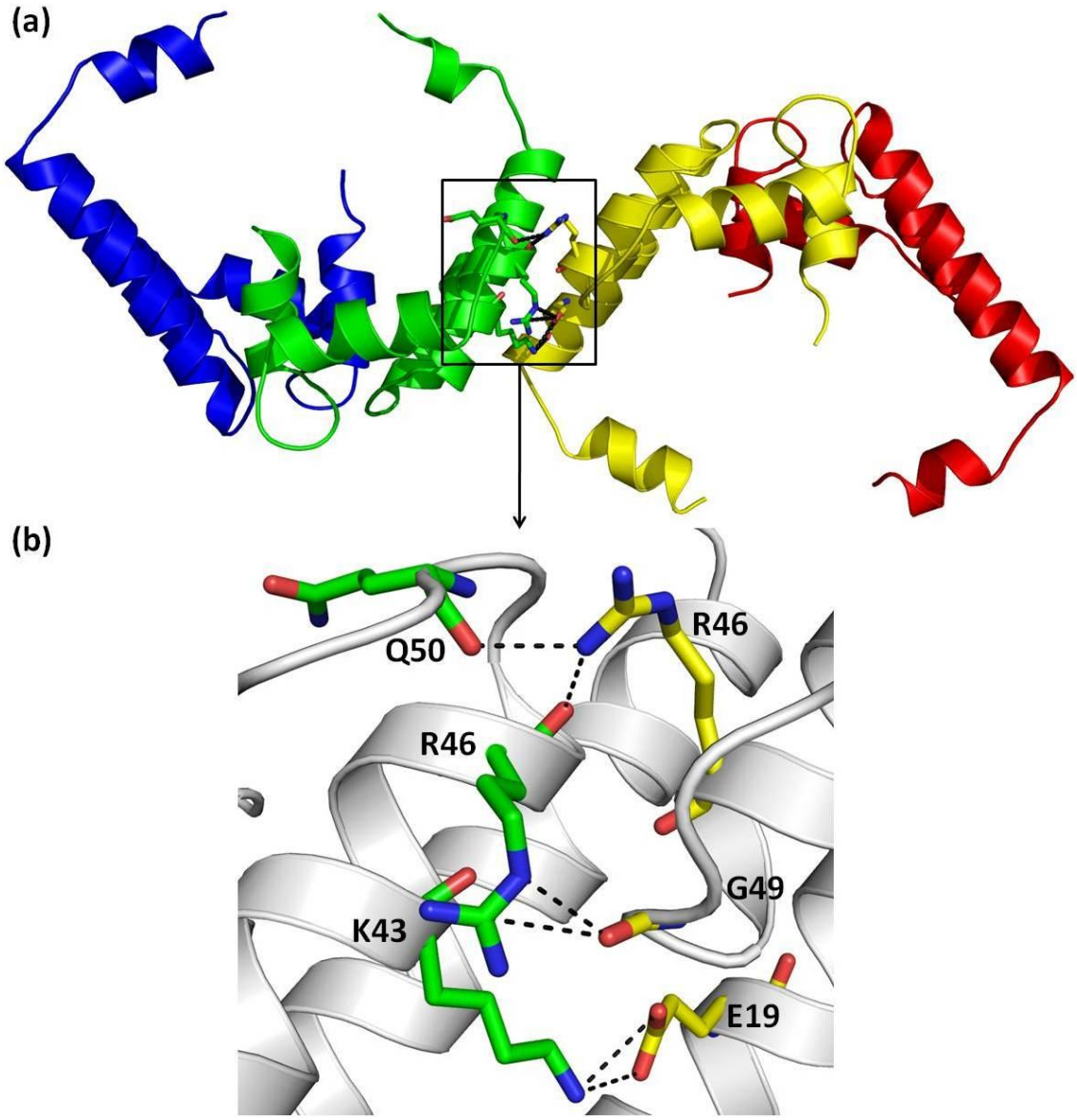

Figure 4-6: The hydrogen bonding interactions at the interface formed between chain B and chain C.

(a) Hydrogen bonding interactions at the interface formed between chain B (green) and chain C (yellow). (b) The enlarged view of the six important hydrogen bonding interactions at the interface. Glu19, Arg46, and Gly 49 belong to chain C and are coloured yellow, and Lys43, Arg46, and Gln50 belong to chain B and are coloured green.

4.3 The cadmium binding sites

One notable feature of this structure is the predominant cadmium (Cd^{2+}) coordination with each protein chain. Not only is Cd^{2+} an essential component required for the crystallization of N-cTnC, but it also displaces Ca^{2+} ions in the EF-hand Ca^{2+} binding sites I and II (EFI and EFII). This displacement is predictable because Cd^{2+} has an ionic radius of 0.97Å, which is very close to that of Ca^{2+}, 0.99Å (Rao 1996). Table 4-2 lists the comparison between Cd^{2+} and Ca^{2+} ion. Previous structural studies on metal coordination by TnC also shows that Cd^{2+} binding causes very little perturbation in the overall conformation of the protein (Rao 1996). Because Ca^{2+} was in the final protein buffer and Cd^{2+} was used in the crystallization reagent, they could both be present in the final structure.

Table 4-2: Comparison between calcium and cadmium. The information was obtained from WebElement (Winter 2009).

	Calcium	**Cadmium**
Type of metal	Alkaline earth metal	Transition metal
Atomic number	20	48
Toxicity	Non-toxic	Carcinogenic
Pauling electronegativity	1.0	1.7
Atomic radius (Å)	1.94	1.61
Ionic radius in +2 charge (Å)	0.99	0.97

Numerous studies on ligand coordination in metalloproteins provide some general trends used to distinguish different ion bindings, but they are not fixed rules (Harding 2002; Dokmanic 2008). From Dokmanic's studies on the correlation between metal ion coordination and amino acid residues, Cd^{2+} is coordinated by the side chains of Cys, His, Glu, and Asp, in order of decreasing

frequency (Dokmanic 2008). In contrast, Ca^{2+} is mainly found to be coordinated by the side chains of Asp, Glu, Asn, and the backbone carbonyl of Gly (Dokmanic 2008). In addition to examining the metal ion in relation to nearby residues, the electron density map and B-factor are used to determine the identity of the coordinated metal. Because Cd^{2+} has 46 electrons and Ca^{2+} has 18 electrons (Winter 2009) , the higher electron density of Cd^{2+} can be seen in the omit electron density of a map contoured at a high sigma level (Bouckaert 2000; Minichino 2003). Figure 4-7 (a) shows the difference in electron density (2Fo-Fc) between Cd^{2+} and Ca^{2+} when contoured at 4.0 σ. It is clear that the electron density of Cd^{2+} is much greater than that of Ca^{2+}. Figure 4-7 (b) and (c) show the electron density of Cd^{2+} in EFI and EFII contoured at 5.0 σ in the same electron density map. The density for both Cd^{2+} ions in the binding loop is still visible, but the density of Ca^{2+} can no longer be observed (graph not shown). In addition, the *B*-factor can be used as an indicator to distinguish different metal ions. The *B*-factor of Ca^{2+} was considerably lower compared to that of the main protein chains, while the *B*-factor of Cd^{2+} was in a similar range. By combining the information obtained from the omit electron density map at a high σ level and the *B*-factor range, a total of eighteen Cd^{2+} ions are found in the final structure. Sixteen of them are located in the binding loops, and two of them are found outside the loop. Interestingly, the Cd^{2+} coordination in the current structure reveals several unique features that have not been observed in other homologous structures.

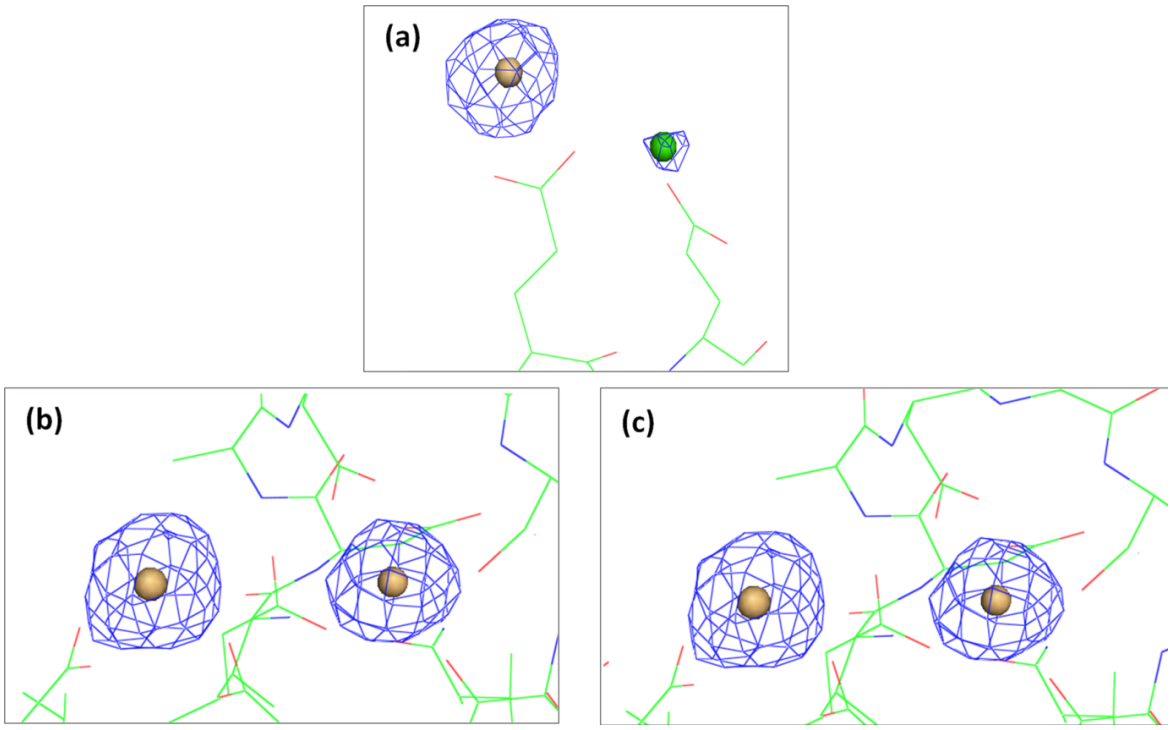

Figure 4-7: The electron density of Cd^{2+} and Ca^{2+} on a (2Fo-Fc) map at (a) σ4.0 and (b) σ5.0.

(a) The greater electron density of Cd^{2+} coordinated by Glu59/B and lesser density of Ca^{2+} coordinated by Glu63/B. The map is contoured at 4.0σ. (b) The strong electron density of the two Cd^{2+} ions in EFI in chain A. The map is contoured at 5σ. (c) The strong electron density of the other two Cd^{2+} ions in EFII. The map is contoured at 5σ. This figure was generated using PyMol(DeLano 2002).

In general, the 13-residue (28-40) EF-hand binding loop I (EFI) of cardiac TnC is dysfunctional due to the valine insertion at residue 28 and two non-polar amino acid substitutions at residues 29 and 31 (van Eerd 1975). Thus, metal coordination has not been observed due to the non-polar amino acid residue substitutions. The 12-residue (65-76) EF-hand binding loop II (EFII) is functional and able to coordinate one Ca^{2+} ion. From the other N-cTnC structures, it can be

observed that five conserved residues and a nearby water molecule provide seven ligands to coordinate the Ca^{2+} ion to form a pentagonal bipyramidal arrangement within this region. However, our N-cTnC structure shows very different metal ion coordination in both binding loops. First, unlike the other cTnC structures which have a dysfunctional EFI, the residues in our N-cTnC is able to coordinate two Cd^{2+} ions in this region. Similarly, EFII is able to coordinate two Cd^{2+} ions. This two-Cd^{2+}-ion coordination is observed throughout all four chains. In addition to the seven-ligand coordination to Cd^{2+}, five- and six-ligand coordination is observed in the structure. It should be noted that one of the two Cd^{2+} in each EF hand binding loop occupied the canonical Ca^{2+} binding site.

The residues that participate in the ion coordination are compared to other N-cTnC structures (figure 4-8). This comparison shows the sequence alignment among our N-cTnC protein, another human cardiac N-cTnC protein (1WRK), and a chicken skeletal N-cTnC protein (1AVS). In EFI of our human N-cTnC structure, four residues and residues from the symmetry-related molecules provide ligands to coordinate two Cd^{2+} ions. In the other N-cTnC structure (1WRK), there was no metal ion coordination in this region. In the N-sTnC structure (1AVS), Ca^{2+} ion coordination with six ligands and a water molecule was observed. Conversely, in EFII of our human N-cTnC, two additional residues (Asp73 and Asp75; highlighted in blue in figure 4-8) participate in the Cd^{2+} coordination.

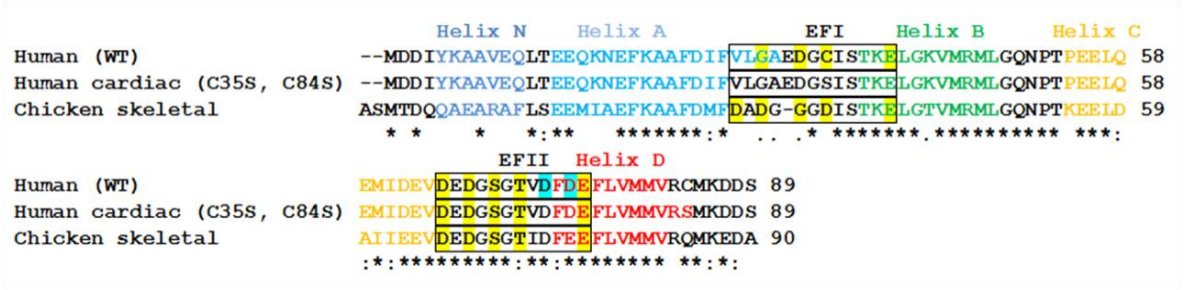

Figure 4-8: Sequence alignment of our N-cTnC structure with other N-TnC homologous structure.

The current human N-cTnC is compared to other N-cTnC structures with the two cysteine mutations (C35S, C84S) (PBD: 1WRK (Takeda 2006)) and a N-sTnC (PDB: 1AVS (Strynadka 1997)). The residues that belong to the same helix are coloured the same. The conserved EF-hand binding loop I and II are boxed. The residues that provide ligands for ion coordination are highlighted in yellow. In EFI, four residues in our human N-cTnC structure participate in ion coordination, and these residues are the same conserved residues that participate in Ca^{2+} coordination in 1AVS. In the other cardiac N-cTnC structure (1WRK), no ion coordination is observed. In EFII, the five conserved residues that provide the ion coordination in our structure is the same as in 1WRK and 1AVS. In addition, two additional residues, Asp73 and Asp75 (highlighted in blue), that normally do not participate in ion coordination in the homologous structures, provide ligand coordination for Cd^{2+} ion in our structure. The sequence alignment was generated using ClustalW 2.0.10 (Thompson 2002).

The unique Cd^{2+}-coordination in each binding loop is shown in figure 4-9 and the participating ligands and ligand-ion distances are shown in table 4-2. Because chain A and chain D are equivalent, only chain A and its Cd^{2+} ions are displayed in figure 4-9 (a). Gly30, Asp33, Cys35, and Glu40 provide seven ligands to form the vertices of the pentagonal bipyramid with Cd_{A1} (and Cd_{D1}) in the center. The five equatorial plane ligands are Cys35 O, Asp33 $O^{\delta 1}$ and $O^{\delta 2}$, and Glu40 $O^{\varepsilon 1}$ and $O^{\varepsilon 2}$. Two axial ligands are Gly30 O and Cys35 S. Unlike any

other structures, coordination of the first Cd^{2+} in EFI is achieved solely by ligands provided by amino acid residues. When compared to N-sTnC, in which one water molecule is needed as a ligand, the carboxylate group of Asp33 in the current human N-cTnC structure is oriented in a planar conformation with respect to Cd_{A1}. Thus, both oxygen atoms of the Asp carboxylate group participate in the ion coordination, and a water ligand is no longer needed. This coordination is considered the strongest as no water molecules are involved in the coordination. In general, the more water ligands, the weaker the apparent ion affinity in these binding loops (Strynadka 1989; Strynadka 1997). Even a highly ordered water molecule could be in constant exchange with the surrounding solvent. The second Cd^{2+} ion (Cd_{A2} and Cd_{D2}) is coordinated by five ligands to form the trigonal bipyramidal coordination (figure 4-9 (a)). The ligands at the equatorial plane are Cys35 S and Glu19 $O^{\varepsilon 1}$ and $O^{\varepsilon 2}$ from the symmetry-related molecule, and the axial ligands are a water molecule and Glu15 $O^{\varepsilon 1}$ from the symmetry-related molecule. The coordination of Cd_{A2} and Cd_{D2} between symmetry-related molecules allows tight packing of the protein chains in this region.

Figure 4-9 (b) shows the Cd^{2+} coordination in binding loop I of chain B (i) and chain C (ii). Unlike in chain A and chain D which have identical Cd^{2+} coordination in this region, variable Cd^{2+} coordination is observed in chain B and C. In chain B, in addition to the typical seven-ligand coordination (Cd_{B1}), Cd_{B2} adopts the five-ligand coordination to form a square pyramid. Four ligands, Cys35 S, one Cl^- ion, and two oxygen atoms of the carboxylate group from an acetate ion, form the base of the equatorial plane, while one water molecule acts

as the fifth ligand to form the top vertex of the pyramid. In the same region of chain C, the seven-ligand coordination no longer exists. Instead, Cd_{C1} has a six-ligand coordination and Cd_{C2} has a five-ligand coordination to form an octahedral and a square pyramidal structure, respectively (figure 4-9 b(ii)). In the six-ligand coordination, all the ligands that form the vertices are identical to that of seven-ligand coordination of Cd_{B1}, with the exception of Asp33. Its carboxyl side chain is oriented perpendicular to the equatorial plane such that one oxygen atom (Glu40 $O^{\varepsilon 1}$) coordinates Cd_{C1} and the other oxygen atom (Glu40 $O^{\varepsilon 2}$) coordinates Cd_{C2}. Because of the bridging coordination Asp33, a slightly distorted octahedral arrangement is formed. In the coordination of Cd_{C2}, Glu40 $O^{\varepsilon 2}$ forms the axial ligand of the square pyramid, while Cys35 S, one water molecule, and two carbonyl atoms of a glycerol molecule form the four vertices of the equatorial plane of the pyramid.

The coordination of EFII is less complicated than that of EFI. It appears to be identical throughout all four chains, so only EFII of chain A is shown on figure 4-9 (c). Cd_{A3} adopts the typical seven-ligand pentagonal bipyramidal coordination with ligands from five conserved residues: Asp65 (residue 1), Asp67 (residue 3), Ser69 (residue 5), Thr71 (residue7), and Glu76 (residue12). Cd_{A4} is coordinated by six ligands that form an octahedral coordination. Asp75 $O^{\varepsilon 1}$ and $O^{\varepsilon 2}$ and two water molecules are located at the four vertices of the equatorial plane, while Asp73$O^{\delta 2}$ and the third water molecule are the axial ligands located at the top and the bottom of the pyramid. Interestingly, Asp73 and Asp75 have never been

involved in any ion coordination in homolog TnCs; thus, these two residues are novel binding ligands found only in our human N-cTnC structure.

(a) EF binding loop I of chain A and chain D

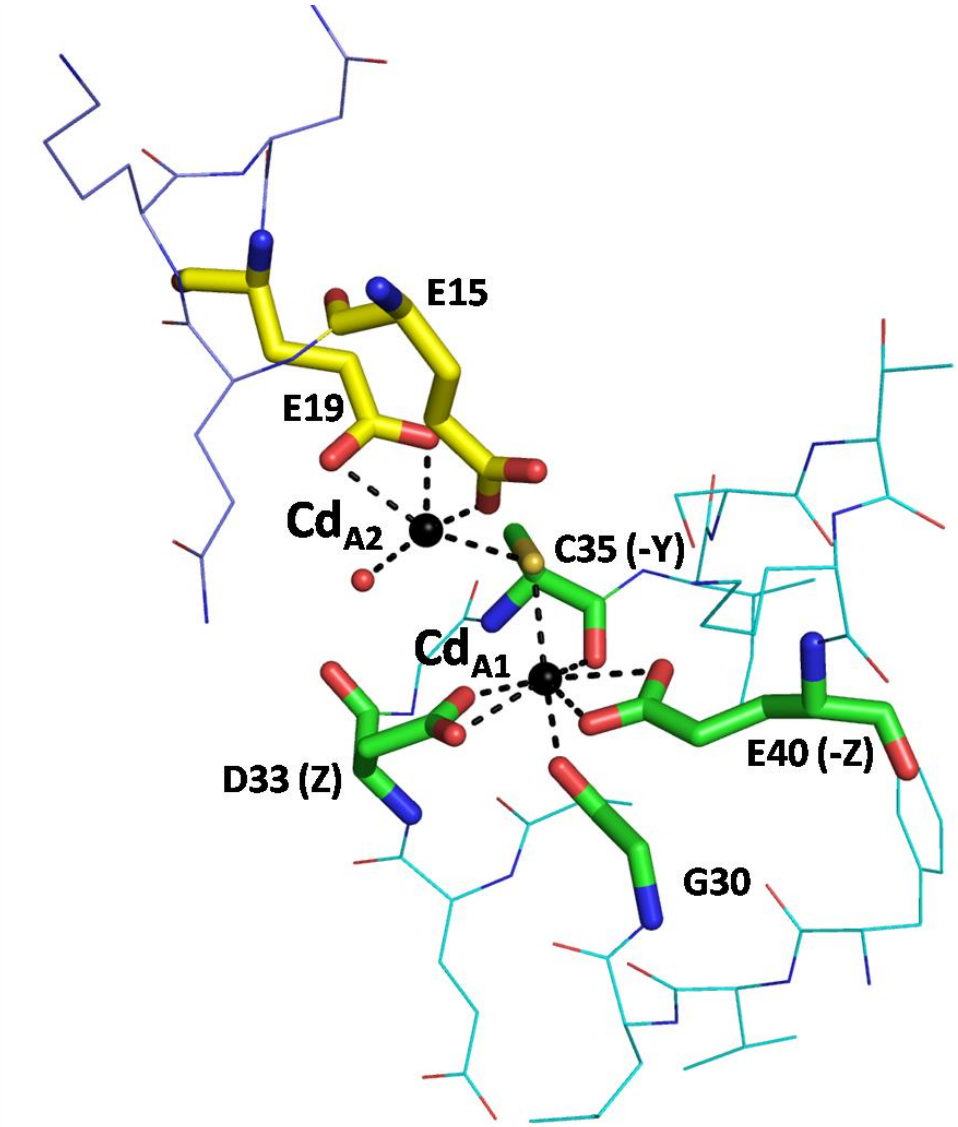

(b) Binding loop I of (i) chain B and (ii) chain C

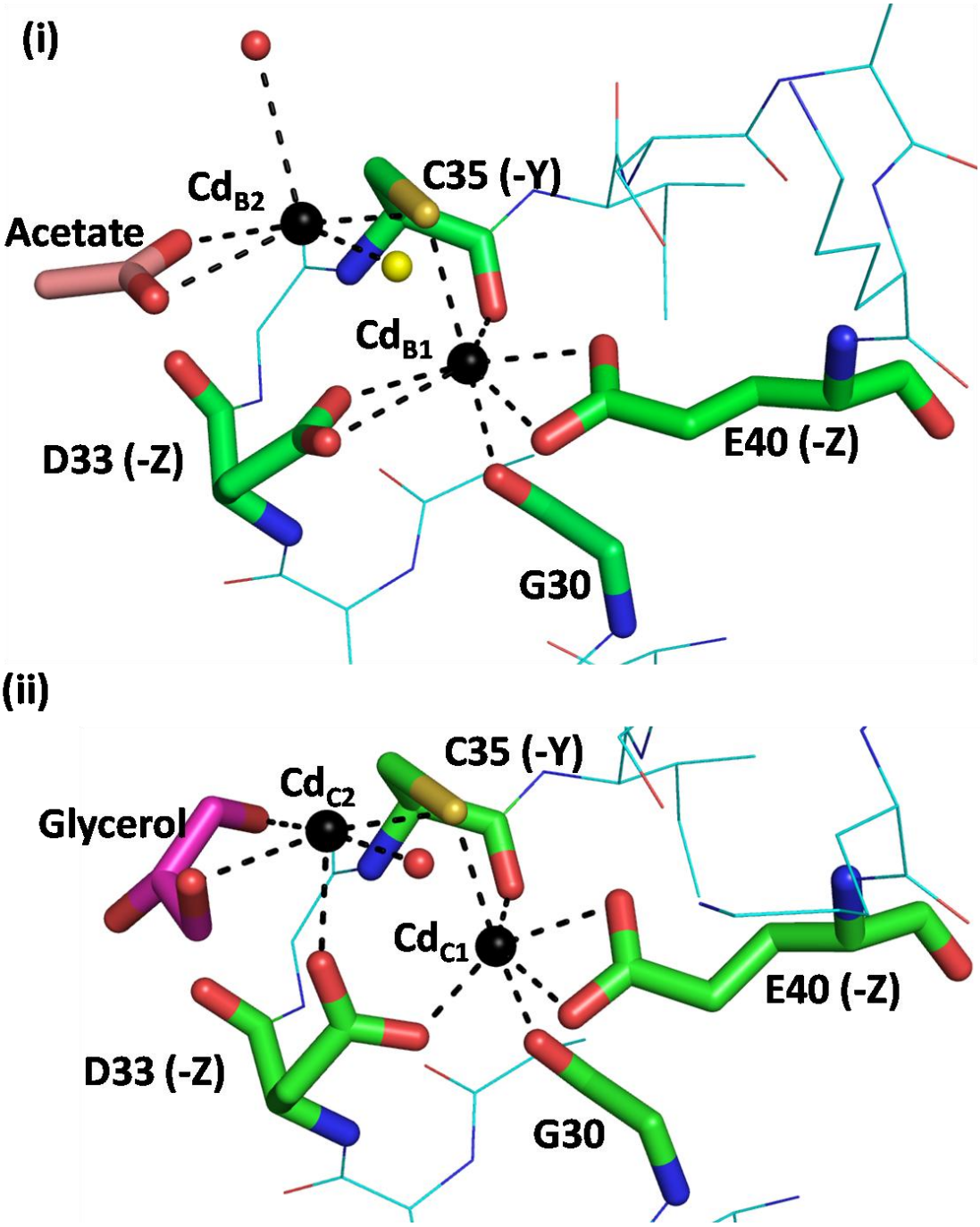

(c) Binding loop II of chain A

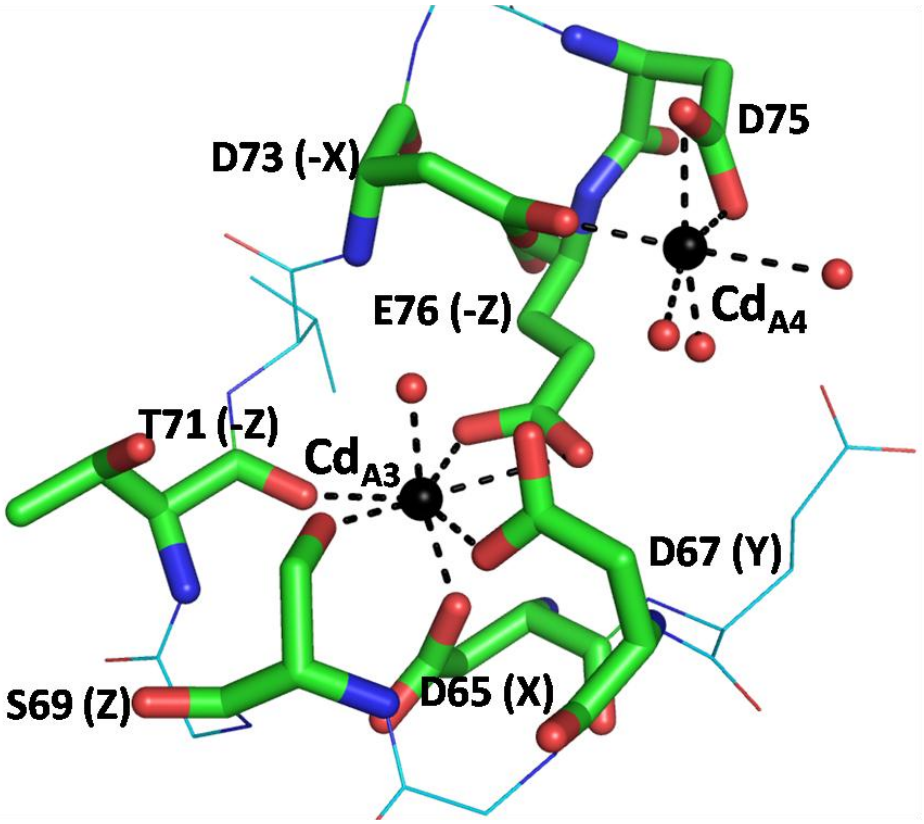

Figure 4-9: Cd^{2+} coordination in (a) EFI of chain A, (b-i) EFI of chain B, (b-ii) EFI of chain C, and (c) EFII of chain A.

The residues that are directly involved in the coordination are labelled and coloured in green, and remaining residues in EF-handing binding loops are represented as cyan lines. Oxygen atoms are coloured red, nitrogen atoms are coloured blue, water molecules are coloured red, chlorine ions are shown as yellow spheres, and cadmium ions are shown as larger black spheres. (a) Cd^{2+} coordination in the EFI of chain A. Cd_{A1} is coordinated by the conserved residues in EFI, whereas Cd_{A2} is coordinated by Cys35 of chain A and Glu13 and Glu15 from a symmetry-related chain A. Because this coordination is identical in chain D, only chain A is displayed here. The residues involved in the coordination from symmetry-related molecule are coloured yellow, while the rest of the residues are coloured in blue. b) Cd^{2+} coordination in the EFI of chain B (i) and chain C (ii). Both Cd_{B1} and Cd_{C1} are coordinated by the conserved residues in EFI. The coordination of Cd_{B2} and Cd_{D2} are mediated by an acetate ion and a glycerol molecule, respectively. (c) Two Cd^{2+} coordination in EFII. Only chain A is displayed here as all four chains have identical coordination. Cd_{A3} is coordinated by the conserved residues in EFII, while Cd_{A4} is coordinated by Asp73 and Asp75 which have never shown to participate in ion coordination in homologous structures. The figures were generated using PyMol (DeLano 2002).

Table 4-3: Cadmium-ligand distance in the binding loop of N-cTnC.

Chain A			**Chain B**		
Cd ID	**Ligand**	**Distance(Å)**	**Cd ID**	**Ligand**	**Distance(Å)**
Cd_{A1}	Gly30 O Asp33 $O^{\delta1}$ Asp33 $O^{\delta2}$ Cys35 S Cys35 O Glu40 $O^{\varepsilon1}$ Glu40 $O^{\varepsilon2}$	2.4 1.9 2.5 2.5 2.6 2.4 2.6	Cd_{B1}	Gly30 O Asp33 $O^{\delta1}$ Asp33 $O^{\delta2}$ Cys35 S Cys35 O Glu40 $O^{\varepsilon1}$ Glu40 $O^{\varepsilon2}$	2.4 2.7 2.9 2.7 2.5 2.4 2.4
Cd_{A2}	*Glu15 $O^{\varepsilon1}$/A* *Glu19 $O^{\varepsilon1}$/A* *Glu19 $O^{\varepsilon2}$/A* Cys35 S Wat57	2.3 2.5 2.2 2.6 2.1	Cd_{B2}	Cys35S $Cl^{-}4$ Act O^{1} Act O^{2} Wat95	2.5 2.8 2.5 2.6 3.2
Cd_{A3}	Asp65 $O^{\delta2}$ Asp67 $O^{\delta1}$ Ser69 O^{γ} Thr71 O Glu76 $O^{\varepsilon1}$ Glu76 $O^{\varepsilon2}$ Wat68	2.1 2.3 2.1 2.5 2.2 2.8 2.1	Cd_{B3}	Asp65 $O^{\delta1}$ Asp67 $O^{\delta1}$ Ser69 O^{γ} Thr71 O Glu76 $O^{\varepsilon1}$ Wat67	2.1 2.4 2.2 2.6 2.1 2.6
Cd_{A4}	Asp73 $O^{\delta2}$ Asp75 $O^{\varepsilon1}$ Asp75 $O^{\varepsilon2}$ Wat66 Wat86 Wat105	2.0 2.4 2.6 2.7 2.6 1.9	Cd_{B4}	Asp73 $O^{\delta2}$ Asp75 $O^{\delta1}$ Asp75 $O^{\delta2}$ Wat62 Wat63 Wat181	2.1 2.0 2.8 2.2 2.5 1.8
Chain C			**Chain D**		
Cd ID	**Ligand**	**Distance(Å)**	**Cd ID**	**Ligand**	**Distance(Å)**
Cd_{C1}	Gly30 O Asp33 $O^{\delta1}$ Asp33 $O^{\delta2}$ Cys35 S Cys35 O Glu40 $O^{\varepsilon1}$	2.2 2.8 2.7 2.6 2.3 2.5	Cd_{D1}	Gly30 O Asp33 $O^{\delta1}$ Asp33 $O^{\delta2}$ Cys35 S Cys35 O Glu40 $O^{\varepsilon1}$	2.1 1.8 2.6 2.3 2.6 2.5

	Glu40 $O^{\varepsilon 2}$	2.3		Glu40 $O^{\varepsilon 2}$	2.4
Cd_{C2}	Cys35S Asp33 $O^{\delta 2}$ Wat71 Gol O^{1} Gol O^{2}	2.6 3.1 2.7 2.7 3.0	Cd_{D2}	Glu15 $O^{\varepsilon 2}$ *Glu19 $O^{\varepsilon 1}$/D* *Glu19 $O^{\varepsilon 2}$/D* Cys35 S Wat145	2.6 2.5 2.1 2.6 2.1
Cd_{C3}	Asp65 $O^{\delta 2}$ Asp67 $O^{\delta 1}$ Ser69 O^{γ} Thr71 O Glu76 $O^{\varepsilon 1}$ Glu76 $O^{\varepsilon 2}$ Wat160	1.9 2.3 2.3 2.5 2.8 2.1 2.4	Cd_{D3}	Asp65 $O^{\delta 2}$ Asp67 $O^{\delta 1}$ Ser69 O^{γ} Thr71 O Glu76 $O^{\varepsilon 1}$ Glu76 $O^{\varepsilon 2}$ Wat119	2.0 2.5 2.6 2.3 2.3 2.5
Cd_{C4}	Asp73 $O^{\delta 1}$ Asp75 $O^{\varepsilon 1}$ Asp75 $O^{\varepsilon 2}$ $Cl^{-}8$ Wat116 Wat211	2.2 2.3 2.5 2.5 2.4 2.6	Cd_{D4}	Asp73 $O^{\delta 2}$ Asp75 $O^{\varepsilon 1}$ Asp75 $O^{\varepsilon 2}$ Wat176 Wat156	2.0 2.6 2.7 2.2 2.5

Aside from the Cd^{2+} binding site in EFI and EFII, there are two additional Cd^{2+} ions that are coordinated by side chains not involved in the binding loop. Table 4-3 shows the coordination of the additional two Cd^{2+} ions. Because there are 16 Cd^{2+} involved in EFI and EFII, the two additional Cd^{2+} ions are named Cd_{17} (figure 4-10 (a)) and Cd_{18} (figure 4-10 (b)). Cd_{17} is located at the interface formed by helix A of chain B and helix A of chain C. It is coordinated by six ligands located at the distorted equatorial plane, including Glu32 $O^{\varepsilon 1}$ and $O^{\varepsilon 2}$ of chain B, Glu15 $O^{\varepsilon 1}$ of chain C, and a water ligand. A Cl^{-} atom is located at the vertex of the axial plane. As the location of Cd_{17} coordination suggests, it plays an important role of mediating a crystal contact between the two dimers in the

asymmetric unit. Cd_{18} is located at the interface formed by chain B and its symmetry-related chain A. It has a seven-ligand coordination and adopts a distorted pentagonal bipyramid arrangement. The ligands located at the distorted equatorial plane include Glu59 $O^{\varepsilon 1}$ and $O^{\varepsilon 2}$ of chain B, one water molecule, and the carboxylate group from a symmetry related deoxycholic acid associated with chain A. Two water molecules form the top and the bottom vertices of the axial plane. As a result, Cd_{18} plays an important role of bringing the symmetry-related molecules together to form the tight packing of the chains.

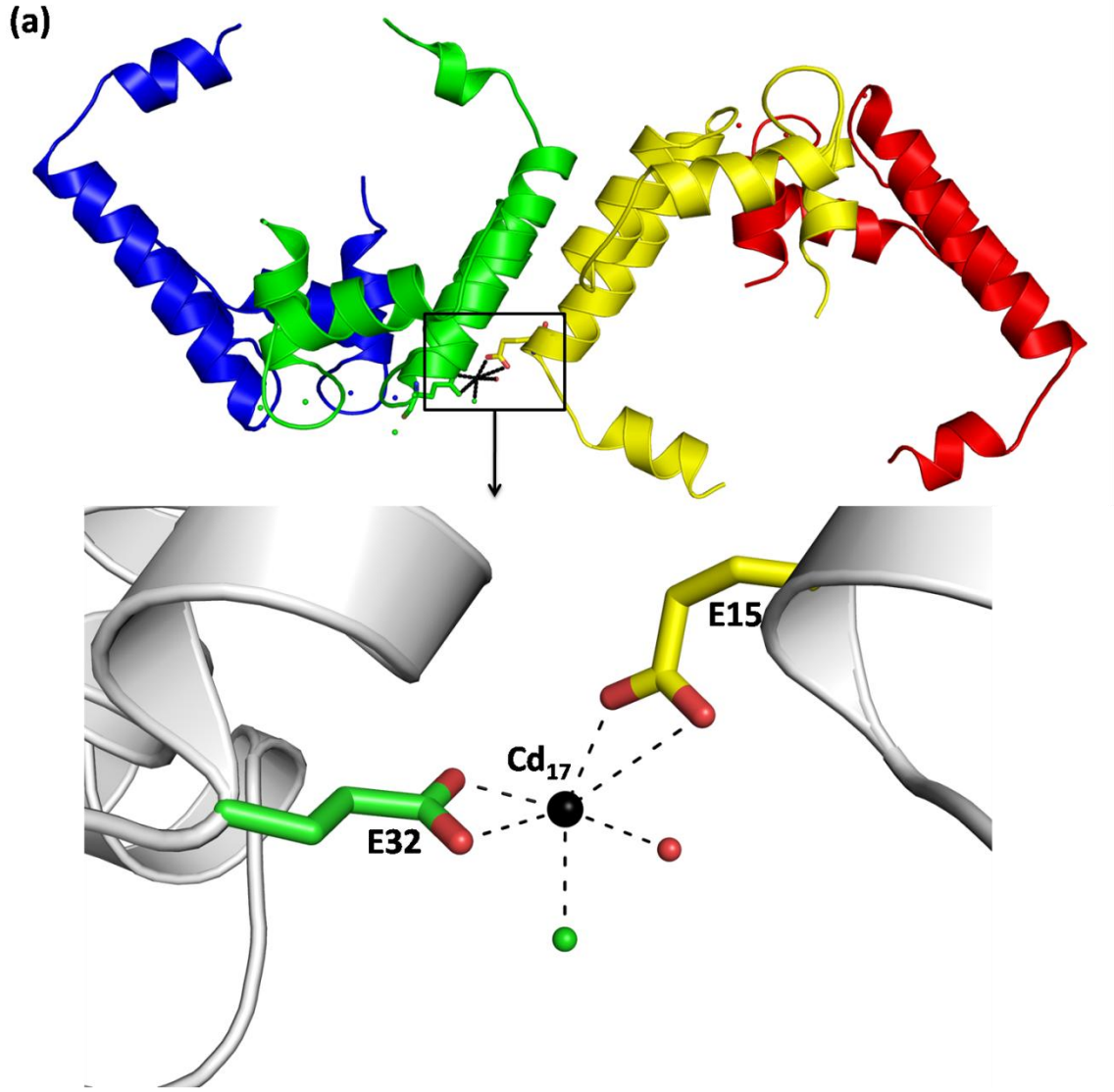
(a)
E15
Cd17
E32

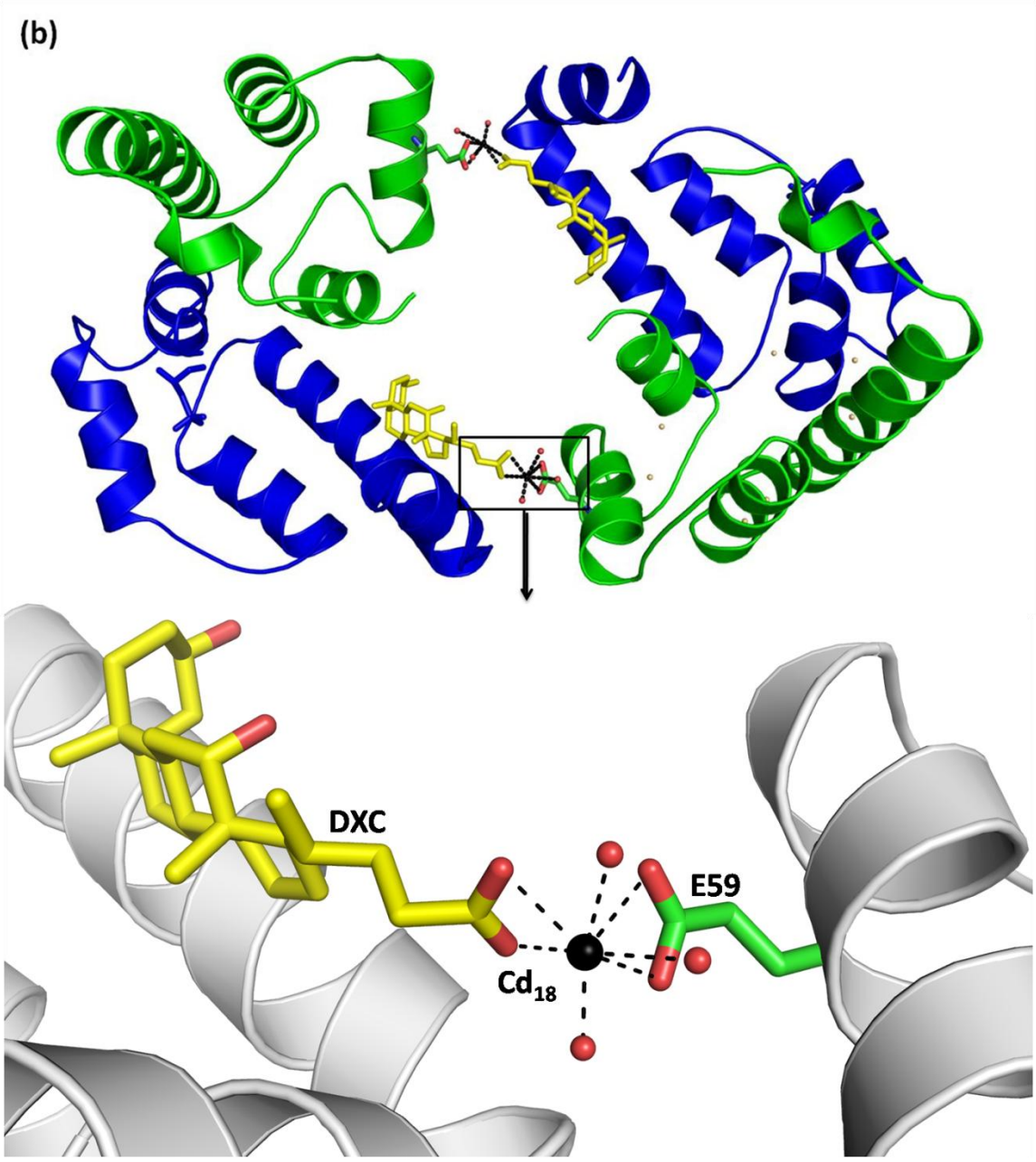
(b)
DXC
E59
Cd18

Figure 4-10: The ion coordination of (a) Cd_{17} and (b) Cd_{18} outside the EF-hand binding loop.

(a) The coordination of Cd_{17}. The coordination is enlarged as shown. It is coordinated by Glu32 of chain B (green) and Glu 15 of chain C (yellow). Its coorindation between chains suggests that it helps to stablize the dimer interface. (b) The coordination of Cd_{18}. It is coordinated by Glu59 of chain B and a DXC molecule bound with chain A from a symmetry-related molecule. Its coordination between symmetry-related molecules suggests that Cd_{18} mediates the crystal packing between symmetry-related molecules. The figures were generated using PyMol (DeLana 2002).

Table 4-4: Ion coordination of Cd_{17} and Cd_{18} with side chains not involved in the binding loop.

Cd_{17}		**Cd_{18}**	
Ligand	**Distance (Å)**	**Ligand**	**Distance (Å)**
Glu32 $O^{\varepsilon 1}$/B	3.0	Glu59 $O^{\varepsilon 1}$/B	2.5
Glu32 $O^{\varepsilon 2}$/B	2.3	Glu59 $O^{\varepsilon 2}$/B	2.7
Glu15 $O^{\varepsilon 1}$/C	2.4	Wat151	1.9
Cl^- 3	2.6	Wat152	2.9
Wat155	2.8	Wat153	2.4
		DXC_{A2} O3	2.4
		DXC_{A2} O4	2.5

a. Deoxycholic acid (DXC) is from a symmetry-related molecule, and it contains a carboxylate group that acts as a bidentate ligand to coordinate the Cd_{18}.

Many forms of Cd^{2+} coordination are observed within the EF-hand binding loops and at the interface of the dimers. The five-, six-, and seven-ligand coordination forms the square pyramidal or the trigonal bipyramidal, octahedral, and pentagonal bipyramidal coordination with Cd^{2+} ion, respectively. The ligands

can be backbone carbonyl oxygen atoms, oxygen-containing side chains, carbonyl group from an acetate ion, a chlorine ion, a glycerol molecule, a deoxycholic acid molecule, and a water molecule that is exposed to a solvent channel. This complex network of Cd^{2+} coordination within the binding loop and at the interface of the dimers has an important role in maintaining the structural integrity of the intra- and inter-chains of our human N-cTnC structure.

4.4 The deoxycholic acid binding pocket on N-cTnC

Deoxycholic acid (DXC), also known as deoxycholate, is referred to as a "secondary bile acid" in nature (figure 4-11). It is produced from cholic acid in the intestine and used to increase the volume of the bile produced from the liver (Neugebauer 1990). Less than half of DXC is absorbed by the intestine and is returned to the liver where it is conjugated and released into the gall bladder (Neugebauer 1990). It was historically used as an intermediate for the synthesis of adrenocortical hormones, such as cortisone, to have an anti-inflammatory effect (Chen 2002). It can also be used as a biological detergent to lyse cells and solubilise membrane components (Neugebauer 1990).

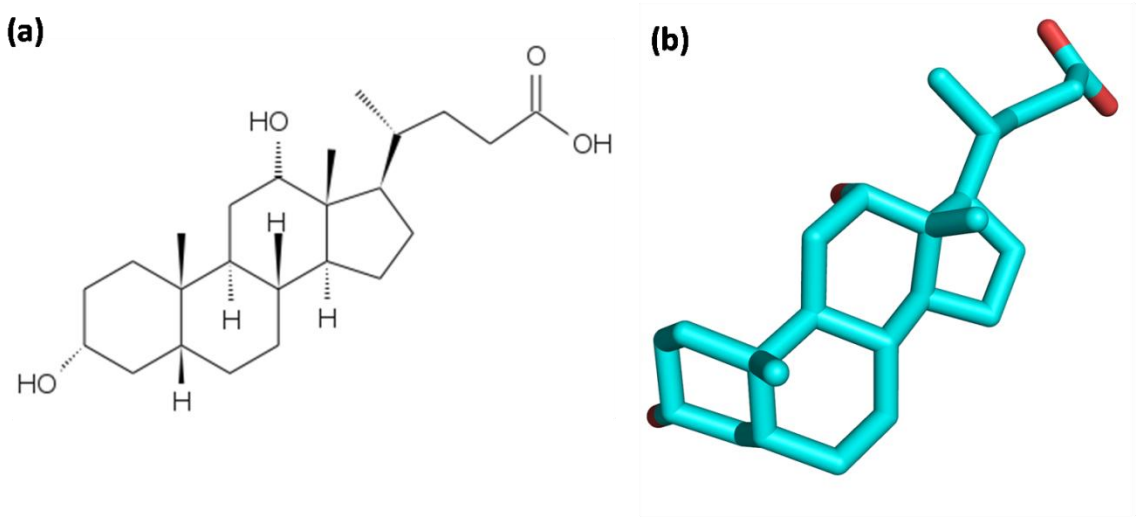

Figure 4-11: The chemical structure of deoxycholic acid.

(a) The 2D chemical structure of DXC. It was drawn by GChemPaint (Brefort 2001). (b) The stick representation of DXC. The oxygen atom is coloured red. The figure was generated by PyMol (DeLano 2002).

DXC was originally used as an additive in the crystallization in an attempt to obtain a crystal form that was free of twinning. Not only did it change the crystal form, but it also binds to the protein, particularly in the Phe-rich environment of the central hydrophobic cavity (figure 4-12).

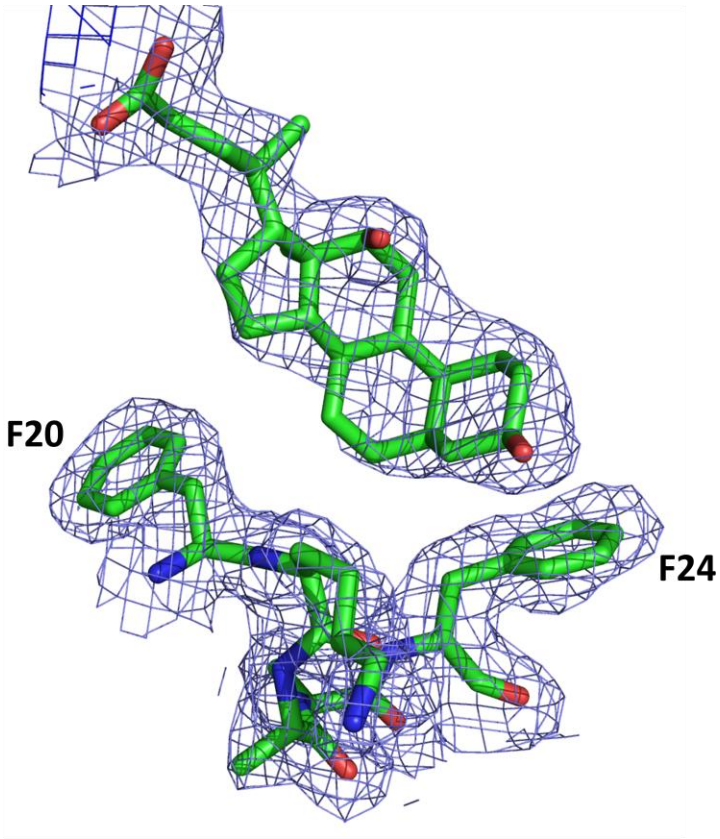

Figure 4-12: The DXC binding in the Phe-rich environment of N-cTnC protein chain.

This shows an example of how DXC binds in the central hydrophobic cavity.

There are two DXC molecules that bind to each chain. One is found at the central hydrophobic cavity, while the other is located at the small hydrophobic groove formed by helix N and helix A. The average surface area of the binding pocket of each chain is around 400 $Å^2$. In each chain, the DXC that is located at the central hydrophobic cavity is named DXC_{A1}, DXC_{B1}, DXC_{C1}, and DXC_{D1}. The second DXC that is bound in between helix N and helix A is named DXC_{A2}, DXC_{B2}, DXC_{C2}, and DXC_{D2} (figure 4-13 and figure 4-14). The second DXC binding is observed throughout all four chains at the approximately the same

location. However, the first DXC that is bound within in the central hydrophobic cavity is variable between different chains. Because chain A and D are equivalent, their DXC binding locations are almost identical. Although chain B and C are equivalent, some difference between DXC_{B2} and DXC_{C2} is observed. Their location within the central hydrophobic cavity is also different from that of chain A and D.

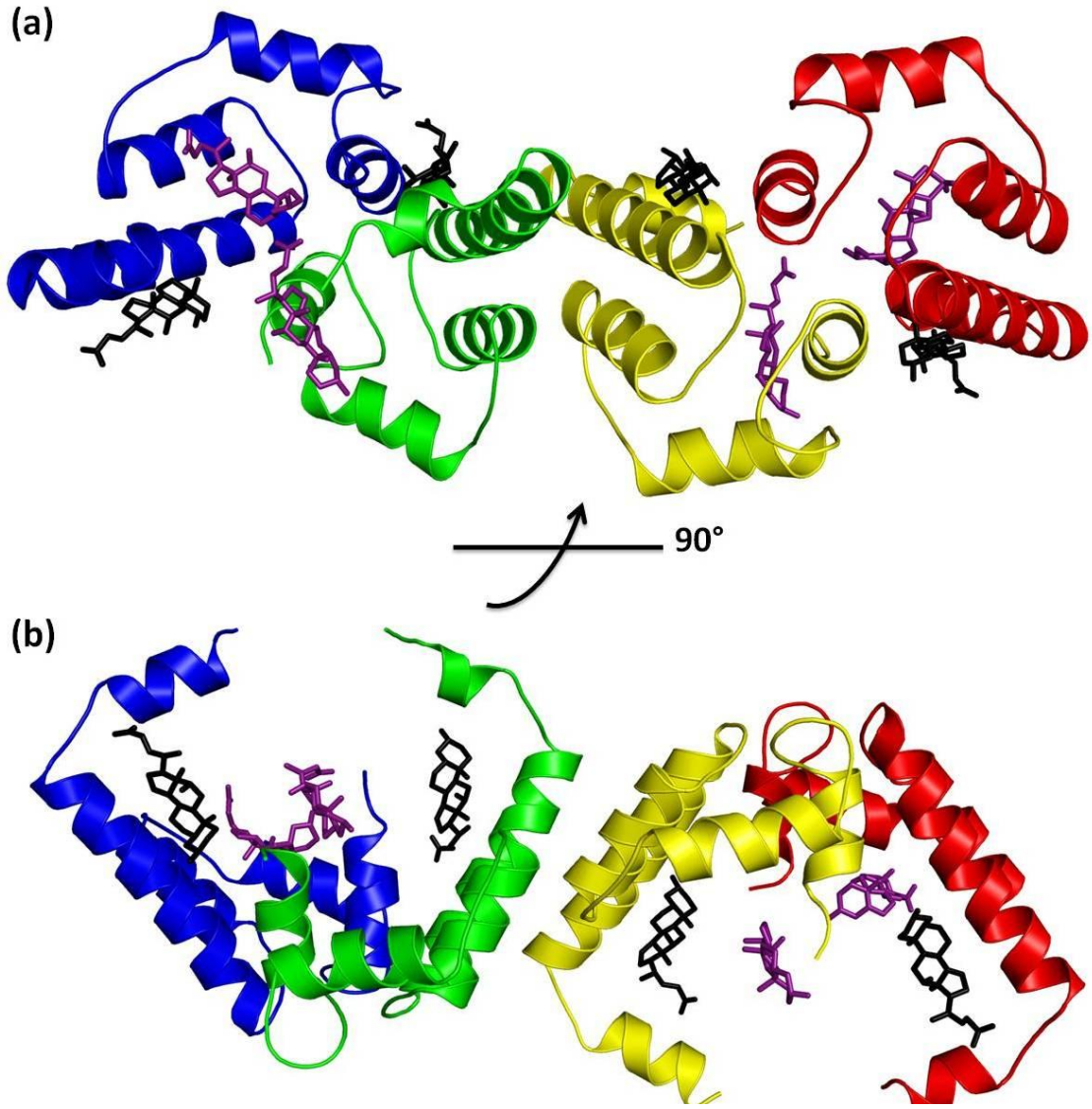

Figure 4-13: The binding site of deoxycholic acid (DXC) in four N-cTnC protein chains from (a) the top view and (b) the side view.

Each protein chain (Chain A, blue; chain B, green; chain C, yellow; chain D, red) has 2 DXC molecules bound. The DXC molecules bound in the central hydrophobic cavity are shown in dark purple, and the ones located between helix N and helix A are shown in black.

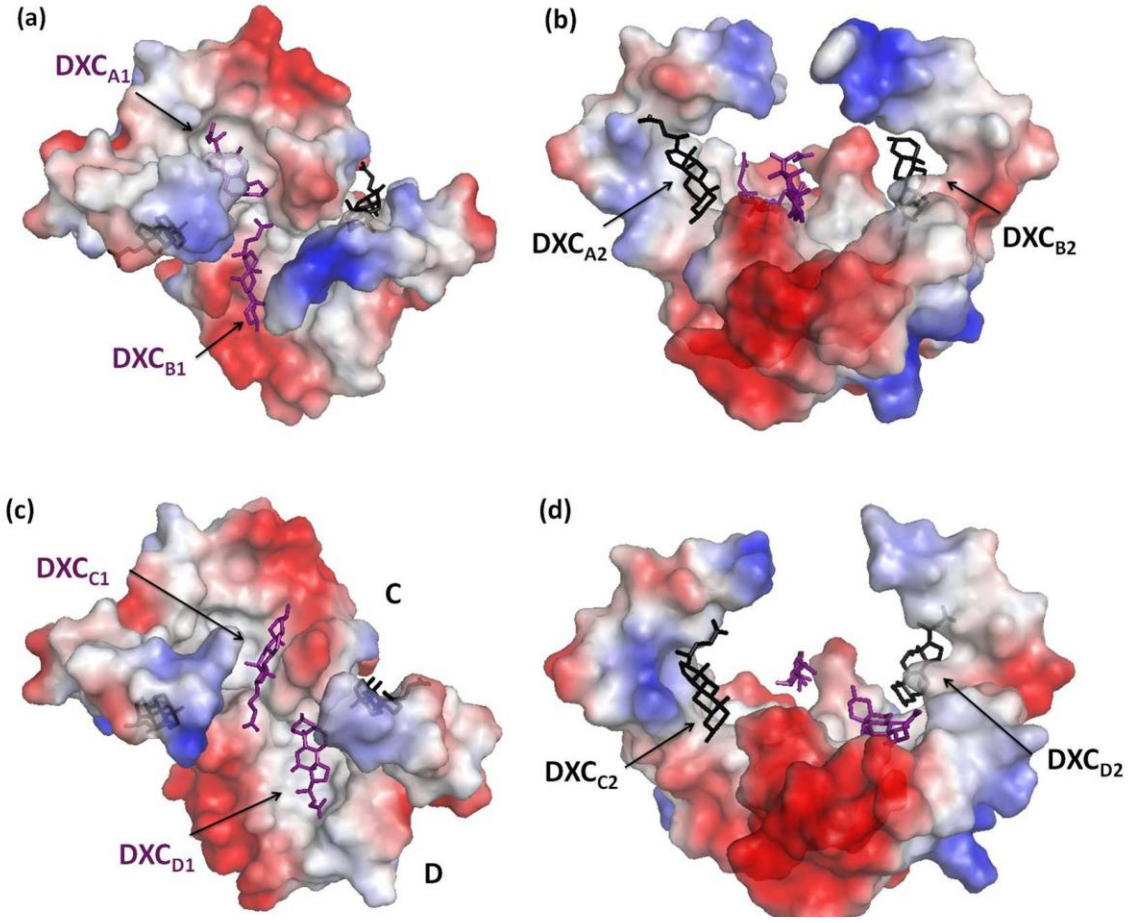

Figure 4-14: The DXC binding site on the surface of (a) (b) AB dimer and (c) (d) CD dimer.

The DXC binding site on the electrostatic surface of N-cTnC (white: neutral; blue: positive; red: negative). (a) The top view of the AB dimer shows the binding site for DXC_{A1} and DXC_{B1}. They are located in the central hydrophobic cavity. (b) The side view of the AB dimer shows the binding location of DXC_{A2} and DXC_{B2} , which is in between helix N and helix A. It has a role in stabilizing the helix conformation. (c) The top view of the CD dimer that shows the binding location of DXC_{C1} DXC_{D1}, which is located at the central hydrophobic cavity. (d) The side view of the CD dimer that shows that binding location of DXC_{C2} and DXC_{D2}. DXC_{A1}, DXC_{B1}, DXC_{C1}, and DXC_{D1} are bound in the central hydrophobic cavity and shown in dark purple. DXC_{A2}, DXC_{B2}, DXC_{C2}, and DXC_{D2} are bound in between helix N and helix A and are shown in black.

Figure 4-14 (a) and (c) show that both DXC_{A1} and DXC_{D1} are fitted right into the groove of the hydrophobic binding pocket, whereas DXC_{B1} and DXC_{C1} are bound closer to one side of the pocket. Although some electron density is observed in the central region of the hydrophobic pocket in chain B and C, the electron density is not strong enough to model DXC. Despite the slight difference in the binding location, DXC is found in the Phe-rich hydrophobic environment in which ring stacking interactions are observed.

The second DXC molecule located at the groove formed by helix N and helix A is observed throughout all four chains (figure 4-15). The orientation of DXC_{A2} and DXC_{D2} are identical (figure 4-15 (a) and (b)), in which the carboxylate group points to helix N of the protein chain. DXC_{A2} has a H-bonding interaction with Lys17 Nζ of chain A, and its carboxylate group coordinates Cd_{18} with Glu59 $O^{\varepsilon 1}$ and Glu59 $O^{\varepsilon 2}$ of chain B. The similar H-bonding interaction of DXC_{D2} is also observed with Lys17 Nζ of chain D, but instead of coordinating Cd^{2+} ion, it coordinates two Ca^{2+} ions. In contrast, DXC_{B2} and DXC_{C2} have different interactions and orientations from those observed for of DXC_{A2} and DXC_{D2}. DXC_{B2} forms a hydrogen bond with Arg83 $N^{\omega 2}$ of chain A, and its carboxylate group points toward the center of the protein. Conversely, DXC_{C2} has its carboxylate group pointing towards the N-terminal helix, and it has a H-bonding interaction with symmetry-related Tyr5 O^{ω} of chain A.

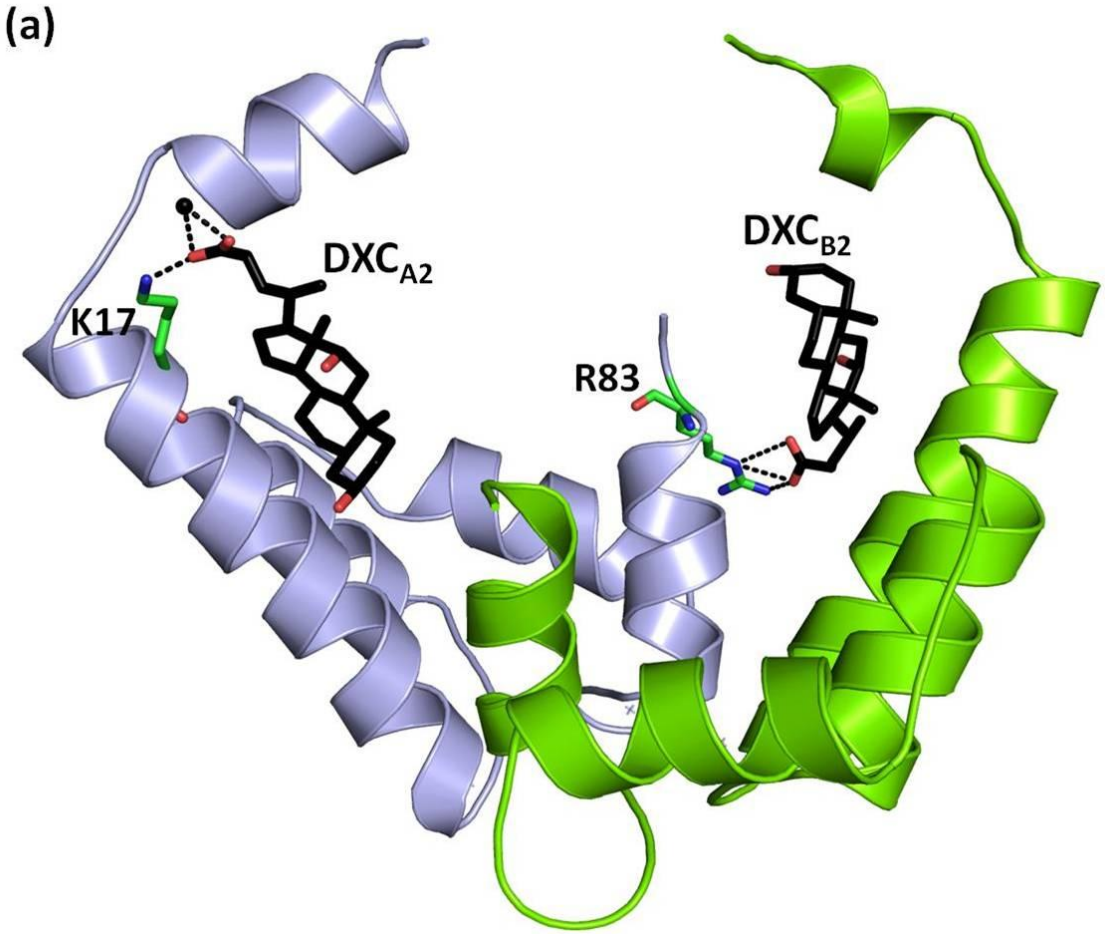
(a)
DXC$_{A2}$
K17
DXC$_{B2}$
R83

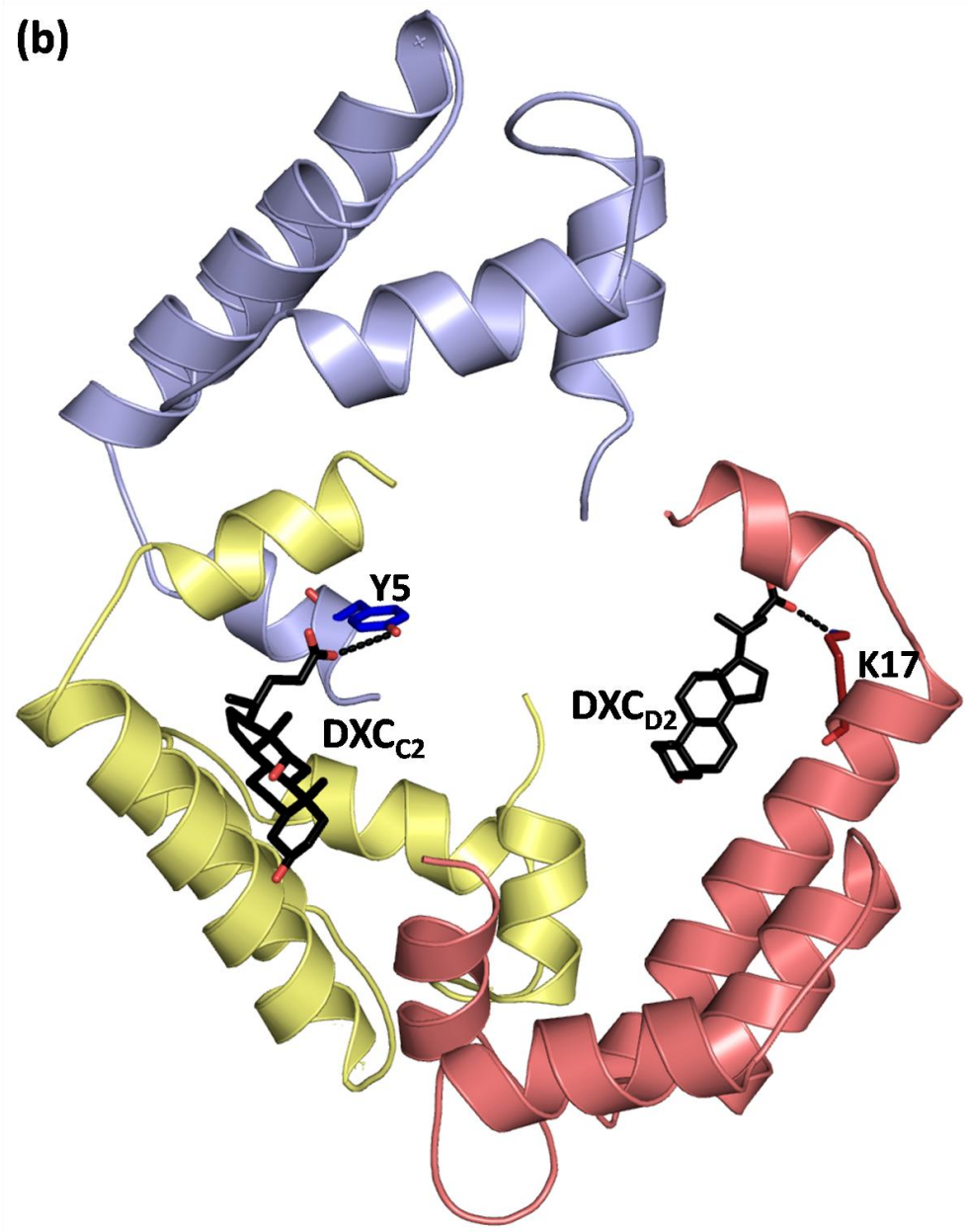

Figure 4-15: The binding location of (a) DXC$_{A2}$ and DXC$_{B2}$, and (b) DXC$_{C2}$ and DXC$_{D2}$.

Chain A is shown in light blue, chain B is shown in light green, chain C is shown in light orange, and chain D is shown in light pink. DXC molecule is shown in black. (a) DXC$_{A2}$ forms a hydrogen bond with Lys17 of chain A. DXC$_{B2}$ has three H-bonding interactions with Arg83 of chain A. (b) DXC$_{C2}$ has a H-bonding interaction with Tyr5 of chain A, while DXC$_{D2}$ forms a hydrogen bond with Lys17 of chain D.

When comparing the drug binding sites in other N-cTnC structures, the DXC binding site in our structure takes on an open conformation due to the shift of helices A and N. Although the hydrophobic cavity appears to be larger and more open, the rest of the cavity is occupied by helices A from a symmetry-related molecule (figure 4-16). The way the dimer AB and symmetry-related dimer CD interact with each other resembles the “holding hands” conformation which stabilizes the open hydrophobic cavity. This also allows the tight packing of the symmetry-related molecules. It should be noted that although N-cTnC chain forms the dimer formation with symmetry-related molecule, it is solely because of the crystal packing interaction. The light scattering analysis shows that N-cTnC exists as a monomer is solution.

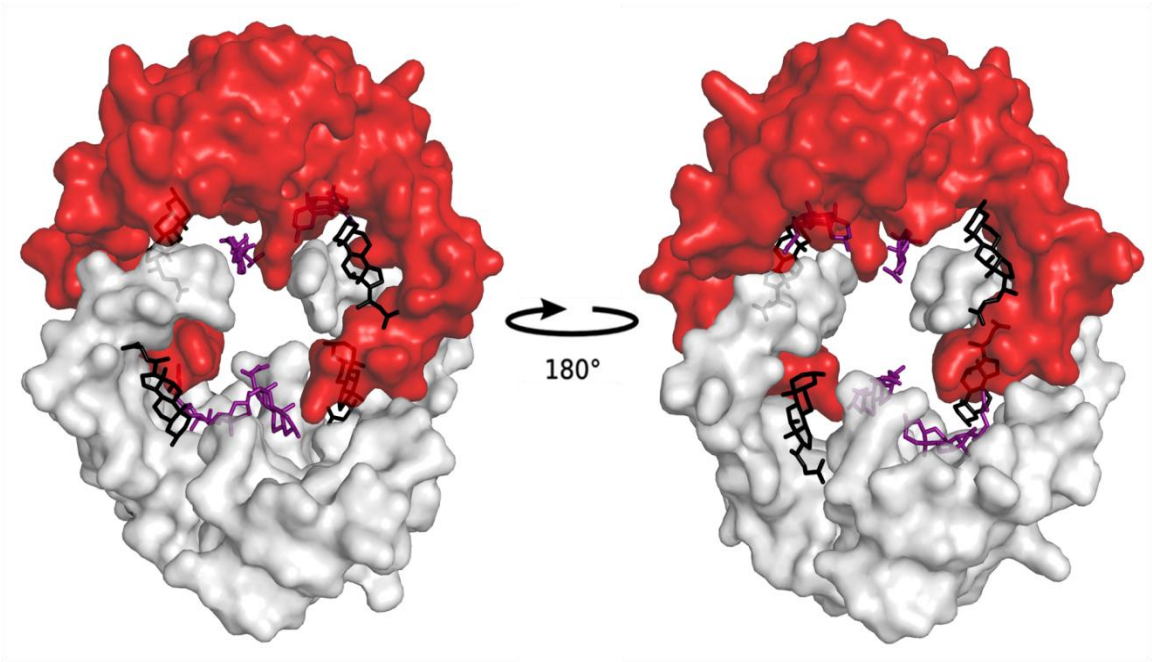

Figure 4-16: The surface representation of dimer AB (white) and symmetry-related dimer CD (red).

The symmetry-related CD dimer (red) fills the open hydrophobic cavity form by AB dimer (white). This allows a close packing of the symmetry-related molecule to stabilize the hydrophobic cavity of each chain.

Each chain has two DXC molecules, one is located in the hydrophobic binding pocket, and the other is located in between helix N and helix A. Together the eight DXC molecules stabilize the terminal helices as well as the hydrophobic binding pocket of N-cTnC. Although the pocket is very open when compared to the other N-cTnC structures, the pace is filled with the extended helix A from the symmetry-related molecules. This network of interaction and packing with symmetry-related molecules contribute to the overall structural integrity of the protein chains. Interestingly, structure of DXC has similar properties to those of known Ca^{2+} sensitizers such as TFP, EMD 57033, and levosimendan (discussed in section 1.6.1). They each have at least two hydrophobic rings and a hydrophilic head group (figure 4-17). Homologous structures containing these drugs show that the hydrophobic rings bind to the hydrophobic pocket within TnC, and the hydrophilic head group is often exposed to the solvent.

Deoxycholic acid

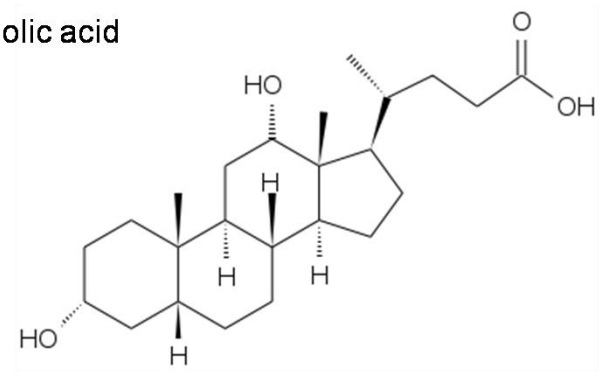

levosimendan

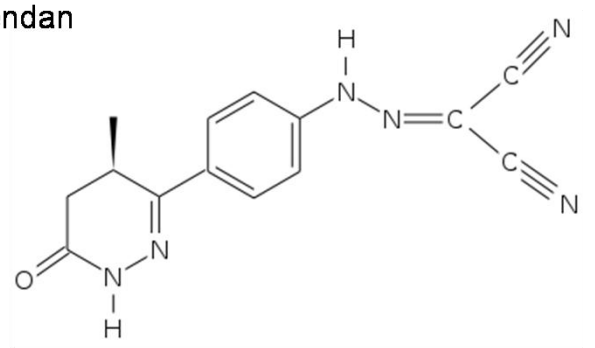

Trifluoperazine

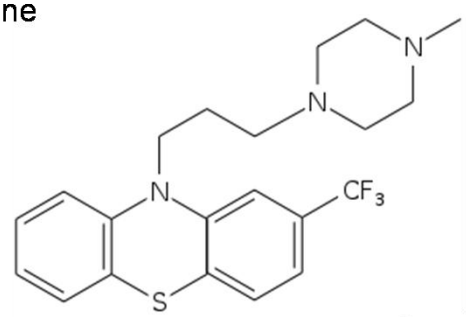

EMD57033

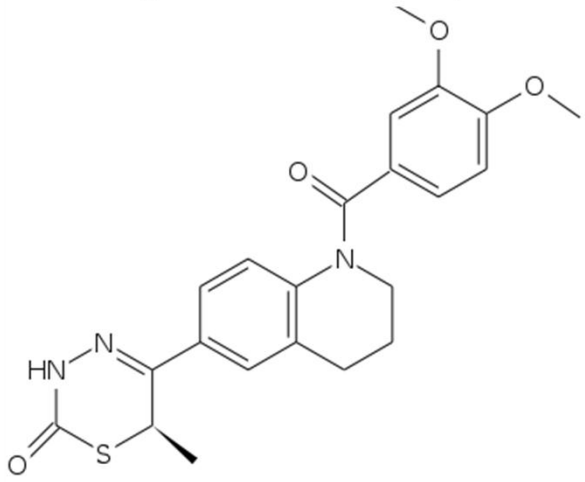

Figure 4-17: Structural comparison of DXC to other Ca2+-sensitizer drugs: levosimendan, TFP, and EMD57033.

The chemical structure of DXC is somewhat similar to the known Ca^{2+}-sensitizer drugs shown. Each contains several hydrophobic rings with a hydrophilic group attached. The figures were generated using GChemPaint (Brefort 2001).

4.5 Comparison with other N-cTnC Structures

To date, there is a total of seven N-cTnC structures solved, and only two of them were solved by X-ray crystallography (PDB: 1WRK and 1WRL). 1WRK and 1WRL are the human N-cTnC constructs with the two cysteine mutations (C35S, C84S), and the only wild type human N-cTnC without the two cysteine mutations were solved by NMR spectroscopy. The five crystal structures of N-cTnC are complexed either with its binding protein TnI or drugs. Each of the previously-solved crystal structures contain two mutations, C35S and C84S, to prevent disulfide bond formation while maintaining the ability to bind Ca^{2+} (Putkey 1993). Unlike these structures, our human N-cTnC structure is the first crystal structure without the two-cystine mutations, and it shows some major structural differences particularly at the N-terminal region. This section discusses and compares our human N-cTnC structure with other human structures, including the NMR structure of Ca^{2+}-free (PDB: 1SPY; (Spyracopoulos 1997)) and Ca^{2+}-bound N-cTnC (PDB: 1AP4;(Spyracopoulos 1997)), the crystal structure of drug-bound N-cTnC (PDB: 1WRK and 1WRL; (Takeda 2006)), TnI

peptide bound N-cTnC within the TnC complex (PDB: 1J1D: (Takeda 2003)), and the NMR structure of both peptide and drug bound N-cTnC (PDB: 1LXF; (Wang 2002)). All four chains of our human N-cTnC structure were resolved but chain A is used for comparison due to its clearest electron density.

Despite 100% sequence identity between the NMR structure of Ca^{2+}-free and the Ca^{2+}-bound N-cTnC structures, the overall conformation of our structure contains some significant structural differences. Our structure superimposed with Ca^{2+}-free N-TnC (PDB: 1SPY) over 76 atoms and the Ca^{2+}-bound (PDB: 1AP4) form over 77 atoms with r.m.s.d values of 11.8 Å and of 8.2 Å, respectively. The most profound difference lies within the N-terminal helix and helix A. The length of the terminal N-helix of our structure is approximately the same as that of 1AP4 and 1SPY (residue 1-11), but the length of helix A (residue 14-33) is six residues longer than helix A in each of 1AP4 and 1SPY (residue 14-27). In addition to the extended length of helix A, its orientation with respect to the rest of the protein is also very different. It is situated much closer to helix B, having an almost 90° shift from the location of helix A in each of 1AP4 and 1SPY (figure 4-18 (a) and (b)). This large shift of helix A is caused by the two-Cd^{2+}-coordination in the EFI region, which is normally dysfunctional in the homologous structures. As mentioned earlier, the B-factor of this region is the lowest and the ion coordination is the strongest when compared with the remainder of the structure. In addition, deoxycholic acid has a stabilizing effect between the N-terminal helix and helix A. Because of the two-Cd-coordination and binding of deoxycholic acid, the overall

structure is not a globular conformation; instead, it has an elongated conformation with helix A extending out of the protein.

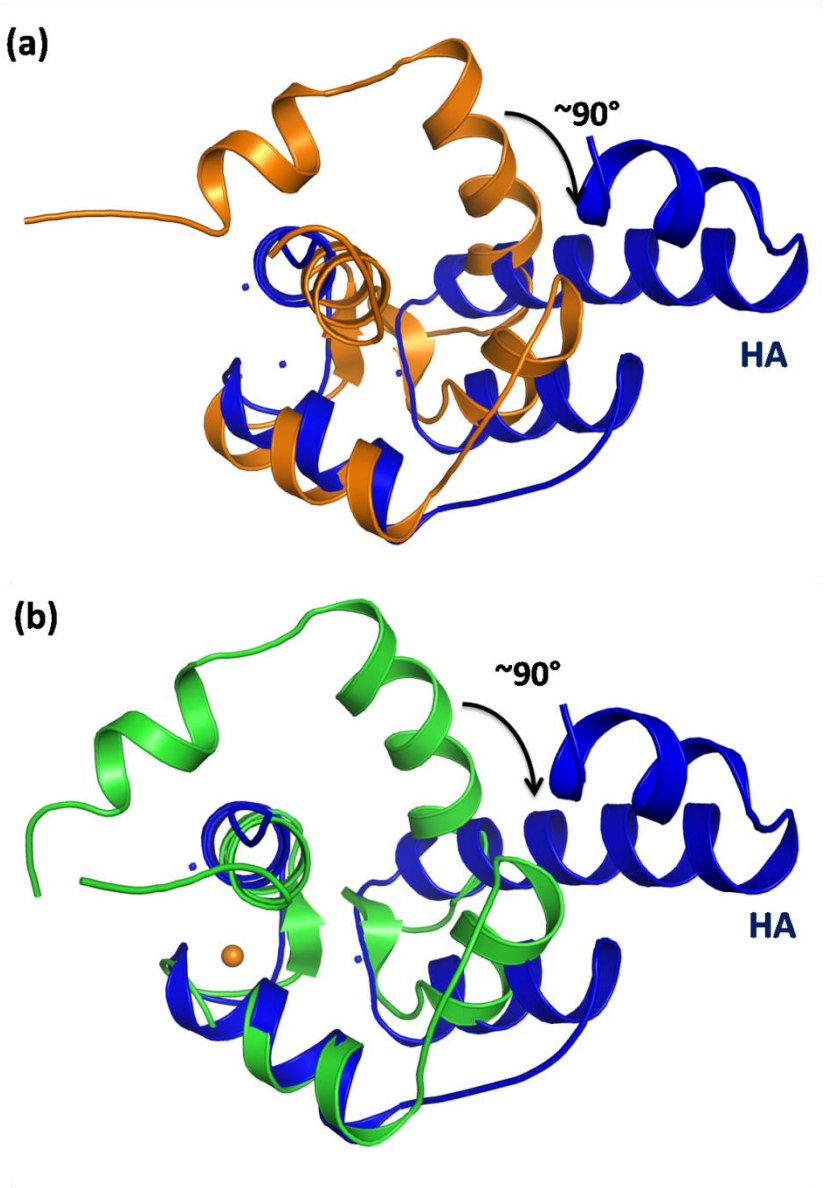

Figure 4-18: The superimposition of our crystal structure of human N-cTnC on the NMR structures of (a) Ca^{2+} free N-cTnC (PDB: 1SPY) and (b) Ca^{2+}-bound N-cTnC (PDB: 1AP4).

Our human N-cTnC structure is shown in blue, 1AP4 is shown in green, and 1SPY is shown in orange. Each of the superimposed structures shows that the position of helix A is significantly different from the homologous structures. It is shifted approximately 90° from its original position.

The most closely related structure is the crystal structure of human N-cTnC bound to the Ca^{2+} sensitizer drug TFP (figure 4-19). This construct produces two crystal forms, in which one belongs to an orthorhombic $P2_12_12_1$ form (PDB: 1WRK), and the other belongs to a monoclinic $P2_1$ form (PDB: 1WRL). 1WRK and 1WRLboth form a dimer in the crystal structure. See table 4-4 for a comparison of crystal statistics.

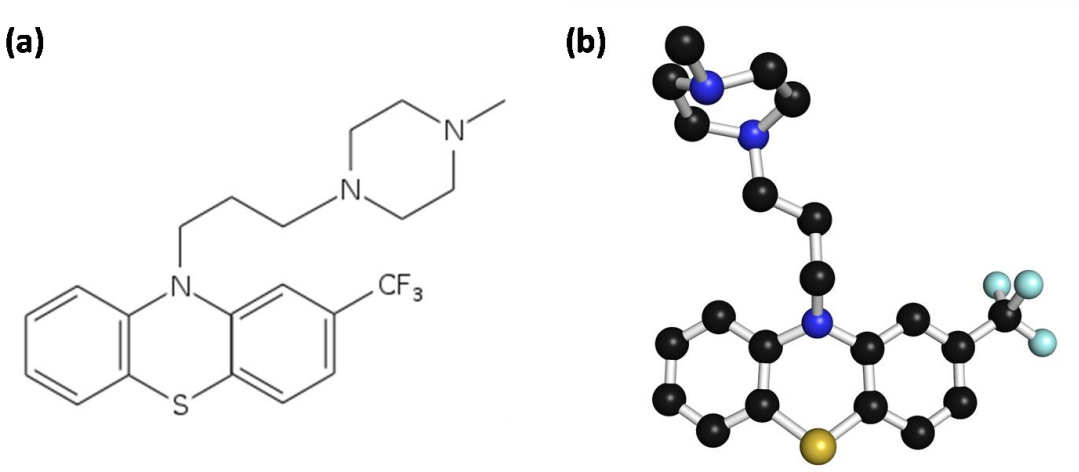

Figure 4-19: The chemical structure of TFP.

(a) The 2D chemical structure of TFP. The figure was drawn using GChemPaint (Brefort 2001) (b) The ball and stick representation of TFP (carbon: black; nitrogen: blue; sulphur: yellow; fluoride: cyan). The figure was generated using PyMol (DeLano 2002).

Table 4-5: Comparison of our human N-cTnC to 1WRK and 1WRL.

	Human N-cTnC	**1WRK**	**1WRL**
Construct	Native human wild type N-cTnC	Human N-cTnC with two mutations: C35S and C84S	Human N-cTnC with two mutations: C35S and C84S
Unit cell	Orthorhombic	Orthorhombic	Monoclinic
Space group	$P2_12_12$	$P2_12_12_1$	$P2_1$
Unit cell dimension Length: a, b, c (Å) Angle: α, β, γ (°)	 51.84 × 81.78 ×100.74 90.0, 90.0, 90.0	 40.33 × 47.90 × 98.64 90.0, 90.0, 90.0	 48.93 × 67.46 × 90.28 90.00, 96.75, 90.00
Resolution (Å)	2.20	2.15	2.60
Ligand	Deoxycholic acid	Trifluoperazine	Trifluoperazine
Oligomeric state	Dimeric	Dimeric	Dimeric
Number of molecules in the asymmetric unit	4	2	6

When comparing a single chain of our human N-cTnC structure with a single chain of 1WRK, the two structures superimposed with a Cα r.m.s.d of 8.5 Å over 76 atoms despite having 97% sequence identity. Excluding helix A from the superimposition, helix B, C, and D from the two structures superimposed with a Cα r.m.s.d of 2.3 Å over 46 atoms. The 90° degree shift of extended helix A is still apparent (figure 4-20), and the drug binding site is somewhat different (figure 4-21). In each 1WRK monomer, the globular conformation creates a closed hydrophobic binding cavity with 2 TFP molecules bound. In the dimeric form of

1WRK, the interface forms a closed binding pocket for a total of 4 bound TFP molecules (figure 4-21 (a)). Although our N-cTnC has a larger hydrophobic binding area, only 1 DXC molecule is found within the hydrophobic cavity. The rest of the pocket is filled with the extended helix A from a symmetry-related molecule. The second DXC (DXC_{A2} and DXC_{B2} shown on figure 4-21 (b)) is located in the smaller hydrophobic area formed by helix A and the N-terminal helix. In total, four DXC molecules are bound to our human N-cTnC dimer, two DXC are found in the hydrophobic pocket and two are found outside the pocket.

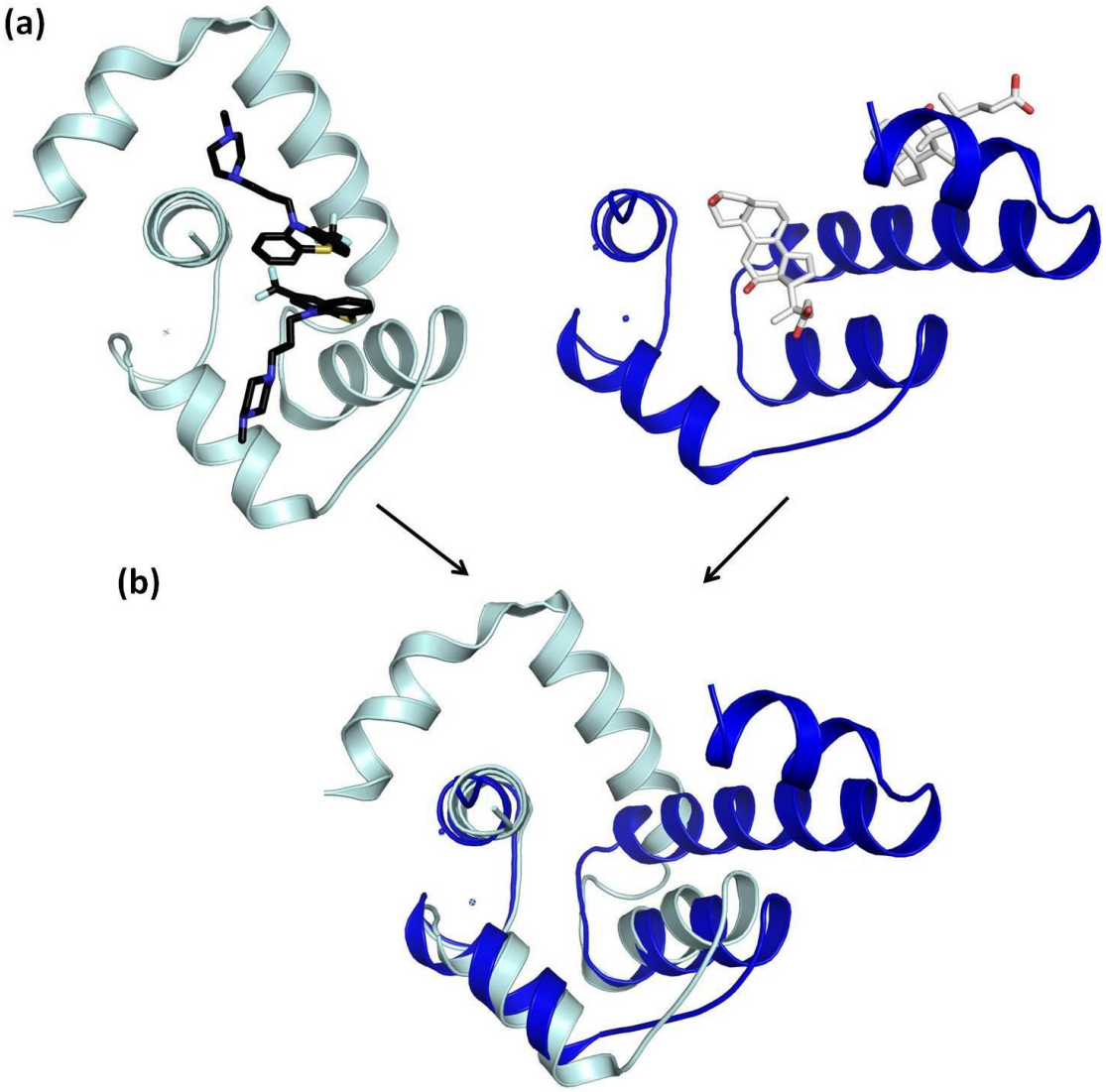
(a)
(b)

Figure 4-20: Comparison of the (a) crystal structure of 1WRK monomer (light cyan) and our human N-cTnC structure (blue) and (b) their superimposed structure.

1WRK is the orthorhombic crystal form of the two cystine mutant construct of human N-cTnC complexed with TFP. It forms a dimer in the crystal structure, but only a single chain is shown in this figure. The DXC molecule is shown in white, and the TFP molecule is shown in black. The superimposed structure shown in (b) highlights the major difference between helix A of our model and that of 1WRK. The DXC in the central hydrophobic cavity is located approximately where the TFP molecules bound in 1WRK. The ligands are not shown in the superimposed structure.

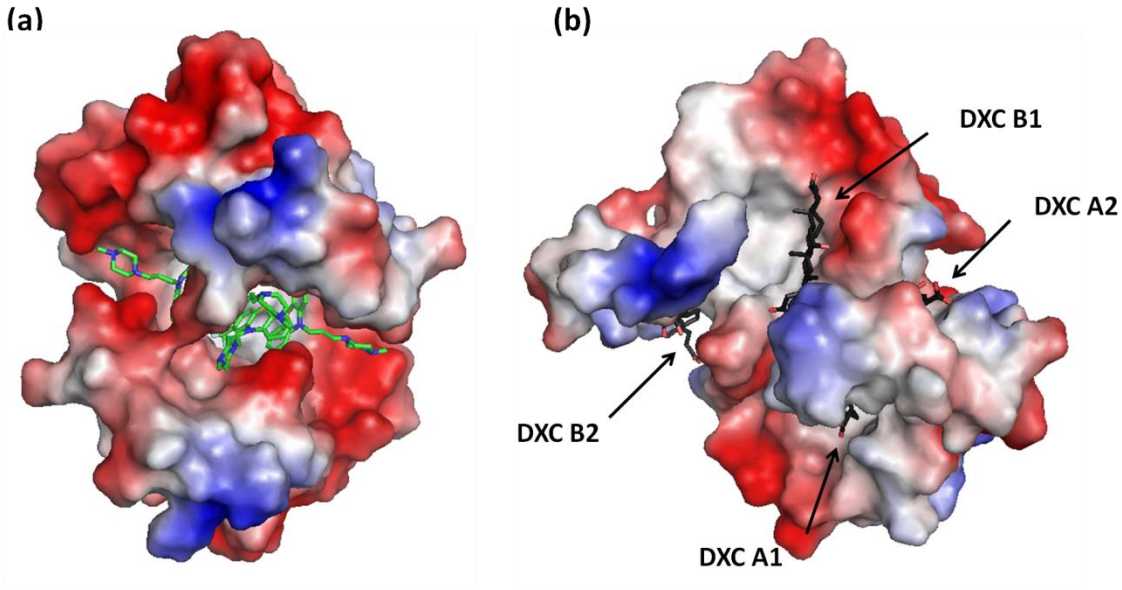

Figure 4-21: The vacuum electrostatic representation of the binding pocket for (a) 1WRK and (b) our N-cTnC structure.

The molecular surface colored by electrostatic potential (a) 1WRK and (b) our human N-cTnC. (white: neutral; blue: positive; red: negative). TFP molecules are coloured in green, and DXC molecules are coloured in black. The two dimers in 1WRK form a tight hydrophobic cavity which provides a binding pocket for 4 TFP molecules. In contrast, the hydrophobic cavity formed by our dimer is more open, and only 2 DXC molecules (DXC_{A1} and DXC_{B1}) are located in the center. The other two DXC molecules (DXC_{A2} and DXC_{B2}) are located outside the cavity and mediating the conformation of helix N and helix A.

When comparing our structure with the monoclinic form of 1WRL, a difference between the helix N and helix A is very noticeable. Figure 4-22 shows that both TFP molecules are bound within the central cavity of 1WRL, similarity to that of 1WRK. When superimposing with our human N-cTnC structure, the orientation of helix A is clearly shown to be very different. Because both 1WRK and 1WRL constructs have the two cystine mutations at C35S and C84S, it makes a profound difference in the ion coordination of EFI. Cys35 of our structure is shown to play a significant role in coordinating two Cd^{2+} ions, making the EFI become functional.

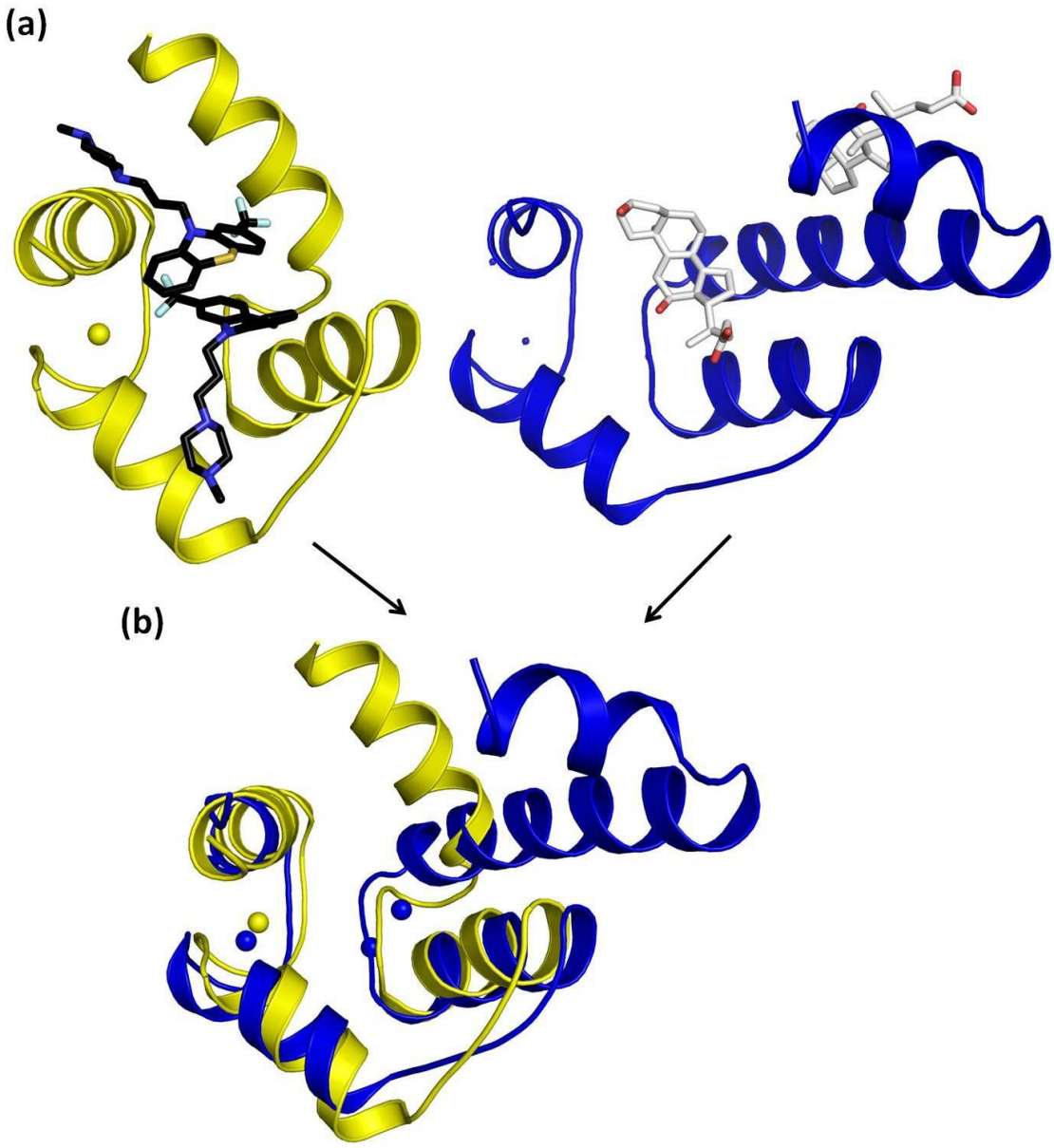

Figure 4-22: Comparison between (a) 1WRL (yellow) and our human N-cTnC structure (blue) and (b) their superimposed structure.

1WRL is the monoclinic crystal form of the same construct used to produce 1WRK. N-cTnC forms a dimer in the 1WRL crystal structure. A single chain is shown in the figure. The difference between helix A in each structure is apparent, and the DXC molecule that binds in the central cavity of our structure is approximately where the two TFP molecules are located in 1WRK.

When N-cTnC is compared with the two cystine-mutant N-cTnC crystal structure (1J1D) within the troponin complex, some structural differences can be observed (figure 4-23). They superimpose with a Cα r.m.s.d of 8.7 Å over 77 atoms. Excluding helix N and helix A (1-33), they superimposed with a Cα r.m.s.d of 2.4 Å over 46 atoms. Like the other superimposed structures, only helix B, helix C, and helix D superimposed approximately at the same location. Interestingly, TnI peptide (145-160) binds with 1J1D at the location where DXC1 and DXC2 appear in our N-cTnC structure.

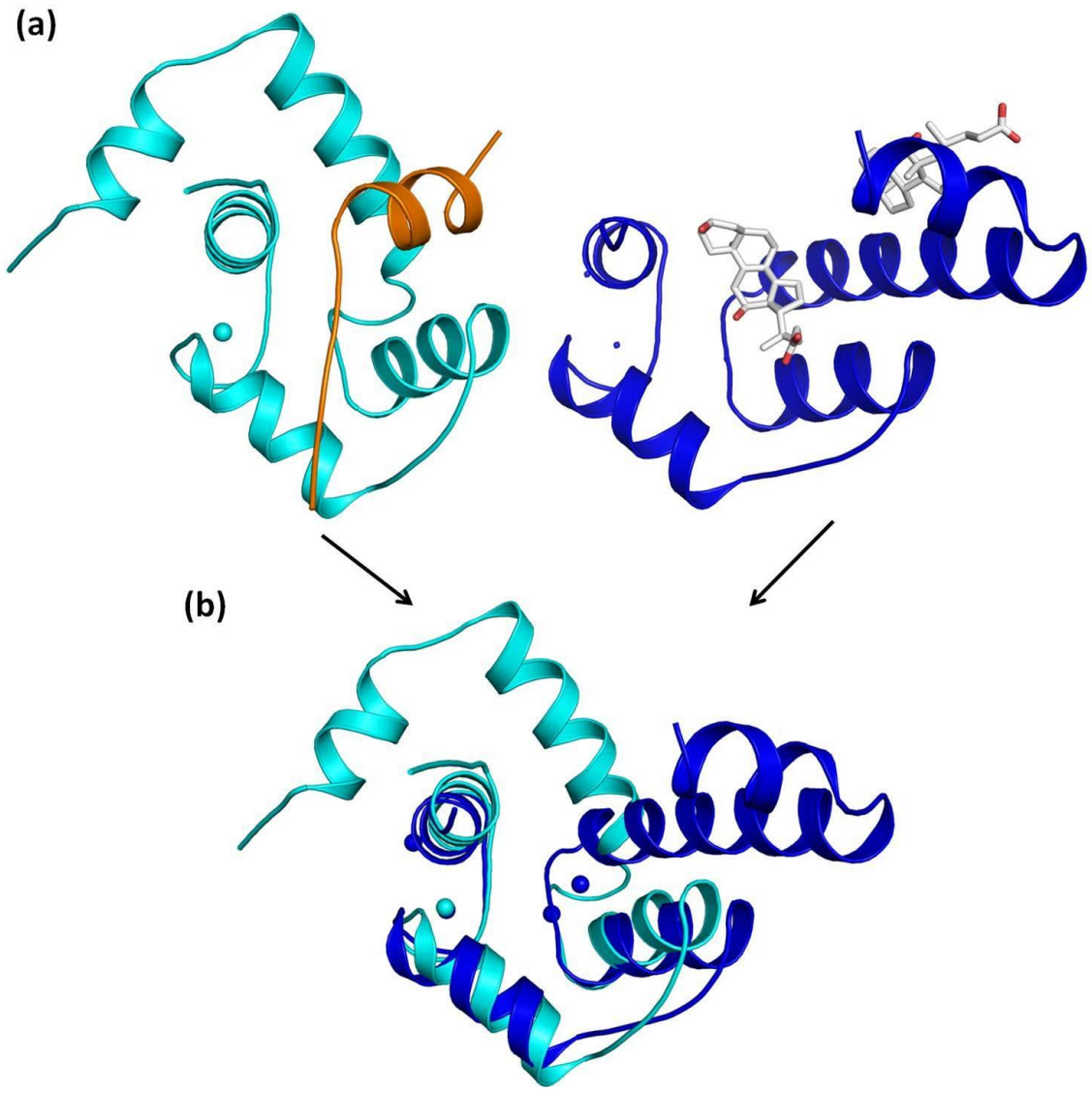

Figure 4-23: Comparison between (a) our human N-cTnC (blue) and homolog N-cTnC (cyan) with TnI peptide (orange) from full troponin complex model (1J1D). (b) Their superimposed structure.

The superimposed structure shows that the TnI peptide in 1J1D is bound where the 2 DXC molecules located in our structure. The superposition does not show the binding of the TnI peptide of 1J1D or DXC from our human N-cTnC structure.

Finally, when comparing our structure with 1LXF, the NMR structure of N-cTnC bound to the TnI peptide (147-163) and a bepridil drug molecule, they superimposed with an overall main chain Cα r.m.s.d of 7.9Å over 77 atoms. Again, the Cα r.m.s.d decreases to 2.0 Å over 46 atoms when helix N and helix A are excluded from the superimposition. Bepridil in LXF binds in the hydrophobic binding pocket that is approximately at the same location of DXC1, and the TnI peptide is bound at the location of DXC2 (figure 4-24).

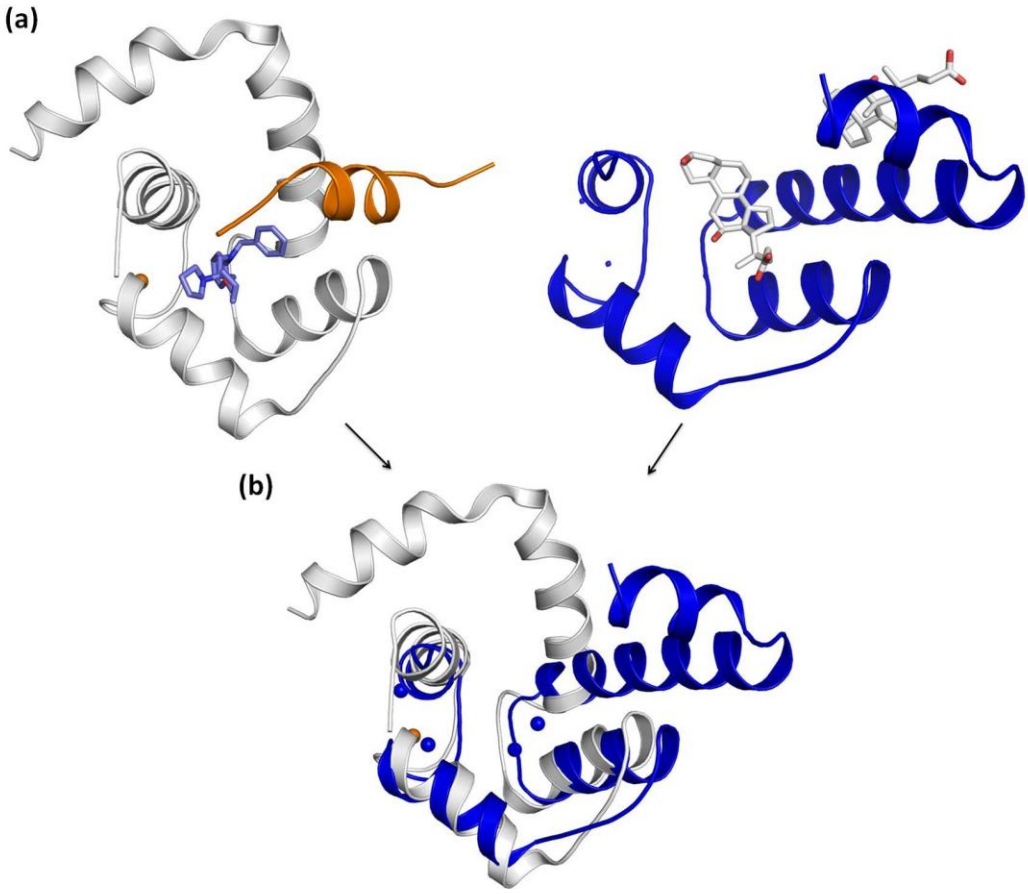

Figure 4-24: Comparison between (a) the NMR structure of N-cTnC (white) in complexed with TnI peptide (orange) and bepridil (blue) (PDB: 1LXF) and our human N-cTnC structure (blue). (b) Their superimposed structure.

Bepridil molecule is shown in blue, and DXC molecule is shown in white. Their superimposed structure shows the large difference of location of helix A. Where bepridil and TnI located in 1LXF is approximately where the two DXC molecules are bound in our structure. Ligand are not shown in the superimposed structure.

Aside from the difference between our N-cTnC structure and other homologous structures, TnC is well known for its extreme flexibility. Despite the similarity of the overall conformation of the previously-mentioned homologous structures, there are many structural differences between them. Figure 4-25 shows the superimposed C-alpha structure among the five homologous human N-cTnC structures used for comparison. When all helix N and helix A are superimposed (figure 4-25 (a)), the significant shift of helix B and the linker region is observed. When each of the C helices are superimposed (figure 4-25 (b)), the large difference at each of the terminal helices can be observed.

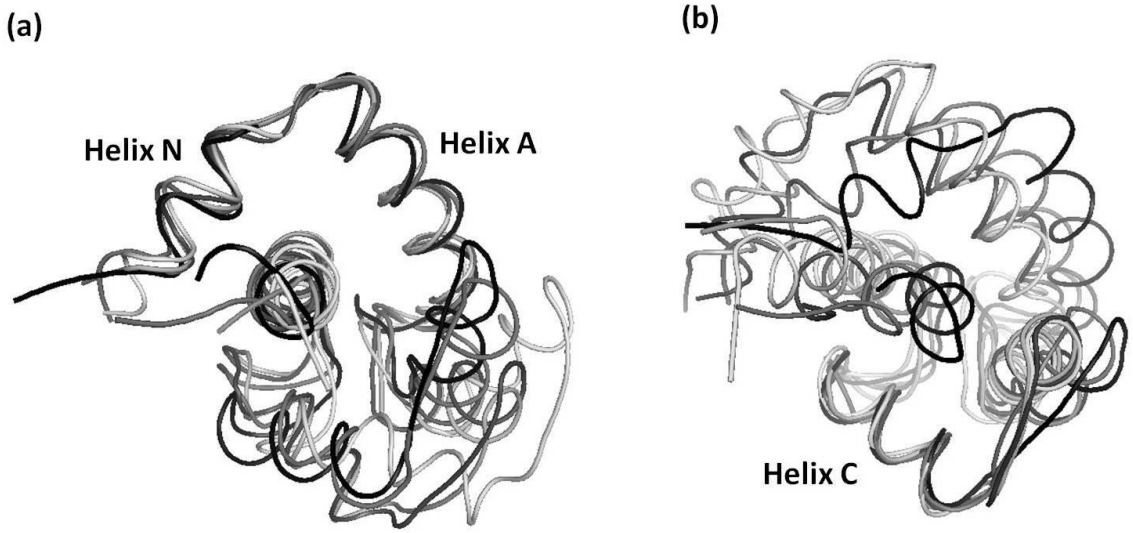

Figure 4-25: The superposition of the six homologous structures used for comparison, with (a) terminal helix N and helix A superimposed and (b) helix C superimposed.

Although the homologous structures adopt a similar overall conformation, their superimposed structure shows a range of helix positions. It demonstrates the flexibility of the N-cTnC protein.

Comparison of our human N-cTnC to other NMR and crystal structures of TnC, in the presence or absence of Ca^{2+}, with TnI peptide or other chemical drugs binding in the N-terminal domain, reveal a range of structural conformations that the N-cTnC protein can adopt. In addition to the flexibility of the N- and C-terminal domains among the homologous structures, our human N-cTnC reveals a novel conformation that is very distinct from the homologous structures (figure 4-26). The most significant difference lies within the length and the position of helix A with respect to the rest of the protein. Helix A of our structure is six-residues longer than the other N-cTnC structures, and because of the two-Cd^{2+}-coordination in EFI, the extended helix A is shifted 90° degrees from helix A of all the other homologous structures. This changes the overall globular conformation of the protein to a more elongated structure, further demonstrating the extreme flexibility of the N-terminal domain of TnC. The phi-psi angles of the residues that involved in the turning point of helix A and the first loop region (residue 28-34) are listed in table 4-6.

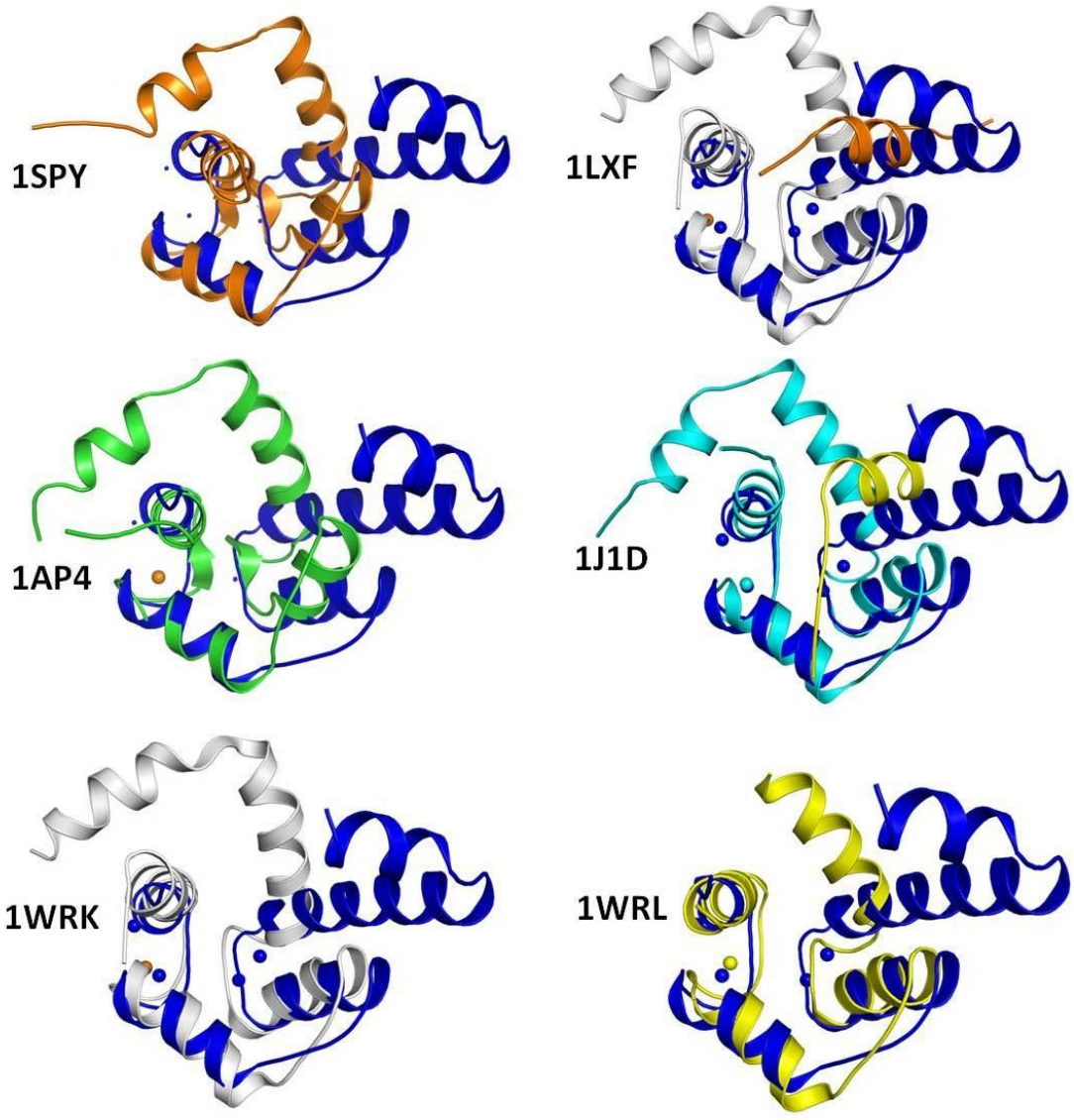
1SPY
1LXF
1AP4
1J1D
1WRK
1WRL

Figure 4-26: Superposition of our human N-cTnC structure (blue) with the other N-cTnC structures.

1SPY: NMR structure of Ca^{2+}-free wild type human N-cTnC; 1AP4: NMR structure of Ca^{2+}-bound human N-cTnC; 1LXF: NMR structure of Ca^{2+}-bound wild type human N-cTnC with TnI peptide (orange; residue 147-163); 1J1D: the crystal structure of mutant human N-cTnC (C35S, C84S) with TnI peptide (yellow; residue 145-160); 1WRK: the crystal structure of mutant human N-cTnC (C35S, C84S); 1WRL: the crystal structure of mutant human N-cTnC (C35S, C84S). The 90° shift of helix A of our human N-cTnC (blue) is observed in all superimposed structures.

Table 4-6: Comparison of the phi-psi angle of residue 28-34 of chain A to that of 1WRK. These residues are located at the turning point of helix A to the EFI.

Residues Number (our human N-cTnC)	Phi (φ) angel	Psi (ψ) angle	Residues Number (two cystine mutant 1WRK)	Phi (φ) angel	Psi (ψ) angle
Val28	-68.6	-41.7	Val28	5.5	-100.2
Leu29	-55.2	-50.5	Leu29	-62.5	115.9
Gly30	-49.5	-35.5	Gly30	103.7	-17.3
Ala31	-82.1	-12.7	Ala31	-67.3	132.9
Glu32	-59.7	-18.5	Glu32	-56.8	-31.1
Asp33	-91.9	-3.3	Asp33	-122.0	24.1
Gly34	98.3	-2.6	Gly34	66.2	12.5

4.6 Conclusion

We solved the first crystal structure of wild type human N-cTnC. The structure reveals several new insights about the protein. First, it is able to coordinate two Cd^{2+} ions in both EF-hand binding loops. In EFI, Cys35 plays an important role of coordinating two Cd^{2+} ions, and this agrees with previous findings in which Cys residues have a high affinity for Cd^{2+} (Dokmanic 2008). In

EFII, not only do the conserved residues provide ligands for ion coordination, but two other residues, Asp73 and Asp75, also provide ligands for the coordination of a second Cd^{2+} ion. Second, because of the two Cd^{2+} coordination in EFI, it brings helix A closer to helix B, making them almost parallel to each other. When comparing the position of helix A of homologous proteins, helix A is found perpendicular to helix B. In our structure, helix A is shifted approximately 90° from the original position. Third, a chemical that was used as an additive to aid crystallization, deoxycholic acid (DXC), was bound to our N-cTnC structure. One DXC is located at the central hydrophobic cavity, and the other is located between helix N and helix A, maintaining the structural integrity of this region. Interestingly, deoxycholic acid has a similar chemical structure to other Ca^{2+}-sensitizing drugs, such as trifluoperazine and levosimendan, which are used for treating troponin-related cardiovascular diseases. These new insights obtained from solving this structure provide valuable information for the use of N-cTnC as a potential target for rational drug design.

APPENDICES

Appendix I: The PDB of crystal and NMR cTnC homolog structure

ID	Descriptor	Method	Date	Source	Temp (K)	pH	R_{factor}	Res	R_{free}
Full length cTnC									
3CTN	Cardiac troponin C in the Ca^{2+}-saturated form	NMR, 30 structures	07/05/1993	*Gallus gallus*	0	0	0	0	0
2JT0	F104W cardiac troponin C	NMR, 10 structures	16/07/2003	*Homo sapiens*	0	0	0	0	0
2JT3	F153W cardiac troponin C	NMR, 10 structures	17/07/2003	*Homo sapiens*	0	0	0	0	0
2JT8	F153-to-5-flurotryptophan mutant of human cardiac troponin C	NMR, 10 structures	19/07/2003	*Homo sapiens*	0	0	0	0	0
TnC complex with TnI									
1FI5	The C-terminal domain of cardiac troponin C bound to the N- terminal domain of cardiac troponin I	NMR, 20 structures	02/08/1996	*Gallus gallus*	0	0	0	0	0
1LXF	The N-terminal domain of human cardiac troponin C in complex with human cardiac troponin-I (147-163) and bepridil	NMR, 30 structures	04/06/1998	*Homo sapiens*	0	0	0	0	0
1SBJ	The C-terminal domain of cardiac troponin C bound to the N-Terminal domain of cardiac Troponin I in the Mg^{2+}-saturated form	NMR, 20 structures	09/02/2000	*Gallus gallus*	0	0	0	0	0

1SCV	The C-terminal domain of cardiac troponin C bound to the N- terminal domain of cardiac troponin I	NMR, 20 structures	11/02/2000	*Gallus gallus*	0	0	0	0	0
1OZS	The C-terminal domain of human cardiac troponin C in complex with the inhibitory region of human cardiac troponin I	NMR, 30 structures	08/04/1999	*Homo sapiens*	0	0	0	0	0
2CTN	Cardiac troponin C in the Ca^{2+}-saturated form	NMR, 30 structures	05/05/1993	*Gallus gallus*	0	0	0	0	0
N-cTnC									
2JXL	The N-terminal domain of troponin C mutant F77W-V82A	NMR, 30 structures	19/11/2003	*Homo sapiens*	0	0	0	0	0
1AP4	The N-terminal domain of human cardiac troponin C in the Ca^{2+}-saturated form	NMR, 40 structures	23/07/1993	*Homo sapiens*	0	0	0	0	0
1R2U	The N-terminal domain of trout cardiac troponin C at 30 C°	NMR, 40 structures	28/09/1999	*Oncorhynchus mykiss*	0	0	0	0	0
1R6P	The N-terminal domain of trout cardiac troponin C at 7 C°	NMR, 40 structures	14/10/1999	*Oncorhynchus mykiss*	0	0	0	0	0
1SPY	The N-terminal domain of human cardiac troponin C in the Ca^{2+}-free form	NMR, 40 structures	13/07/1993	*Homo sapiens*	0	0	0	0	0
cTnC complexed with drug									
ID	**Descriptor**	**Method**	**Date**	**Source**	**Temp (K)**	**pH**	**Rfactor**	**Res**	**Rfree**
1DTL	Cardiac troponin C in complex with Ca^{2+}-sensitizer bepridil in Ca^{2+}-saturated form	X-ray diffraction	11/01/1996	*Gallus gallus*	277	7.2	0.22	2.15	0.28
1WRK	The N-terminal domain of human cardiac troponin C in complex with trifluoperazine (orthorhombic crystal form)	X-ray diffraction	19/10/2000	*Homo sapiens*	277	7.2	0.23	2.15	0.25

1WRL	The N-terminal domain of human cardiac troponin C in complex with trifluoperazine (monoclinic crystal form)	X-ray diffraction	19/10/2000	*Homo sapiens*	277	7.2	0.24	2.6	0.27
Full troponin complex									
1J1D	The 46kDa core domain of human cardiac troponin in the Ca^{2+}-saturated form	X-ray diffraction	02/12/1998	*Homo sapiens*	293	8.0	0.26	2.61	0.30
1J1E	The 52kDa core domain of human cardiac troponin in the Ca^{2+}-saturated form	X-ray diffraction	02/12/1998	*Homo sapiens*	293	8.0	0.25	3.3	0.31

APPENDIX II –The list of N-TnC crystal data collection

Crystal collected at the Macromolecular X-ray Diffraction Data Collection Facility at Simon Fraser University

Protein	**Native WT N-TnC**	**Native WT N-TnC**	**Native WT N-TnC**	**Native L29Q N-TnC**
Data collected	Sept 4, 2007	Jan 16, 2008	Jan 22, 2008	Jan 24, 2008
Dataset name	AL61_B4_a_1	AL92_D3_2_a	AL92_A6_1_a	AL110_C3_1_a
Crystal-to-detector distance (mm)	200.0	150.0	120.0	120.0
Beam center (X, Y)	151.22, 151.15	151.22, 151.15	151.22, 151.15	151.22, 151.15
Crystallization condition	0.05M $CdSO_4$, 1.0M NaOAc, and 0.1M Hepes pH 7.5	0.05M $CdSO_4$, 0.7 M NaOAc, and 0.1M Hepes pH 7.5	0.05M $CdSO_4$, 0.7 M NaOAc, and 0.1M Tris pH 8.0	0.05M $CdSO_4$, 1.0M NaOAc, and 0.1M Hepes pH 7.5, and 1 µl of acyl alcohol
Cryoprotectant solution	Mother liquor + 30% glycerol	Mother liquor + 30% glycerol	Mother liquor + 30% glycerol	Mother liquor + 30% glycerol
Unit cell **space group**	Trigonal/hexagonal P622	C center orthorhombic C222	Trigonal hexagonal P622	Trigonal hexagonal P622
Crystal dimension **A, b, c (Å)** **α, β,γ (°)**	 49.7 × 49.7 × 115.5 90.0, 90.0, 120.0	 49.8 × 86.3 × 117.1 90.0, 90.0, 90.0	 49.8 × 49,8 × 116.9 90.0, 90.0, 120.0	 49.7 × 49.7 × 116.8 90.0, 90.0, 120.0
Maximum resolution (Å)	2.4	2.0	1.8	1.8
# of images collected	360	360	280	360
Notes on reflection images		initial indexing suggested trig/hex was most likely but spot prediction was still good when indexed in monoclinic unit cell	Reflections were visible to 1.9 Å. Little splitting of the spots was observed. However, ice rings were observed in images collected later.	Reflections were very clean and well defined.

Crystals collected at the Macromolecular X-ray Diffraction Data Collection Facility at the University of British Columbia

Protein	**Mutant L29Q N-TnC**	**Mutant NIQD N-TnC**
Data collected	Oct. 11, 2007	Oct. 11, 2007
Dataset name	AL71_C2	AL80_A1
Crystal-to-detector distance (mm)	250.0	250.0
Beam center (X, Y)	172.5, 172.5	172.5, 172.5
Exposure time	--	--
Crystallization condition	0.05M $CdSO_4$, 0.7 M NaOAc, and 0.1M Hepes pH 7.5	0.05M $CdSO_4$, 1.0 M NaOAc, and 0.1M Tris pH 8.0
Cryoprotectant solution	Mother liquor + 30% glycerol	Mother liquor + 30% glycerol
Unit cell **space group**	Trigonal/hexagonal P622	Trigonal/hexagonal P622
Crystal dimension **A, b, c (Å)** **α, β,γ (°)**	 49.4 × 49.4 × 113.8 90.0, 90.0, 120.0	 49.6 × 49.6 × 115.0 90.0, 90.0, 120.0
Maximum resolution (Å)	2.6	3.0
# of images collected	180	180
Notes on reflection images	Data good to 2.6 Å. Spots are clear and separated.	

Crystals collected at the Advance Light Source, Lawrence Berkeley Laboratory, University of California at Berkeley

Protein	**Native apo WT N-TnC**	**Native Ca^{2+} WT N-TnC**	**Native apo WT N-TnC**
Dataset name	NTnC_199_C1	NTnC_201_C6	NTnC_199_A6
Data collected	Mar 29, 2008	Mar 30, 2008	Mar 30, 2008
Crystal-to-detector distance (mm)	270.0	150.0	370.0
Beamline	ALS 8.2.1	ALS 8.2.1	ALS 8.2.1
Beam center (X, Y)	155.1, 157.3	155.1, 157.3	155.1, 157.3
Exposure time	3 sec	10 sec	8 sec
Crystallization condition	0.05M $CdSO_4$, 0.60 M NaOAc, and 0.1 M Tris pH 8.0	0.05M $CdSO_4$, 0.7 M NaOAc, and 0.1M Hepes pH 7.5	0.05M $CdSO_4$, 0.7 M NaOAc, and 0.1M Tris pH 8.0
Cryoprotectant solution	Mother liquor + 30% glycerol	Mother liquor + 30% glycerol	Mother liquor + 30% glycerol
Unit cell **space group**	Orthorhombic $P2_12_12$	Orthorhombic $P2_12_12$	Orthorhombic $P2_12_12$
Crystal dimension **A, b, c (Å)** **α, β,γ (°)**	 51.7 × 81.7 × 100.3 90.0, 90.0, 90.0	 51.7 × 82.0 × 100.2 90.0, 90.0, 90.0	 49.8 × 49,8 × 116.9 90.0, 90.0, 120.0
Maximum resolution (Å)	2.2	2.0	1.8
# of images collected	360	180	280
Notes on reflection images	Reflections appear clean; diffracted beyond 2.2 Å; mosaicity was low ~ 0.358	High mosaicity ~ 2.863	Data good to about 2.5 Å; average mosaicity ~ 0.3

Crystals collected at the Canadian Light Source, Canadian Macromolecular Crystallography Facility, University of Saskatchewan

Protein	**SeMet WT N-TnC – Ca^{2+}**	**SeMet WT N-TnC – Ca^{2+}**	**SeMet WT N-TnC– Ca^{2+}**	**SeMet WT N-TnC– Ca^{2+}**
Dataset name	ALI_A	ALI_B	ALI_C	ALI_D
Data collected	Aug 8, 2008	Aug 8, 2008	Aug 8, 2008	Aug 8, 2008
Crystal-to-detector distance (mm)	180	180	190	210
Beamline	081D-1	081D-1	081D-1	081D-1
Beam center (X, Y)	111.22, 110.78	111.22, 110.78	111.28, 110.78	111.22, 110.78
Exposure time	--	--	--	--
Crystallization condition	0.05M $CdSO_4$, 0.6 M NaOAc, and 0.1 M Hepes pH 7.5	0.05M $CdSO_4$, 0.7 M NaOAc, and 0.1M Hepes pH 7.5	0.05M $CdSO_4$, 0.8 M NaOAc, and 0.1M Tris pH 8.0	0.05M $CdSO_4$, 0.8 M NaOAc, and 0.1M Tris pH 8.0
Cryoprotectant solution	Mother liquor + 30% glycerol	Mother liquor + 30% glycerol	Mother liquor + 30% glycerol	Mother liquor + 30% glycerol
Unit cell **space group**	Orthorhombic $P2_12_12$	Orthorhombic $P2_12_12$	Orthorhombic $P2_12_12$	Orthorhombic $P2_12_12$
Crystal dimension **A, b, c (Å)** **α, β,γ (°)**	 51.9 × 81.9 × 100.5 90.0, 90.0, 90.0	 51.7 × 82.0 × 100.2 90.0, 90.0, 90.0	 51.8 × 82.1 × 100.7 90.0, 90.0, 90.0	 51.9 × 81.9 × 100.6 90.0, 90.0, 90.0
Maximum resolution (Å)	2.07	2.00	3.00	2.77
# of images collected	150	180	130	260
Notes on reflection images	Spots are clear and well-separated	Spots are clear and well-separated	Spots are clear and well-separated	

5: BIBLIOGRAPHY

Abusamhadneh, E.,Abbott, M. B.,Dvoretsky, A.,Finley, N.,Sasi, S. and Rosevear, P. R. (2001). "Interaction of bepridil with the cardiac troponin C/troponin I complex." FEBS Lett **506**(1): 51-4.

Adams, P. D.,Grosse-Kunstleve, R. W.,Hung, L. W.,Ioerger, T. R.,McCoy, A. J.,Moriarty, N. W.,Read, R. J.,Sacchettini, J. C.,Sauter, N. K. and Terwilliger, T. C. (2002). "PHENIX: building new software for automated crystallographic structure determination." Acta Crystallogr D Biol Crystallogr **58**(Pt 11): 1948-54.

Addlagatta, A.,Krzywda, S.,Czapinska, H.,Otlewski, J. and Jaskolski, M. (2001). "Ultrahigh-resolution structure of a BPTI mutant." Acta Crystallogr D Biol Crystallogr **57**(Pt 5): 649-63.

Afonine, P. V., Grosse-Kunstleve, R.W. & Adams, P.D. (2005). The Phenix refinement framework. CCP4 Newsletter on Protein Crystallography. **42: Contribution 8**

Banumathi, S.,Zwart, P. H.,Ramagopal, U. A.,Dauter, M. and Dauter, Z. (2004). "Structural effects of radiation damage and its potential for phasing." Acta Crystallogr D Biol Crystallogr **60**(Pt 6): 1085-93.

Baryshnikova, O. K.,Li, M. X. and Sykes, B. D. (2008). "Modulation of cardiac troponin C function by the cardiac-specific N-terminus of troponin I: influence of PKA phosphorylation and involvement in cardiomyopathies." J Mol Biol **375**(3): 735-51.

Bennett-Lovsey, R. M.,Herbert, A. D.,Sternberg, M. J. and Kelley, L. A. (2008). "Exploring the extremes of sequence/structure space with ensemble fold recognition in the program Phyre." Proteins **70**(3): 611-25.

Borek, D.,Ginell, S. L.,Cymborowski, M.,Minor, W. and Otwinowski, Z. (2007). "The many faces of radiation-induced changes." J Synchrotron Radiat **14**(Pt 1): 24-33.

Bouckaert, J.,Loris, R. and Wyns, L. (2000). "Zinc/calcium- and cadmium/cadmium-substituted concanavalin A: interplay of metal binding, pH and molecular packing." Acta Crystallogr D Biol Crystallogr **56**(Pt 12): 1569-76.

Brefort, J. (2001). GChemPaint 0.8.7.

Burmeister, W. P. (2000). "Structural changes in a cryo-cooled protein crystal owing to radiation damage." Acta Crystallogr D Biol Crystallogr **56**(Pt 3): 328-41.

Chandra, N.,Acharya, K. R. and Moody, P. C. (1999). "Analysis and characterization of data from twinned crystals." Acta Crystallogr D Biol Crystallogr **55**(Pt 10): 1750-8.

Chang, A. N.,Harada, K.,Ackerman, M. J. and Potter, J. D. (2005). "Functional consequences of hypertrophic and dilated cardiomyopathy-causing mutations in alpha-tropomyosin." J Biol Chem **280**(40): 34343-9.

Chen, X.,Mellon, R. D.,Yang, L.,Dong, H.,Oppenheim, J. J. and Howard, O. M. (2002). "Regulatory effects of deoxycholic acid, a component of the anti-inflammatory traditional Chinese medicine Niuhuang, on human leukocyte response to chemoattractants." Biochem Pharmacol **63**(3): 533-41.

Claude, J. B.,Suhre, K.,Notredame, C.,Claverie, J. M. and Abergel, C. (2004). "CaspR: a web server for automated molecular replacement using homology modelling." Nucleic Acids Res **32**(Web Server issue): W606-9.

Cowtan, K. (1994). "'dm': An Automated Procedure for Phase Improvement by Density Modification." Joint CCP4 and ESF-EACBM Newsletter on Protein Crystallography **31**: 34-38.

Cramb, G. and Dow, J. W. (1983). "Two site binding of bepridil and modulation of adenylate cyclase in cardiac sarcolemmal membranes." Biochim Biophys Acta **736**(1): 99-108.

DeLana, W. L. (2002). "The PyMol molecular graphics system." DeLano Scientific.

DeLano, W. L. (2002). "The PyMol molecular graphics system." DeLano Scientific.

Dokmanic, I.,Sikic, M. and Tomic, S. (2008). "Metals in proteins: correlation between the metal-ion type, coordination number and the amino-acid residues involved in the coordination." Acta Crystallogr D Biol Crystallogr **64**(Pt 3): 257-63.

Dvoretsky, A.,Abusamhadneh, E. M.,Howarth, J. W. and Rosevear, P. R. (2002). "Solution structure of calcium-saturated cardiac troponin C bound to cardiac troponin I." J Biol Chem **277**(41): 38565-70.

Dweck, D.,Hus, N. and Potter, J. D. (2008). "Challenging current paradigms related to cardiomyopathies. Are changes in the Ca2+ sensitivity of myofilaments containing cardiac troponin C mutations (G159D and L29Q) good predictors of the phenotypic outcomes?" J Biol Chem **283**(48): 33119-28.

Ebashi, S.,Endo, M. and Otsuki, I. (1969). "Control of muscle contraction." Q Rev Biophys **2**(4): 351-84.

Ebashi, S. and Kodama, A. (1966). "Native tropomyosin-like action of troponin on trypsin-treated myosin B." J Biochem **60**(6): 733-4.

Emsley, P., and Cowtan, K. (2004). "Coot: model-building tools for molecular graphics." Acta Crystallogr D Biol Crystallogr **60**(Pt 12 Pt 1): 2126-32.

Farah, C. S. and Reinach, F. C. (1995). "The troponin complex and regulation of muscle contraction." Faseb J **9**(9): 755-67.

Fatkin, D. and Graham, R. M. (2002). "Molecular mechanisms of inherited cardiomyopathies." Physiol Rev **82**(4): 945-80.

Finley, N.,Abbott, M. B.,Abusamhadneh, E.,Gaponenko, V.,Dong, W.,Gasmi-Seabrook, G.,Howarth, J. W.,Rance, M.,Solaro, R. J.,Cheung, H. C. and Rosevear, P. R. (1999). "NMR analysis of cardiac troponin C-troponin I complexes: effects of phosphorylation." FEBS Lett **453**(1-2): 107-12.

Flicker, P. F.,Phillips, G. N., Jr. and Cohen, C. (1982). "Troponin and its interactions with tropomyosin. An electron microscope study." J Mol Biol **162**(2): 495-501.

French, A. S. and Jarvilehto, M. (1978). "The dynamic behaviour of photoreceptor cells in the fly in response to random (white noise) stimulation at a range of temperatures." J Physiol **274**: 311-22.
Fujimori, K.,Sorenson, M.,Herzberg, O.,Moult, J. and Reinach, F. C. (1990). "Probing the calcium-induced conformational transition of troponin C with site-directed mutants." Nature **345**(6271): 182-4.
Geeves, M. A.,Chai, M. and Lehrer, S. S. (2000). "Inhibition of actin-myosin subfragment 1 ATPase activity by troponin I and IC: relationship to the thin filament states of muscle." Biochemistry **39**(31): 9345-50.
Gill, A.,Flaim, S. F.,Damiano, B. P.,Sit, S. P. and Brannan, M. D. (1992). "Pharmacology of bepridil." Am J Cardiol **69**(11): 11D-16D.
Gillis, T. E.,Liang, B.,Chung, F. and Tibbits, G. F. (2005). "Increasing mammalian cardiomyocyte contractility with residues identified in trout troponin C." Physiol Genomics **22**(1): 1-7.
Gomes, A. V. and Potter, J. D. (2004). "Molecular and cellular aspects of troponin cardiomyopathies." Ann N Y Acad Sci **1015**: 214-24.
Gonzalez, A. (2007). "A comparison of SAD and two-wavelength MAD phasing for radiation-damaged Se-MET crystals." J Synchrotron Radiat **14**(Pt 1): 43-50.
Gordon, A. M.,Homsher, E. and Regnier, M. (2000). "Regulation of contraction in striated muscle." Physiol Rev **80**(2): 853-924.
Gordon, A. M.,Regnier, M. and Homsher, E. (2001). "Skeletal and cardiac muscle contractile activation: tropomyosin "rocks and rolls"." News Physiol Sci **16**: 49-55.
Gouet, P.,Courcelle, E.,Stuart, D. I. and Metoz, F. (1999). "ESPript: analysis of multiple sequence alignments in PostScript." Bioinformatics **15**(4): 305-8.
Grabarek, Z.,Tan, R. Y.,Wang, J.,Tao, T. and Gergely, J. (1990). "Inhibition of mutant troponin C activity by an intra-domain disulphide bond." Nature **345**(6271): 132-5.
Gulati, J.,Babu, A. and Su, H. (1992). "Functional delineation of the Ca(2+)-deficient EF-hand in cardiac muscle, with genetically engineered cardiac-skeletal chimeric troponin C." J Biol Chem **267**(35): 25073-7.
Harding, M. M. (2002). "Metal-ligand geometry relevant to proteins and in proteins: sodium and potassium." Acta Crystallogr D Biol Crystallogr **58**(Pt 5): 872-4.
Herzberg, O. and James, M. N. (1985). "Structure of the calcium regulatory muscle protein troponin-C at 2.8 A resolution." Nature **313**(6004): 653-9.
Herzberg, O.,Moult, J. and James, M. N. (1986). "A model for the Ca2+-induced conformational transition of troponin C. A trigger for muscle contraction." J Biol Chem **261**(6): 2638-44.
Hoffmann, B.,Schmidt-Traub, H.,Perrot, A.,Osterziel, K. J. and Gessner, R. (2001). "First mutation in cardiac troponin C, L29Q, in a patient with hypertrophic cardiomyopathy." Hum Mutat **17**(6): 524.
Holton, J. M. (2009). "A beginner's guide to radiation damage." J Synchrotron Radiat **16**(Pt 2): 133-42.

Houdusse, A.,Love, M. L.,Dominguez, R.,Grabarek, Z. and Cohen, C. (1997). "Structures of four Ca2+-bound troponin C at 2.0 A resolution: further insights into the Ca2+-switch in the calmodulin superfamily." Structure **5**(12): 1695-711.

Howells, M. R., Beetz, T., Chapman, H.N., Cui, C., Holton, J. M., Jacobsen, C. J., Lima, J. Kirz E., Marchesini, S., Miao H., Sayre, D. , Shapiro, D. A., Spence, J. C. H. (2005). "An assessment of the resolution limitation due to radiation-damage in x-ray

diffraction microscopy." Journ. of El. Spect. & Rel. Phen. **In the press**: 4-12.

Karibe, A.,Tobacman, L. S.,Strand, J.,Butters, C.,Back, N.,Bachinski, L. L.,Arai, A. E.,Ortiz, A.,Roberts, R.,Homsher, E. and Fananapazir, L. (2001). "Hypertrophic cardiomyopathy caused by a novel alpha-tropomyosin mutation (V95A) is associated with mild cardiac phenotype, abnormal calcium binding to troponin, abnormal myosin cycling, and poor prognosis." Circulation **103**(1): 65-71.

Keegan, R. M. and Winn, M. D. (2007). "Automated search-model discovery and preparation for structure solution by molecular replacement." Acta Crystallogr D Biol Crystallogr **63**(Pt 4): 447-57.

Kentish, J. C.,McCloskey, D. T.,Layland, J.,Palmer, S.,Leiden, J. M.,Martin, A. F. and Solaro, R. J. (2001). "Phosphorylation of troponin I by protein kinase A accelerates relaxation and crossbridge cycle kinetics in mouse ventricular muscle." Circ Res **88**(10): 1059-65.

King, W. A.,Stone, D. B.,Timmins, P. A.,Narayanan, T.,von Brasch, A. A.,Mendelson, R. A. and Curmi, P. M. (2005). "Solution structure of the chicken skeletal muscle troponin complex via small-angle neutron and X-ray scattering." J Mol Biol **345**(4): 797-815.

Kleerekoper, Q.,Liu, W.,Choi, D. and Putkey, J. A. (1998). "Identification of binding sites for bepridil and trifluoperazine on cardiac troponin C." J Biol Chem **273**(14): 8153-60.

Ko, T. P.,Day, J.,Malkin, A. J. and McPherson, A. (1999). "Structure of orthorhombic crystals of beef liver catalase." Acta Crystallogr D Biol Crystallogr **55**(Pt 8): 1383-94.

Kretsinger, R. H. and Nockolds, C. E. (1973). "Carp muscle calcium-binding protein. II. Structure determination and general description." J Biol Chem **248**(9): 3313-26.

Krudy, G. A.,Brito, R. M.,Putkey, J. A. and Rosevear, P. R. (1992). "Conformational changes in the metal-binding sites of cardiac troponin C induced by calcium binding." Biochemistry **31**(6): 1595-602.

Levijoki, J.,Pollesello, P.,Kaivola, J.,Tilgmann, C.,Sorsa, T.,Annila, A.,Kilpelainen, I. and Haikala, H. (2000). "Further evidence for the cardiac troponin C mediated calcium sensitization by levosimendan: structure-response and binding analysis with analogs of levosimendan." J Mol Cell Cardiol **32**(3): 479-91.

Li, M. X.,Robertson, I. M. and Sykes, B. D. (2008). "Interaction of cardiac troponin with cardiotonic drugs: a structural perspective." Biochem Biophys Res Commun **369**(1): 88-99.

Li, M. X.,Spyracopoulos, L. and Sykes, B. D. (1999). "Binding of cardiac troponin-I147-163 induces a structural opening in human cardiac troponin-C." Biochemistry **38**(26): 8289-98.

Li, Y.,Love, M. L.,Putkey, J. A. and Cohen, C. (2000). "Bepridil opens the regulatory N-terminal lobe of cardiac troponin C." Proc Natl Acad Sci U S A **97**(10): 5140-5.

Liang, B.,Chung, F.,Qu, Y.,Pavlov, D.,Gillis, T. E.,Tikunova, S. B.,Davis, J. P. and Tibbits, G. F. (2008). "Familial hypertrophic cardiomyopathy-related cardiac troponin C mutation L29Q affects Ca2+ binding and myofilament contractility." Physiol Genomics **33**(2): 257-66.

Lues, I.,Beier, N.,Jonas, R.,Klockow, M. and Haeusler, G. (1993). "The two mechanisms of action of racemic cardiotonic EMD 53998, calcium sensitization and phosphodiesterase inhibition, reside in different enantiomers." J Cardiovasc Pharmacol **21**(6): 883-92.

Marsden, B. J.,Shaw, G. S. and Sykes, B. D. (1990). "Calcium binding proteins. Elucidating the contributions to calcium affinity from an analysis of species variants and peptide fragments." Biochem Cell Biol **68**(3): 587-601.

McCoy, A. J.,Grosse-Kunstleve, R. W.,Adams, P. D.,Winn, M. D.,Storoni, L. C. and Read, R. J. (2007). "Phaser crystallographic software." J Appl Crystallogr **40**(Pt 4): 658-674.

Minichino, A.,Habash, J.,Raftery, J. and Helliwell, J. R. (2003). "The properties of (2Fo - Fc) and (Fo - Fc) electron-density maps at medium-to-high resolutions." Acta Crystallogr D Biol Crystallogr **59**(Pt 5): 843-9.

Minor, W.,Cymborowski, M.,Otwinowski, Z. and Chruszcz, M. (2006). "HKL-3000: the integration of data reduction and structure solution--from diffraction images to an initial model in minutes." Acta Crystallogr D Biol Crystallogr **62**(Pt 8): 859-66.

Neugebauer, J. M. (1990). "Detergents: An overview." Methods in Enzymology **184**: 239-253.

Otsuki, I.,Masaki, T.,Nonomura, Y. and Ebashi, S. (1967). "Periodic distribution of troponin along the thin filament." J Biochem **61**(6): 817-9.

Otwinowski, Z. (1991). "Maximum likelihood refinement of heavy atom parameters." CCP4 Study Weekend Proceedings **Isomorphous Replacement And Anomalous Scattering**: 80-87.

Otwinowski, Z. and Minor, W. (1997). Processing of X-ray Diffraction Data Collected in Oscillation Mode. Methods Enzymol. J. C.W. Carter and R. M. Sweet, Academic Press. **276:** 307-326.

Otwinowski, Z. and Minor, W. (1997). "Processing of X-ray Diffraction Data Collected in Oscillation Mode." Methods in Enzymology **276: Macromolecular Crystallography, part A**: 307-326.

Otwinowski, Z. and Minor, W. (2000). Denzo and Scalepack. International Tables for Crystallography. M. G. Rossman. Dordrecht, Kluwer Academic Publishers. **F:** 226:235.

Painter, J., and Merritt, E. A. (2006). "Optimal description of a protein structure in terms of multiple groups undergoing TLS motion." Acta Crystallogr D Biol Crystallogr **62**(Pt 4): 439-50.

Pan, B. S. and Johnson, R. G., Jr. (1996). "Interaction of cardiotonic thiadiazinone derivatives with cardiac troponin C." J Biol Chem **271**(2): 817-23.

Perrakis, A.,Sixma, T. K.,Wilson, K. S. and Lamzin, V. S. (1997). "wARP: Improvement and extension of crystallographic phases by weighted averaging of multiple-refined dummy atomic models." Acta Crystallographica Section D-Biological Crystallography **53**: 448-455.

Pinto, J. R.,Parvatiyar, M. S.,Jones, M. A.,Liang, J.,Ackerman, M. J. and Potter, J. D. (2009). "A functional and structural study of troponin C mutations related to hypertrophic cardiomyopathy." J Biol Chem.

Potter, J. D. and Gergely, J. (1975). "The calcium and magnesium binding sites on troponin and their role in the regulation of myofibrillar adenosine triphosphatase." J Biol Chem **250**(12): 4628-33.

Putkey, J. A.,Dotson, D. G. and Mouawad, P. (1993). "Formation of inter- and intramolecular disulfide bonds can activate cardiac troponin C." J Biol Chem **268**(10): 6827-30.

Ramagopal, U. A.,Dauter, Z.,Thirumuruhan, R.,Fedorov, E. and Almo, S. C. (2005). "Radiation-induced site-specific damage of mercury derivatives: phasing and implications." Acta Crystallogr D Biol Crystallogr **61**(Pt 9): 1289-98.

Rao, S. T.,Satyshur, K. A.,Greaser, M. L. and Sundaralingam, M. (1996). "X-ray structures of Mn, Cd and Tb metal complexes of troponin C." Acta Crystallogr D Biol Crystallogr **52**(Pt 5): 916-22.

Ravelli, R. B. and McSweeney, S. M. (2000). "The 'fingerprint' that X-rays can leave on structures." Structure **8**(3): 315-28.

Rees, D. C. and Lipscomb, W. N. (1980). "Structure of potato inhibitor complex of carboxypeptidase A at 5.5-A resolution." Proc Natl Acad Sci U S A **77**(1): 277-80.

Robertson, I. M.,Baryshnikova, O. K.,Li, M. X. and Sykes, B. D. (2008). "Defining the binding site of levosimendan and its analogues in a regulatory cardiac troponin C-troponin I complex." Biochemistry **47**(28): 7485-95.

Robertson, S. P.,Johnson, J. D.,Holroyde, M. J.,Kranias, E. G.,Potter, J. D. and Solaro, R. J. (1982). "The effect of troponin I phosphorylation on the Ca2+-binding properties of the Ca2+-regulatory site of bovine cardiac troponin." J Biol Chem **257**(1): 260-3.

Rossmann, M. G. (1990). "The molecular replacement method." Acta Crystallogr A **46 (Pt 2)**: 73-82.

Sambrook, J., Fritsch, E.F., and Maniatis, T. (1989). Molecular Cloning: A Laboratory Manual, Cold Spring Harbor, NY, Cold Spring Habor Laboratory Press.

Satyshur, K. A.,Rao, S. T.,Pyzalska, D.,Drendel, W.,Greaser, M. and Sundaralingam, M. (1988). "Refined structure of chicken skeletal muscle troponin C in the two-calcium state at 2-A resolution." J Biol Chem **263**(4): 1628-47.

Schmidtmann, A.,Lindow, C.,Villard, S.,Heuser, A.,Mugge, A.,Gessner, R.,Granier, C. and Jaquet, K. (2005). "Cardiac troponin C-L29Q, related to

hypertrophic cardiomyopathy, hinders the transduction of the protein kinase A dependent phosphorylation signal from cardiac troponin I to C." Febs J **272**(23): 6087-97.

Sheldrick, G. M. (2008). "A short history of SHELX." Acta Crystallogr A **64**(Pt 1): 112-22.

Sia, S. K.,Li, M. X.,Spyracopoulos, L.,Gagne, S. M.,Liu, W.,Putkey, J. A. and Sykes, B. D. (1997). "Structure of cardiac muscle troponin C unexpectedly reveals a closed regulatory domain." J Biol Chem **272**(29): 18216-21.

Silver, P. J.,Pinto, P. B. and Dachiw, J. (1986). "Modulation of vascular and cardiac contractile protein regulatory mechanisms by calmodulin inhibitors and related compounds." Biochem Pharmacol **35**(15): 2545-51.

Solaro, R. J.,Bousquet, P. and Johnson, J. D. (1986). "Stimulation of cardiac myofilament force, ATPase activity and troponin C Ca++ binding by bepridil." J Pharmacol Exp Ther **238**(2): 502-7.

Solaro, R. J.,Gambassi, G.,Warshaw, D. M.,Keller, M. R.,Spurgeon, H. A.,Beier, N. and Lakatta, E. G. (1993). "Stereoselective actions of thiadiazinones on canine cardiac myocytes and myofilaments." Circ Res **73**(6): 981-90.

Sorsa, T.,Heikkinen, S.,Abbott, M. B.,Abusamhadneh, E.,Laakso, T.,Tilgmann, C.,Serimaa, R.,Annila, A.,Rosevear, P. R.,Drakenberg, T.,Pollesello, P. and Kilpelainen, I. (2001). "Binding of levosimendan, a calcium sensitizer, to cardiac troponin C." J Biol Chem **276**(12): 9337-43.

Sorsa, T.,Pollesello, P.,Permi, P.,Drakenberg, T. and Kilpelainen, I. (2003). "Interaction of levosimendan with cardiac troponin C in the presence of cardiac troponin I peptides." J Mol Cell Cardiol **35**(9): 1055-61.

Spyracopoulos, L.,Li, M. X.,Sia, S. K.,Gagne, S. M.,Chandra, M.,Solaro, R. J. and Sykes, B. D. (1997). "Calcium-induced structural transition in the regulatory domain of human cardiac troponin C." Biochemistry **36**(40): 12138-46.

Stefancsik, R.,Jha, P. K. and Sarkar, S. (1998). "Identification and mutagenesis of a highly conserved domain in troponin T responsible for troponin I binding: potential role for coiled coil interaction." Proc Natl Acad Sci U S A **95**(3): 957-62.

Stein, N. (2008). "CHAINSAW: a program for mutating pdb files used as templates in molecular replacement." J. Appl. Cryst. **41**: 641-643.

Strynadka, N. C.,Cherney, M.,Sielecki, A. R.,Li, M. X.,Smillie, L. B. and James, M. N. (1997). "Structural details of a calcium-induced molecular switch: X-ray crystallographic analysis of the calcium-saturated N-terminal domain of troponin C at 1.75 A resolution." J Mol Biol **273**(1): 238-55.

Strynadka, N. C. and James, M. N. (1989). "Crystal structures of the helix-loop-helix calcium-binding proteins." Annu Rev Biochem **58**: 951-98.

Strynadka, N. C. J.,Cherney, M.,Sielecki, A. R.,Li, M. X.,Smillie, L. B. and James, M. N. G. (1997). "Structural details of a calcium-induced molecular switch: X-ray crystallographic analysis of the calcium-saturated N-terminal domain of troponin C at 1.75 Å resolution." Journal of Molecular Biology **273**(1): 238-255.

Sundaralingam, M.,Bergstrom, R.,Strasburg, G.,Rao, S. T.,Roychowdhury, P.,Greaser, M. and Wang, B. C. (1985). "Molecular structure of troponin C from chicken skeletal muscle at 3-angstrom resolution." Science **227**(4689): 945-8.

Sweeney, H. L.,Brito, R. M.,Rosevear, P. R. and Putkey, J. A. (1990). "The low-affinity Ca2(+)-binding sites in cardiac/slow skeletal muscle troponin C perform distinct functions: site I alone cannot trigger contraction." Proc Natl Acad Sci U S A **87**(24): 9538-42.

Takeda, S., Igarashi, T., Oishi, Y., and Mori, H. (2006). "Crystal structure of the N-terminal domain of human cardiac troponin C in complex with trifluoperazine." To be Published

Takeda, S., Igarashi, T., Oishi, Y., Mori, H. (2004). "Crystal structure of the N-terminal domain of human cardiac troponin C in complex with trifluoperazine " To be Published

Takeda, S.,Yamashita, A.,Maeda, K. and Maeda, Y. (2003). "Structure of the core domain of human cardiac troponin in the Ca(2+)-saturated form." Nature **424**(6944): 35-41.

Tanaka, T.,Umekawa, H.,Ohmura, T. and Hidaka, H. (1984). "Calcium-dependent hydrophobic chromatography of calmodulin, S-100 protein and troponin-C." Biochim Biophys Acta **787**(2): 158-64.

Terwilliger, T. C. and Berendzen, J. (1999). "Automated MAD and MIR structure solution." Acta Crystallogr D Biol Crystallogr **55**(Pt 4): 849-61.

Thompson, J. D.,Gibson, T. J. and Higgins, D. G. (2002). "Multiple sequence alignment using ClustalW and ClustalX." Curr Protoc Bioinformatics **Chapter 2**: Unit 2 3.

Tikhonov, A. N., and Arsenin, V. Y (1977). Solutions of ill-posed problems. New York, distributed by Wiley and Sons.

Tsuda, S.,Miura, A.,Gagne, S. M.,Spyracopoulos, L. and Sykes, B. D. (1999). "Low-temperature-induced structural changes in the Apo regulatory domain of skeletal muscle troponin C." Biochemistry **38**(18): 5693-700.

Vagin, A. a. T., A (1997). " MOLREP: an automated program for molecular replacement." Journal of Applied Crystallography **30**: 1022-1025.

van Eerd, J. P., and Takahashi, K. (1975). "The amino acid sequence of bovine cardiac tamponin-C. Comparison with rabbit skeletal troponin-C." Biochem Biophys Res Commun **64**(1): 122-7.

Vassylyev, D. G.,Takeda, S.,Wakatsuki, S.,Maeda, K. and Maeda, Y. (1998). "Crystal structure of troponin C in complex with troponin I fragment at 2.3-A resolution." Proc Natl Acad Sci U S A **95**(9): 4847-52.

Vinogradova, M. V.,Stone, D. B.,Malanina, G. G.,Karatzaferi, C.,Cooke, R.,Mendelson, R. A. and Fletterick, R. J. (2005). "Ca(2+)-regulated structural changes in troponin." Proc Natl Acad Sci U S A **102**(14): 5038-43.

Wang, X.,Li, M. X.,Spyracopoulos, L.,Beier, N.,Chandra, M.,Solaro, R. J. and Sykes, B. D. (2001). "Structure of the C-domain of human cardiac troponin C in complex with the Ca2+ sensitizing drug EMD 57033." J Biol Chem **276**(27): 25456-66.

Wang, X.,Li, M. X. and Sykes, B. D. (2002). "Structure of the regulatory N-domain of human cardiac troponin C in complex with human cardiac troponin I147-163 and bepridil." J Biol Chem **277**(34): 31124-33.

Ward, D. G.,Brewer, S. M.,Gallon, C. E.,Gao, Y.,Levine, B. A. and Trayer, I. P. (2004). "NMR and mutagenesis studies on the phosphorylation region of human cardiac troponin I." Biochemistry **43**(19): 5772-81.

Watson, J. (1972). The Mechanism of Muscle Contraction. Cold Spring Harbor Symposia on Quantitative Biology, Long Island
Cold Spring Harbor Laboratory Press.

Weik, M.,Ravelli, R. B.,Kryger, G.,McSweeney, S.,Raves, M. L.,Harel, M.,Gros, P.,Silman, I.,Kroon, J. and Sussman, J. L. (2000). "Specific chemical and structural damage to proteins produced by synchrotron radiation." Proc Natl Acad Sci U S A **97**(2): 623-8.

White, S. P.,Cohen, C. and Phillips, G. N., Jr. (1987). "Structure of co-crystals of tropomyosin and troponin." Nature **325**(6107): 826-8.

Winn, M. D.,Isupov, M. N. and Murshudov, G. N. (2001). "Use of TLS parameters to model anisotropic displacements in macromolecular refinement." Acta Crystallogr D Biol Crystallogr **57**(Pt 1): 122-33.

Winter, M. (2009). WebElements: the periodic table on the WWW. UK**:** http://www.webelements.com/.

Xu, G. Q. and Hitchcock-DeGregori, S. E. (1988). "Synthesis of a troponin C cDNA and expression of wild-type and mutant proteins in Escherichia coli." J Biol Chem **263**(27): 13962-9.

Yeates, T. O. (1997). "Detecting and overcoming crystal twinning." Methods Enzymol **276**: 344-58.

Yeates, T. O. and Fam, B. C. (1999). "Protein crystals and their evil twins." Structure **7**(2): R25-9.

Zot, H. G. and Potter, J. D. (1982). "A structural role for the Ca2+-Mg2+ sites on troponin C in the regulation of muscle contraction. Preparation and properties of troponin C depleted myofibrils." J Biol Chem **257**(13): 7678-83.